Trinity College Dublin
Coláiste na Tríonóide, Baile Átha Cliath
The University of Dublin

School of Mathematics

Heavy Hadron Spectroscopy from Lattice QCD

Luke Gayer

Supervisor: Prof. Sinéad Ryan

January 24, 2024

A thesis submitted in partial fulfilment
of the requirements for the degree of
Doctor of Philosophy

Declaration

I declare that this thesis has not been submitted as an exercise for a degree at this or any other university and it is entirely my own work.

I agree to deposit this thesis in the University's open access institutional repository or allow the Library to do so on my behalf, subject to Irish Copyright Legislation and Trinity College Library conditions of use and acknowledgement.

I consent to the examiner retaining a copy of the thesis beyond the examining period, should they so wish (EU GDPR May 2018).

Parts of this thesis are based on published work. Chapter 4 is based on publication [1], which was produced in collaboration with Nicolas Lang Sinéad Ryan, David Tims, Christopher Thomas and David Wilson. Chapter 5 is based on work to be published, in collaboration with Sinéad Ryan and David Wilson.

Signed: _Luke Mayer_____ Date: _20/01/2024_____

Summary

In this thesis, heavy hadron spectroscopy was studied through the formalism of lattice quantum chromodynamics. A summary of relevant theory is provided, followed by an overview of the current state-of-the-art spectroscopy methods that were employed in this work. Finite volume spectra were computed using the variational method with distillation. The finite-volume spectra computed were used to constrain infinite-volume scattering amplitudes using Lüscher's method. The scattering amplitude of the isospin-1/2 $D\pi$ S-wave was computed. By analytically continuing this amplitude to complex energies, a resonance pole was found. This pole was identified as the D_0^* meson. Extrapolating to physical pion mass suggests that the current reported experimental mass of the D_0^* is too high.

Also covered in this thesis is a calculation of the excited and exotic spectra of the B, B_s and B_c mesons. An extensive spectrum was determined in each meson sector, with robust spin identification. The presence of hybrid mesons was investigated, with candidate states for a hybrid supermultiplet proposed in each meson sector. The mixing of states occurring due to symmetry breaking on the lattice was also studied. The B and B_s mesons were found to be strongly mixed, while the mixing in B_c was much weaker. The analysis of the B meson was extended further, with an exploratory study of isospin-3/2 $B\pi$ scattering performed. The scattering amplitude for the S-wave was computed, and was found to be the form of a weakly repulsive interaction. This thesis concludes with an overview of its findings.

Acknowledgements

Thanks to all of my friends, who have kept me sane over these four years, with chats, card games and fifa nights, in particular John and Conor, who have been constants throughout my eight years studying in Trinity. Thank you Mom, Dad, and Ben, for providing constant support from home throughout my studies. Finally, a special thank you to my fiancée Lisa, I couldn't have done this without you.

Contents

List of Figures

List of Tables

1   Introduction

Quantum chromodynamics (QCD) is the theory of the strong interaction between quarks and gluons. It is a key component of the Standard Model of particle physics, which is an incredibly successful theory at predicting the behaviour of fundamental particles and forces. QCD is comprised of SU(3) Yang-Mills theory, coupled to Dirac fermions which represent the quarks and antiquarks of the theory. Gluons are represented by the gauge fields in the theory. The gauge charge of the quarks and gluons is referred to as colors, specifically red, blue, and green. Quarks come in six flavours, namely up, down, strange, charm, top and bottom. Although it has yet to be proven, it is strongly believed that QCD is a confining theory, and experimental evidence to date supports this belief, as do lattice results. This means that no quark is observed on its own, all allowed states are color-neutral. Thus quarks and gluons group themselves into color-neutral states. These color neutral states are known as hadrons. More details on the properties and symmetries of QCD are discussed in the next chapter.

Until a few decades ago, only two types of hadrons had been observed experimentally, mesons and baryons. Mesons consist of a quark-antiquark pair while baryons are combinations of three quarks. This experimental observation, combined with the difficulty of analytically computing energy states from QCD, lead to the formulation of the quark model in the 1960s [5,6]. This has proved a successful theory that explained the properties and interactions of hadrons, as well as predicting the presence of hadrons that were later found experimentally, such as the Ω baryon, which consists of three strange quarks. However, in recent times, states that do not agree with the quark model have been observed. There have been states with masses that are at odds with the quark model prediction, as well as states with quantum numbers that are not allowed by the quark model. These states are known as exotic states. There are many proposals for the nature of these exotic states, ranging from tetraquarks and pentaquarks (four and five-quark states respectively) to glueballs (quark-less states containing only gluons) and hybrid mesons (mesonic states containing excited gluons). Exotic hadron states are thus states which either have quantum numbers not allowed by the quark model, or

are comprised of combinations of quarks and/or gluons which the quark model doesn't allow.

With puzzling experimental observations being made, an upgrade in the theoretical methods was called for. There has been some success calculating with the quark model [7], as well as through the use of effective field theories such as chiral perturbation theory [8] and heavy quark effective field theory [9]. However, ideally one would be able to predict energy states directly from the QCD Lagrangian. This became possible through Lattice QCD, a formulation that restricts QCD to a discrete lattice of finite space-time volume and numerically evaluates the path integral. Lattice QCD is a non-perturbative theory which provides the means for ab initio predictions of nuclear physics, even at low energies. Lattice QCD allows for the calculation of energy states in a finite volume through the numerical evaluation of correlators. Through a formalism introduced by Lüscher [10], these energies can be related to infinite volume scattering amplitudes, the resonances of which correspond to hadrons.

The work in this thesis was performed through the formalism of lattice QCD. In Chapter 2 the formalism of lattice QCD will be introduced, and some of its properties will be discussed. Chapter 3 will provide the details of how a finite volume energy spectrum is determined through Lattice QCD, and how these energies can be used to gain access to infinite volume scattering amplitudes. A particularly puzzling experimental result dealing with charm-light mesons is discussed in Chapter 4 with a possible resolution being provided through the results of a scattering analysis of isospin-$1/2$ $D\pi$ scattering. Note that this chapter is based on published work [1]. While many puzzling results have been observed experimentally in the charm-sector, few experimental results exist in the bottom-sector. However, with more runs being performed by LHCb [11] and Belle II [12], this may soon change. Many puzzles similar to those found in the charm-sector are predicted to be present in the bottom-sector. Motivated by this Chapter 5 presents the results of the determination of the finite volume energy spectra of the B (bottom-light), B_s (bottom-strange) and B_c (bottom-charm) mesons, which includes hybrid mesons. Note that this chapter is based on work to be published. Finally Chapter 6 discusses the results of an exploratory study into isospin-$3/2$ $B\pi$ scattering.

2   Lattice QCD

The QCD Lagrangian is given by

$$\mathcal{L}_{QCD} = \sum_{f=1}^{6} \sum_{a,b=1}^{3} \sum_{\alpha,\beta,\mu=0}^{3} \bar{\psi}_{\alpha}^{(f)} \left(i\gamma_{\alpha\beta}^{\mu} D_{\mu;ab} - m_f \delta_{\alpha\beta} \delta_{ab} \right) \psi_{\beta}^{(f)} + \sum_{i=1}^{8} \sum_{\mu,\nu=0}^{3} -\frac{1}{4} G_{\mu\nu}^{i} \, G_{i}^{\mu\nu}. \tag{2.1}$$

This is commonly split into two terms, $\mathcal{L}_{QCD} = \mathcal{L}_F + \mathcal{L}_G$. To obtain the action, one integrates over Minkowski space time,

$$\begin{aligned} S_{QCD}(\psi, \bar{\psi}, A) &= \int d^4 x \, \mathcal{L}_{QCD}(\psi(x), \bar{\psi}(x), A(x)) \\ &= \int d^4 x \, \mathcal{L}_F(\psi(x), \bar{\psi}(x), A(x)) + \int d^4 x \, \mathcal{L}_G(\psi(x), \bar{\psi}(x), A(x)) \\ &= S_F + S_G \end{aligned} \tag{2.2}$$

In $\mathcal{L}_F$, $\psi_a^{(f)}$ are the Dirac fermions that correspond to quarks. The sum in $\mathcal{L}_F$ is over the six flavours of quark, labelled f, and the three colors a, b. The indices α, β are the Dirac indices. In QCD, gluons are described by gauge fields A_μ, with μ being a Lorentz index that labels the direction in space-time. The gauge fields $A_\mu \in SU(3)$, the group of special unitary 3×3 matrices with $\det = 1$. Gauge symmetry is a central part of QCD, it accounts for many of the phenomenona observed in particles (more details later in the chapter). To build gauge symmetry into the theory, one must define what the gauge transformation is. Using $\Omega(x) \in SU(3)$, at location x in space-time, one can define the gauge transformation of the fermion fields as

$$\begin{aligned} \psi^{\Omega}(x) &\rightarrow \Omega(x)\psi(x), \\ \bar{\psi}^{\Omega}(x) &\rightarrow \bar{\psi}(x)\Omega^{-1}(x). \end{aligned} \tag{2.3}$$

By demanding that the fermionic action is gauge invariant, $S_F(\psi^{\Omega}, \bar{\psi}^{\Omega}, A^{\Omega}) = S_F(\psi, \bar{\psi}, A)$, one obtains the gauge transformation condition of A_μ,

$$A_\mu^{\Omega}(x) \rightarrow \Omega(x)A_\mu(x)\Omega^{-1}(x) \, + \, i(\delta_\mu \Omega(x))\Omega(x)^{-1}. \tag{2.4}$$

The gauge-covariant derivative, $D_{\mu;ab}$, can then be defined as

$$D_{\mu;ab}(x) = \delta_{ab}\partial_\mu + ig_s \sum_{i=1}^{8} \lambda_{ab}^i A_\mu^i(x), \tag{2.5}$$

with λ_{ab}^i being the Gell-Mann matrices which are the generators of the SU(3) color group and g_s being the strong coupling constant. In $\mathcal{L}_G$, $G_{\mu\nu}^i$ is the gauge invariant gluon field strength tensor, and is given by

$$G_{\mu\nu}^i(x) = \partial_\mu A_\nu^i(x) - \partial_\nu A_\mu^i(x) - g_s f^{ijk} A_\mu^j(x) A_\nu^k(x), \tag{2.6}$$

with f^{ijk} being the structure constants of the SU(3) color group. This is analogous to the electric field tensor, $F^{\mu\nu}$ in quantum electrodynamics. Both the covariant derivative and gluon field strength tensor transform covariantly,

$$\begin{aligned} D_{\mu;ab}^\Omega(x) &= \Omega(x)D_{\mu;ab}(x)\Omega(x)^{-1} \\ G_{\mu\nu}^\Omega(x) &= \Omega(x)G_{\mu\nu}(x)\Omega(x)^{-1} \end{aligned} \tag{2.7}$$

2.1 Discretising QCD

Lattice QCD is a discretised version of Quantum Chromodynamics, where instead of working in the continuum space time, calculations are performed on a finite (3+1)-dimensional space time grid, Λ. This grid is called a lattice and is a set of discrete points with finite spacing between them, with the spacing between points labelled a. The lattice has a finite volume $V = L^3 \times T$, with L being the spatial length and T the temporal length of the lattice. There are $(L/a)^3 \times (T/a) = N^3 \times n_t$ points on the lattice. The lattice is usually periodic, with the boundaries at n_t and n_s being identified with the boundaries at 0. Following the notation of [13], the fermion fields $\psi^{(f)}(n)$ are placed only at lattice sites $n \in \Lambda$. Instead of the gauge fields A_μ, link variables are introduced which are related to lattice gauge fields by $U_\mu(n) = exp(iagA_\mu(n))$. Here, space-time has been discretised, and as such all length scales are quantised with the spacing a. These gauge fields are introduced to ensure the gauge invariance of the discretised fermionic action, specifically the term containing a derivative, with the gauge transformation of $U_\mu(n)$ defined as

$$U_\mu(n)^\Omega \to \Omega(n)U_\mu(n)\Omega^{-1}(n+\hat{\mu}). \tag{2.8}$$

These link variables connect lattice site n to $n + a\hat{\mu}$, a single lattice step in the direction μ, as shown in Figure 2.1. In the continuum, these are known as parallel transporters.
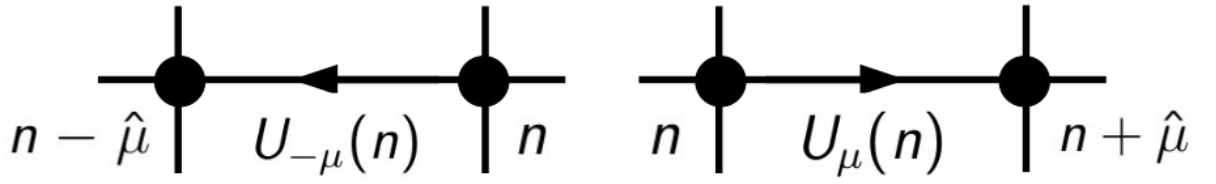
Figure 2.1: The link variables $U_\mu(n)$ and $U_{-\mu}(n)$

They are directed, with $U_{-\mu}(n) \equiv U_\mu(n - \hat{\mu})^\dagger$. Using these link variables, a gauge covariant partial derivative can be defined by

$$\partial_\mu \psi(n) = \frac{U_\mu(n)\psi(n + \hat{\mu}) - U_{-\mu}(n)\psi(n - \hat{\mu})}{2a}, \tag{2.9}$$

where the central difference is used as it has $\mathcal{O}(a^2)$ discretisation effects. Note in this definition, the color indices have been suppressed.

2.2   A note on Symmetries

It is worth noting the symmetries of QCD, especially those that are preserved on the lattice, and having a brief discussion on them, as they motivate some choices made in the discretisation of QCD, as well as playing a big part in how one constructs operators that represent states on the lattice.

2.2.1   Gauge Symmetry

The gauge symmetry of QCD was a necessity to accurately explain the interactions of the strong force, and is built into the theory. It is an SU(3) symmetry, with the charge being the color carried by the quarks and gluons. The allowed colors are labelled as red, green and blue, as well as their anti-colors. The strong interactions are mediated by gauge bosons known as gluons. All hadrons in QCD must be color neutral, a property known as color confinement. On the lattice, this gauge invariance is held by construction, as it is a central piece of the theory. Observables are gauge-invariant as long as the operators involved transform gauge-covariantly. These are very important, as by Elitzur's theorem [14] only gauge-invariant operators have a non-vanishing expectation value in a gauge theory, such as QCD.

2.2.2 Flavour Symmetry

In QCD, there are six flavours of quarks, namely up, down, strange, charm, bottom, top. In this study the top quark is irrelevant due to its much larger mass, as this provides both a computational challenge in terms of the fine lattice spacing required to control systematic errors, as well as the technical challenge of tracking the large energy scale of the top quark in tandem with the much smaller energy scales of the lighter quarks. Flavour symmetry refers to the fact that in the framework of QCD, quarks are treated the same regardless of flavour. However, this symmetry is broken by the unequal quark masses. Up and down quarks have significantly smaller masses than the other flavours of quarks. For this reason, they are typically implemented as two degenerate flavours on the lattice, denoted light quarks. This gives an SU(2) flavour symmetry to the QCD Lagrangian, which is actually a good approximation at physical masses. The strange quark meanwhile, is not as light as the up and down quarks, but is still significantly lighter than the other three flavours. If the strange were to be added to the symmetry with the light quarks, it would create an SU(3) flavour symmetry in the QCD Lagrangian. While this is badly broken at physical quark masses, it is not the worst approximation on the lattice. This is because, quite often on the lattice, calculations are performed with light quarks being at a heavier than physical mass, as simulating at physical light quark mass would require fine lattice spacing, which is computationally expensive. Thus the light quark mass on the lattice is closer to the strange quark which is typically close to its physical mass on the lattice. The assumption of SU(3) flavour symmetry provides a nice way of classifying states into multiplets, which is known as the eightfold way [5].

2.2.3 Rotational Symmetry

In the continuum, QCD has a rotational symmetry, which leads to the conservation of angular momentum. There is also an invariance to inversions in space. As a result of these symmetries, states can be labelled by their angular momentum and parity, J^P. Parity takes a value of $P = \pm 1$ representing odd and even parity states. These label the irreducible representations of the improper rotation group O(3). Projecting the angular momentum onto an axis J_z, gives the rows of the representation. On the lattice however, the continuous rotational symmetry is broken, due to both the finite spacing of the lattice as well as its finite volume. This is replaced by rotations that leave the cube invariant. The corresponding symmetry group is O_h, the cubic point group. States are labelled by their lattice irrep instead of angular momentum, as Λ^P, with the parity label maintained. Again, parity $P = \pm 1$, now corresponding to the spatial inversions

J	Λ
0	A_1
1	T_1
2	$T_2 \oplus E$
3	$T_1 \oplus T_2 \oplus A_2$
4	$A_1 \oplus T_1 \oplus T_2 \oplus E$

Table 2.1: The subduction of continuum spin J into each at-rest lattice irrep

on the octahedral group O. O has five irreducible representations, labelled A_1, A_2, E, T_1 and T_2. The inclusion of parity gives ten lattice irreps. Due to the breaking of the continuous rotational symmetry, states with the same angular momentum and parity J^P can subduce into different lattice irreps, due to differing J_z values. This makes the designing of appropriate operators to represent states very important, as they must project into O_h. Table 2.1 shows how the continuum spin J subduces into each irrep of O_h.

2.3 Lattice Actions

On the lattice, the action is typically computed in Euclidean space-time. To gain access to this, a Wick rotation is performed by $t \rightarrow -it$. The change in metric ensures a positive definite probability density for field configurations. This is not the case in Minkowski space-time, the so-called sign problem arises. This Wick rotation enables the use of the Monte Carlo methods discussed later in this chapter. To compute the action, it is discretised and the integral is replaced by a sum. The fermion action can be written as a bilinear of the form

$$S_F[\psi, \bar{\psi}, U] = \sum_f a^4 \sum_{n,m \in \Lambda} \sum_{a,b,\alpha,\beta} \bar{\psi}^{(f)}(n)_{\underset{a}{\alpha}} D^{(f)}(n|m)_{\underset{ab}{\alpha\beta}} \psi^{(f)}(m)_{\underset{b}{\beta}}, \qquad (2.10)$$

with $D(n|m)$ being the discretised Dirac operator. One must be very careful with the Dirac operator on the lattice, if the only adjustment one makes from the continuum is to treat the derivatives as finite differences, a problem known as fermion doubling will arise. This is the creation of additional solutions to the Dirac equation, typically at higher momentum nodes, due to inherent symmetries on the lattice. To help grasp this issue, consider free fermions in 1-dimension (trivial gauge fields $U_\mu(n) = 1$). Examining the Dirac operator in momentum-space by computing its Fourier transform applied at

sites n and m gives

$$
\begin{aligned}
\tilde{D}(p|q) &= \frac{1}{|\Lambda|} \sum_{n,m \in \Lambda} e^{-ipna} D(n|m) e^{iqma}, \\
&= \frac{1}{|\Lambda|} \sum_{n \in \Lambda} e^{-i(p-q)na} \left(\frac{e^{iqa} - e^{-iqa}}{2a} + m \right), \\
&= \delta(p-q)\tilde{D}(p),
\end{aligned}
\tag{2.11}
$$

where $|\Lambda|$ is the total number of lattice points, and p, q are the momenta associated with the Fourier transform of n, m respectively. The phase signs differ to ensure the unitary similarity transformation. The Fourier transform of the lattice Dirac operator in one-dimension with trivial gauge fields is then given by

$$
\tilde{D}(p) = m + \frac{i}{a} \sin(pa).
\tag{2.12}
$$

The Dirac operator is diagonal in the momenta p, q. Thus to compute the inverse of the Dirac operator in real space, it is sufficient to compute the inverse of $\tilde{D}(p)$, and then invert the Fourier transform. The inverse $\tilde{D}(p)^{-1}$ is given by

$$
\tilde{D}(p)^{-1} = \frac{m - ia^{-1} \sin(pa)}{m^2 + a^{-2} \sin(pa)^2}.
\tag{2.13}
$$

The so-called quark propagator can then be obtained by inverting the Fourier transform,

$$
D^{-1}(n|m) = \frac{1}{|\Lambda|} \sum_{p \in \tilde{\Lambda}} \tilde{D}(p)^{-1} e^{ip(n-m)a}.
\tag{2.14}
$$

The quark propagator represents the probability of a quark travelling from point n to point m. It is important to examine its properties. Considering the massless case, in momentum space the quark propagator still has the correct continuum limit,

$$
\tilde{D}(p)^{-1} = \frac{-ia^{-1} \sin(pa)}{a^{-2} \sin(pa)^2} \xrightarrow{a \to 0} \frac{-ip}{p^2}.
\tag{2.15}
$$

The continuum expression has a pole at $p = 0$, representing the single fermion described by the Dirac operator. However, one will notice that on the lattice, there is an extra pole, given at $p = \pi/a$. This unphysical pole is known as a fermion doubler, and $2^D - 1$ fermion doublers arise on the lattice for a theory of fermions in dimension D. The first Brillouin zone in momentum space contains all allowed distinct momentum values $p \in (-\pi/a, \pi/a]$. It is periodic, identifying $-\pi/a$ with π/a. One can not simply exclude the boundary π/a. To fix the unwanted presence of these doublers, one must do more

with the lattice Dirac operator. A popular solution is to add an extra term to the naive discretisation, known as the Wilson term. This is given by,

$$-\frac{r}{2a} \sum_{\mu=\pm 1}^{\pm 4} U_\mu(n)_{ab}\delta_{n+\hat{\mu},m} - \delta_{ab}\delta_{n,m}. \qquad (2.16)$$

The factor r is a free parameter which has no effect on the continuum limit of observables. As such, it is typically set to $r = 1$, giving the form of Eq. 2.17. The Wilson term acts like an additional mass term, causing the mass of doublers to get infinitely large in the continuum limit, decoupling them from the theory and solving the problem. This leads to the use of the so-called Wilson Dirac operator [15], given by,

$$D^{(f)}(n|m)_{\underset{ab}{\alpha\beta}} = \left(m^{(f)} + \frac{4}{a}\right)\delta_{\alpha\beta}\delta_{ab}\delta_{nm} - \frac{1}{2a}\sum_{\mu=\pm 1}^{\pm 4}(\mathbb{1} - \gamma_\mu)_{\alpha\beta}U_\mu(n)_{ab}\delta_{n+\hat{\mu},m}, \qquad (2.17)$$

with $\gamma_{-\mu} = -\gamma_\mu$ and the nearest neighbour terms are made gauge invariant by the insertion of link variables. The Wilson action can then be defined as,

$$S_{Wilson} = \sum_f a^4 \sum_{n,m\in\Lambda} \sum_{a,b,\alpha,\beta} \bar{\psi}^{(f)}(n)_{\underset{a}{\alpha}} D^{(f)}(n|m)_{\underset{ab}{\alpha\beta}} \psi^{(f)}(m)_{\underset{b}{\beta}}, \qquad (2.18)$$

with the Wilson Dirac operator inserted. For more details on the Wilson action, see Ref [13]. Wilson fermions are one method used to represent fermions on the lattice, and while it is the one employed in this study other methods exist. Staggered fermions [16], domain-wall fermions [17] and twisted mass fermions [18] are all alternative approaches to representing fermions on the lattice.

The gauge action, or gluon action, can be written as

$$S_G[U] = \frac{2}{g^2} \sum_{n\in\Lambda} \sum_{\mu<\nu} \mathrm{Re\,tr}[\mathbb{1} - U_{\mu\nu}(n)], \qquad (2.19)$$

with $U_{\mu\nu}$ being the so-called plaquette, which is the shortest closed loop on the lattice, and is defined as a product of link variables, $U_{\mu\nu}(n) = U_\mu(n)U_\nu(n+\hat{\mu})U_\mu(n+\hat{\nu})^\dagger U_\nu(n)^\dagger$. It is of the form shown in Figure 2.2.

In discretising the fermion and gluon actions, effects are of course introduced. In the formalism above, the discretisation effects for the Wilson fermion action are $\mathcal{O}(a)$, due to the addition of the Wilson term. For the gauge fields the discretisation effects are $\mathcal{O}(a^2)$. These effects only disappear in the continuum limit, meaning that on the lattice, they can be quite significant. One way to address this issue is through the Symanzik
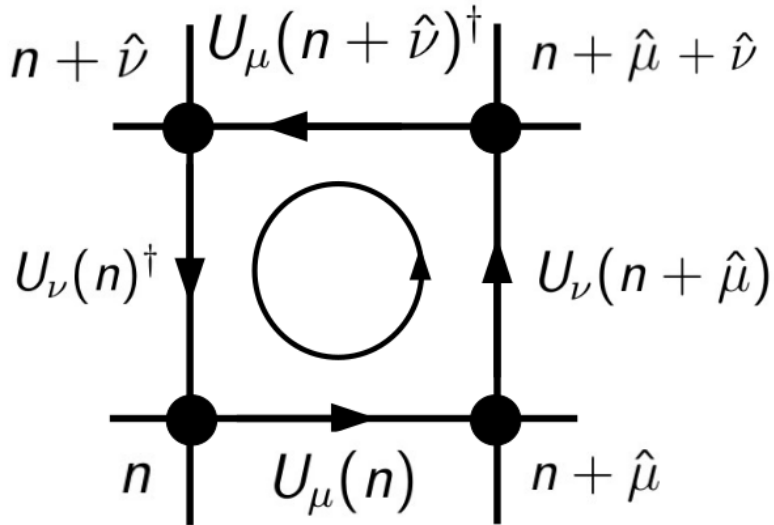
Figure 2.2: The link variables that make up the plaquette $U_{\mu\nu}(n)$.

improvement program [19]. This is a method of improving the order of discretisation effects by adding extra irrelevant counter-terms to the action, to counteract the leading order contribution. In the case of the Wilson fermion action, $\mathcal{O}(a)$ improvement is obtained by employing Symanzik improvement. This leads to the so-called Wilson clover action, which is given by

$$S_F = S_{Wilson} + c_{SW} a^5 \sum_{n \in \Lambda} \sum_{\mu < \nu} \bar{\psi}(n) \frac{1}{2} \sigma_{\mu\nu} \hat{G}_{\mu\nu} \psi(n), \qquad (2.20)$$

with $\hat{G}_{\mu\nu}$ being a discretised version of the gluonic field strength tensor, and $\sigma_{\mu\nu} \equiv [\gamma_\mu, \gamma_\nu]/2i$. The real coefficient c_{SW}, is known as the Sheikholeslami-Wohlert coefficient [20]. This extra term is quite often referred to as the clover term, due to the clover-like shape of the plaquettes it introduces. By tuning the coeffiecents of the action, $\mathcal{O}(a)$ improvement is realised. A similar procedure can be performed on the gluonic action, removing the $\mathcal{O}(a^2)$ discretisation effects. This is known as the Lüscher-Weisz gauge action. For details on this, see Ref [21].

Other methods for improving actions include stout-smearing gauge links and tadpole improvement. Stout-smearing is a type of smoothing procedure applied to space links to help suppress excited gluon modes. The new link after smearing is given by $\tilde{U}_\mu(n) = e^{iQ_\mu(n)} U_\mu(n)$, where $Q_\mu(n)$ is a traceless Hermitian matrix. For more details see Ref [22]. Tadpole improvement is a method of normalising the gauge links to eliminate UV

divergences caused by self-interactions of gauge fields. The link variables are divided by a tadpole factor, determined through perturbative or non-perturbative tuning. In this work, a tree-level tadpole term is used. For more details see Ref [23].

2.4 The Path Integral

Using the Euclidean discretised actions discussed above, one can define a partition function, Z, by

$$Z = \int \mathcal{D}[\psi, \bar{\psi}] \mathcal{D}[U] e^{-S_F[\psi, \bar{\psi}, U] - S_G[U]}, \tag{2.21}$$

with the fermion product measure

$$\mathcal{D}[\psi, \bar{\psi}] = \prod_{n \in \Lambda} \prod_{f, \alpha, a} d\psi^{(f)}(n)_\alpha^a d\bar{\psi}^{(f)}(n)_\alpha^a, \tag{2.22}$$

and the gauge field product measure

$$\mathcal{D}[U] = \prod_{n \in \Lambda} \prod_{\mu=1}^{4} dU_\mu(n), \tag{2.23}$$

where dU is the Haar measure on the group manifold of SU(3). The expectation value of an observable O can then be obtained by

$$\langle O \rangle = \frac{1}{Z} \int \mathcal{D}[\psi, \bar{\psi}] \mathcal{D}[U] s^{-S_F[\psi, \bar{\psi}, U] - S_G[U]} O[\psi, \bar{\psi}, U] \tag{2.24}$$

where O may be the product of multiple terms. For the fermionic part of the integral, ψ and $\bar{\psi}$ must be anticommuting to include Pauli's principle, which means they are now Grassmann numbers and Grassmann integration must be performed to compute the fermionic integral. Performing Gaussian integration with Grassmann variables gives the result

$$\int \mathcal{D}[\psi, \bar{\psi}] e^{-S_F[\psi, \bar{\psi}, U]} = \det D, \tag{2.25}$$

with D being the Dirac matrix. Note the determinant is calculated over all indices (flavour, color and spin) as well as all sites. This result allows for the fermionic part of the partition function to be integrated out, giving

$$Z = \int \mathcal{D}[U] e^{-S_G[U]} \det D. \tag{2.26}$$

Integrals with the fermionic action over operators with products of the same numbers of quarks and anti-quarks can be solved analytically. The simplest example of this is

over the operator $\psi(n)_{\underset{a}{\alpha}}\bar\psi(m)_{\underset{b}{\beta}}$;

$$\int \mathcal{D}\psi(n)_{\underset{a}{\alpha}}\bar\psi(m)_{\underset{b}{\beta}}e^{-S_F[\psi,\bar\psi,U]} = \det D\, D^{-1}(n,m)_{\underset{ab}{\alpha\beta}}. \tag{2.27}$$

If there is not an equal number of quarks and anti-quarks in the product, the expectation value vanishes. Thus the expectation value of a general operator O becomes

$$\langle O \rangle = \frac{1}{Z}\int \mathcal{D}[U]s^{-S_G[U]}\det D\, O[U,D^{-1}]. \tag{2.28}$$

D^{-1} is the quark propagator, and only depends on the gauge link U. Thus the dependence on the quark fields has been integrated out. Unfortunately, the remaining gauge integral cannot be solved analytically, and must instead be done numerically.

2.5   Numerical Methods

Instead of integrating, one generates a set of N configurations and samples from each of them, with the expectation value of O becoming

$$\langle O \rangle = \lim_{N\to\infty}\frac{1}{N}\sum_{n=1}^{N}O[U_n,D^{-1}[U_n]]. \tag{2.29}$$

Each U_n is sampled according to a probability distribution

$$dP(U) = \frac{1}{Z}\mathcal{D}[U]e^{-S_G[U]}|\det D|. \tag{2.30}$$

This is known as importance sampling Monte Carlo integration. Of course, one cannot make infinite gauge configurations. So instead the expectation value is approximated by the mean of a finite set. Define $O_n = O[U_n,D^{-1}[U_n]]$ as the estimate of the value of the operator based on a single configuration U_n. One can then define the mean $\bar{O}$ and variance σ^2 of the ensemble as

$$\bar{O} = \frac{1}{N}\sum_{n=1}^{N}O_n, \tag{2.31}$$

and

$$\sigma^2 = \frac{1}{N(N-1)}\sum_{n=1}^{N}(O_n - \bar{O})^2. \tag{2.32}$$

The mean is taken as an estimate of the expectation value of O, with uncertainty of the order $\mathcal{O}(1/\sqrt{N})$. The generation of these configurations is done with a so-called Markov

chain. The gauge configurations are generated subsequently, with each configuration U_n being the input for the next U_{n+1}. A number of changes are proposed to the input U_n, with changes being accepted with a probability that is proportional to the change they cause to the action. One begins measuring when the system reaches equilibrium.

Generating configurations in this way leads to a problem known as autocorrelation. This is where each calculation of an observable is correlated to the previous calculations performed. This problem arises in Markov chains as each configuration is generated from the previous one. There are many ways to attempt to combat this, such as only sampling from every n configurations, or grouping configurations into bins of size n and taking the average measurement in each bin as an independent measurement. The choice of n in these instances is very important, as for too small an n, measurements will still be correlated, but for too large an n, one may not have enough configurations for a suitable number of independent measurements to be made, restricting the ability to perform meaningful statistical analysis. Thus, calculating the so-called autocorrelation length, is quite important, allowing for a suitable choice of n. For an example of the investigation of autocorrelation on lattice ensembles in a spectroscopy study, and the calculation of autocorrelation length, see Ref [24].

One can determine the statistical errors of these numerical calculations, which includes these autocorrelation effects, using resampling techniques, examples of which are bootstrap and jackknife resampling. In this work, jackknife resampling was used, which is only valid on independent data. The procedure is as follows; Take a set of N measurements. Perform whatever analysis is required to gain the desired result, e.g. applying a fitting function to the obtained measurements. Obtain a result x. Now remove the first measurement, leaving N-1 measurements. Repeat the analysis on this new set, giving x_1. Repeat this process, removing one measurement at a time and calculating x_i, $i = 1, ..., N$. The statistical error is then estimated by

$$\sigma^2 = \frac{(N-1)}{N} \sum_{i=1}^{N} (x_i - x)^2.$$

(2.33)

Ensembles used in Chapters 4, 5 and 6 were generated using a Hybrid Monte Carlo method [25] following the standard procedure employed by the Hadron Spectrum collaboration. In generating these ensembles the determinant of the Dirac operator must be calculated repeatedly. Typically only the light and strange quarks are considered in this calculation of the determinant, the ensembles are said to have (2+1) flavours of dynamical quarks. The heavier quarks are omitted as their contributions are assumed to be negligible compared to the light quark contributions. This is further motivated when

comparing to works that included the charm quark as a dynamical quark [26, 27] and noting little difference in spectroscopy results to lattices with (2+1) flavours of dynamical quarks. A final note about these numerical calculations is that they were performed on anisotropic lattices. These are lattices where the spatial spacing a_s does not equal the temporal spacing a_t. The temporal spacing is finer than the spatial one, $a_t < a_s$. The finer temporal spacing is advantageous in lattice spectroscopy, it reduces cutoff effects related to the temporal lattice spacing and allows for more precise determination of correlations over a small time-scale. To use these lattices, the action must be split into a spatial action and a temporal action. Details of the anisotropic action used, and its tuning, can be found in Ref [28].

3 Spectroscopy

In this chapter, the theory and methods for the calculation of hadron spectra will be covered. In addition, scattering theory will be reviewed, and the method used in this thesis to relate finite-volume spectra calculated on a lattice to the infinite volume scattering amplitudes will be discussed. In the determination of a mass spectrum, the correlation function of an operator $\mathcal{O}$ is studied. As long as operators which transform irreducibly according to the relevant symmetries are used, only states which transform similarly will be produced, no additional eigenstates of the QCD Hamiltonian will be created. The Euclidean 2 point correlator is given by

$$
\begin{aligned}
C(t) &= \langle \mathcal{O}(0, t)\mathcal{O}^\dagger(0, 0)\rangle \\
&= \sum_{k=1}^{\infty}\langle 0|e^{Ht}\mathcal{O}e^{-Ht}|k\rangle\langle k|\mathcal{O}^\dagger|0\rangle \\
&= \sum_{k}\langle 0|\mathcal{O}|k\rangle\langle k|\mathcal{O}^\dagger|0\rangle e^{-tE_k},
\end{aligned}
\tag{3.1}
$$

where in the second line, a sum over a complete basis of eigenstates has been inserted. The final expression is the form of a spectral sum. The operator $\mathcal{O}^\dagger(0, 0)$ creates the state of interest at euclidean time $t = 0$. This state is annihilated at time t by $\mathcal{O}(0, t)$. Note that the above expression holds for infinite time extent. In the infinite time limit, the correlator becomes dominated by the term $\langle 0|\mathcal{O}|0\rangle\langle 0|\mathcal{O}^\dagger|0\rangle e^{-tE_0}$. Here E_0 is the energy of the lowest state in the spectrum, known as the ground state energy. Extracting the ground state energy from the correlator is thus quite straightforward in the infinite time limit. On the lattice however, there is a finite time extent, meaning that terms proportional to the energies of other states still contribute. There are also extra terms added to the correlator, of the form $e^{-(T-t)E_k}$, to account for the lattice boundary conditions, which are also relevant. The methods used to disentangle the energies of different states from correlators on the lattice will be outlined in this chapter, starting with a discussion on the operators, $\mathcal{O}$.

3.1 Hadron Operators

Constructing good operators, $\mathcal{O}$, to represent states of interest on the lattice is important. One wants to maximise the overlap an operator has on the state it represents, and reduce noise where possible. Good operators have a definite momentum, $\vec{P}$, and transform according to the symmetries discussed in the previous chapter. Note on the lattice, momentum is typically labelled $[\vec{d}]$, where $P = 2\pi\vec{d}/L$. Operators are constructed following the prescription described in Ref [29]. For this work, the main focus is on mesons.

3.1.1 Meson Operators

Mesons are states consisting of a quark, anti-quark pair $q\bar{Q}$, where the quark and anti-quark are not necessarily the same flavour. Mesons are color neutral. The simplest form of a meson operator on the lattice is given by

$$O_M(n) = \bar{\psi}^{(f_1)}(n)\Gamma\psi^{(f_2)}(n), \tag{3.2}$$

for flavours f_1, f_2. Here, Γ represents a monomial of gamma matrices, the choice of which helps determine the continuum J^{PC} of the meson the operator represents. However, these operators are quite limited, only giving access to spin $J = 0, 1, 2$, and offering little redundancy in each J^{PC} combination. For this reason, so-called forward-backward gauge covariant derivatives are also included in Γ. These allow access to states with higher angular momentum. They are given by

$$\overleftrightarrow{D}(n) = \overleftarrow{D}(n) - \overrightarrow{D}(n). \tag{3.3}$$

These derivatives are normally applied to the second quark, $\psi^{(f_2)}$. To use these on the lattice, one must form a circular basis of cartesian-vector-like derivatives and gamma matrices, of the form

$$O_{m=\pm1} = \mp\frac{i}{\sqrt{2}}\left(O_1 \pm iO_2\right),$$
$$O_{m=0} = iO_3, \tag{3.4}$$

which transforms like spin 1. With this basis established, operators of definite spin can be constructed using SO(3) Clebsch-Gordan coefficients. An example of such an operator, with one forward-backward derivative, looks like

$$\Gamma^{J,M} = \sum_{m_1,m_2} \langle J_1, m_1; J_2, m_2 | J, M \rangle \Gamma^{J_1,m_1} \overleftrightarrow{D}^{J_2,m_2}. \tag{3.5}$$

16

This can have continuum spin $J = 0, 1, 2$. To gain access to higher angular momentum, more derivatives are added. When this is done, the gauge covariant derivatives are coupled together to a definite spin J_D, before they are coupled to $\Gamma^{J,M}$. In this work, up to three of these derivatives are used in a given operator, giving access up to continuum spin $J = 4$. Finally, it is desirable that these operators create states at a definite momentum. Adding this final piece, the operator for a meson with definite momentum, $\vec{P}$, and spin, J, can be written as

$$(O^\dagger)^{J,M}(\vec{P}, \vec{t}) = \sum_{\vec{x}} e^{i\vec{P}\vec{x}} \bar{\psi}^{(f_1)}(\vec{x}, \vec{t}) \Gamma^{J,M} \psi^{(f_2)}(\vec{x}, \vec{t}). \tag{3.6}$$

Note, to use these operators on the lattice, one must go from the rotational symmetry in Euclidean space-time to the lattice, reducing the symmetry of the system to that of a cube. The labelling of states by J^P is replaced by the irreducible representations (irreps) of the cubic group O_h, as discussed in the previous section. Thus the continuum operators must be subduced into the lattice irreps. A subduced operator into the lattice irrep Λ is given by the equation

$$(O^\dagger)^{[J]}_{\Lambda,\lambda} = \sum_{M} S^{J,M}_{\Lambda,\lambda} (O^\dagger)^{J,M}, \tag{3.7}$$

with λ being the row within the irrep. $S^{J,M}_{\Lambda,\lambda}$ is known as a subduction coefficient, for more details see [29]. Note that the subduced operator carries the label $[J]$. Although it transforms within Λ, it has been shown to carry the "memory" of the continuum spin J from which it was subduced. This becomes a very useful property when attempting to identify lattice states with their continuum ones.

3.1.2 Meson-Meson Operators

When investigating meson-meson scattering, it is important to have operators that can represent the resulting states. This motivates the necessity for meson-meson operators. These are formed by combining two single-meson operators, using the appropriate Clebsch-Gordon coefficients, and summing over all allowed momenta that add to give the desired total momentum $\vec{P}$. These operators take the form

$$(O^\dagger)^{\Lambda,\lambda}(\vec{P}) \sum_{\substack{\vec{k}_i \in (\vec{k}_i)^* \\ \vec{k}_1 + \vec{k}_2 = \vec{P}}} \sum_{\lambda_1, \lambda_2} C(\vec{P}\Lambda\lambda; \vec{k}_1\Lambda_1\lambda_1; \vec{k}_2\Lambda_2\lambda_2) O^\dagger_{\Lambda_1,\lambda_1}(\vec{k}_1, \vec{t}) O^\dagger_{\Lambda_2,\lambda_2}(\vec{k}_2, \vec{t}), \tag{3.8}$$

where $(\vec{k}_i)^*$ means all momenta related to $\vec{k}_i$ by allowed lattice rotations R. Enforcing that $\vec{k}_1 + \vec{k}_2 = \vec{P}$ is the equivalent of requiring $R \in LG(\vec{P})$, where $LG(\vec{0}) = O_h$ For

more details on meson-meson operator construction, see Ref [30].

3.1.3 Hybrid Meson Operators

Operators can be constructed for many hadron states, from baryons to the exotic glueball and tetraquark states. None of these are relevant for this study. However the exotic state known as a hybrid meson is relevant. This is a state composed of the usual mesonic quark-antiquark pair but combined with excited gluons in their structure. These excited gluons provide extra internal degrees of freedom, allowing the hybrid mesons to exist with exotic quantum numbers, which are quantum numbers not allowed in the quark model for ordinary mesons. Hybrid mesons provide an insight into the strong force, and the gluons that carry it. The simplest operators to represent hybrid mesons are those consisting of the commutator of 2 covariant derivatives, proportional to the field-strength tensor, $O \approx \bar{\psi} G^{\mu\nu} \psi$. The simplest forms of these operators look like $\left(\pi \times D_{J=1}^{[2]} \right)^J$ and $\left(\rho \times D_{J=1}^{[2]} \right)^J$, where π and ρ are given by γ_5 and γ_i respectively. Operators of this type are used in Chapter 5. For more details on hybrid meson operators, see Refs [31, 32]

3.2 Quark Sources, Smearing and Distillation

A complete quark propagator matrix is quite large. While the Dirac operator D may be sparse depending on the action, its inverse D^{-1} is not. It contains $\mathcal{O}(10^{12})$ complex entries, being a large memory cost to store and often quite wasteful to fully compute. Each entry of the propagator D^{-1} connects a so-called source point to a sink point, referring to both the site on the lattice and the Dirac and color indices. Following the notation used in Ref [13], the propagator takes the form

$$D^{-1}(n|m_0)_{\substack{\beta\alpha_0 \\ ba_0}} = \sum_{m,\alpha,a} D^{-1}(n|m)_{\substack{\beta\alpha \\ ba}} S_0^{m_0,\alpha_0,a_0}(m)_{\substack{\alpha \\ a}}, \tag{3.9}$$

for a given source point (m_0, α_0, a_0). Here the so-called point sources have been introduced, and are given by

$$S_0^{m_0,\alpha_0,a_0}(m)_{\substack{\alpha \\ a}} = \delta(m - m_0)\delta_{\alpha\alpha_0}\delta_{aa_0}. \tag{3.10}$$

The point sources are placed at the source interpolator $\bar{O}_H(m_0)$ at position m_0. The column $D^{-1}(n|m_0)$ then propagates to the sink operator $O_H(n)$ at position n. Now, due to the presence of an antiquark in mesons, one might expect that a propagator in the

18

opposite direction would be required. However, no such computation is necessary, thanks to the γ_5-hermicity of the Dirac operator, and therefore its inverse $\left((D^{-1})^{\dagger} = \gamma_5 D^{-1} \gamma_5\right)$. This allows the backward propagator to be obtained simply by

$$D^{-1}(n|m_0)_{\underset{ba}{\beta\alpha}} = (\gamma_5)_{\alpha\alpha'} D^{-1}(m_0|n)_{\underset{ab}{\alpha'\beta'}} (\gamma_5)_{\beta'\beta}. \tag{3.11}$$

When performing these types of calculations, clear and strong correlator signals are greatly desired. It has been found that the overlap of operators onto states can be greatly improved by providing more realistic spatial wave functions, that describe the quantum state of the system and govern the probabilities of various outcomes. So far, only point sources have been considered. A more general meson operator located at a spatial lattice site n_0 for a fixed time slice can be written as

$$O(n_0) = \sum_{n_1, n_2} F(n_0; n_1, n_2) \bar{\psi}_1(n_1) \psi_2(n_2), \tag{3.12}$$

with quark fields $\bar{\psi}_1, \psi_2$ and a distribution function F, which combines the field values at site n_1 and n_2 which are in the vicinity of n_0. The sum is over all lattice sites for the fixed time slice. Typically, a form of F using factorizable functions is used, which is of the form

$$F(n_0; n_1, n_2) = S_1(n_0, n_1) \Gamma S_2(n_0, n_2), \tag{3.13}$$

where Γ is a monomial of Dirac gamma matrices and forward backward derivatives, as discussed in the previous chapter, and $S_i(n_0, n_i)$ are the quark source functions. By defining so-called smeared fermions in terms of these smeared quark sources, given by

$$\begin{aligned} \tilde{\psi}_2(n_0) &\equiv \sum_{n_2} S_2(n_0, n_2) \psi_2(n_2), \\ \tilde{\bar{\psi}}_1(n_0) &\equiv \sum_{n_1} S_2(n_0, n_1) \bar{\psi}_1(n_1), \end{aligned} \tag{3.14}$$

the operator simplifies down to a familiar form

$$O(n_0) = \tilde{\bar{\psi}}_1(n_0) \Gamma \tilde{\psi}_2(n_0). \tag{3.15}$$

The problem becomes a linear system of equations of the form $DG = S$, with S the smeared source and G the propagator desired. The smearing operator is only applied in space. If one were to use a smearing function that is not gauge-covariant, the gauge would need to be fixed on each time slice. For this reason, gauge-covariant smeared sources are used. A process that works well in creating these sources is Jacobi smearing, which gives the source a shape similar to a Gaussian function. A particularly effective

smearing operator for this process is the gaussian-smearing operator, as explained in the literature [33]. This operator is given by

$$\Box(n_\alpha; \alpha) = \left(1 + \frac{\alpha \nabla^2}{n_\alpha}\right)^{n_\alpha}, \tag{3.16}$$

with α and n_α being free tunable parameters and ∇^2 being the three-dimensional gauge-covariant Laplace operator. For large n, the smearing operator is $e^{\alpha \nabla^2}$. The smeared source is obtained by applying this operator to the point source S_0,

$$S(n_0) = \Box(n; \alpha) S_0(n_0). \tag{3.17}$$

The parameter α controls the width of the smearing. For the choices of α used, higher eigenmodes of the lattice Laplace operator are strongly suppressed, with only the first N_d contributing significantly. This leads to a technique known as distillation [34]. The distillation operator is defined as

$$\Box(n_1, n_0; t) = V(n_1; t) V^\dagger(n_0; t), \tag{3.18}$$

where $V(t)$ is a matrix of dimension $N_d \times N_S \times N_c$. For an extended creation operator at source and sink $A(n_1, n_0)$, a correlator can be projected into $N_d \times N_d$ dimensions giving

$$C(t, t') = Tr[\Phi_A(t) \tau(t, t') \Phi_A(t') \tau(t', t)], \tag{3.19}$$

where

$$\Phi_A(t) = V^\dagger(n_1; t) A(n_1, n_0, t) V(n_0; t) \tag{3.20}$$

and

$$\tau(t, t') = V^\dagger(n_1; t) D^{-1}(n_1, t; n_0, t') V(n_0; t'). \tag{3.21}$$

$\tau(t, t')$ is known as a perambulator. It connects distillation spaces on two time slices. Using distillation, only N_d, $0 < N_d < N$, solutions of the original problem are required. The choice of how many distillation vectors one uses, N_d, affects the smearing. The higher it is, the less smeared the sources are. The choice of N_d also affects computing cost, and as such should be tuned appropriately for the volume being worked in. The cost of distillation grows with spatial volume. To maintain a constant resolution in the distillation space, the computing cost of inverting the Dirac matrix scales with the square of the volume of the lattice, V^2.

3.3 Computing the Spectrum

Using Eqn 3.1, one can define an effective mass as $m_{eff}(t + 1/2) = ln(\frac{C(t)}{C(t+1)})$. Using this, one can figure out the range of t for which $C(t)$ is dominated by the lowest energy state, known as the ground state. It is only at large t that the correlator is dominated by the ground state. Using this fact, one can extract the ground state energy from the correlator by fitting to a single exponential at large t, with the appropriate range of t determined from an effective mass curve. However, this only holds up to $t = T/2$, due to back-propogating contributions. At smaller t, many more states provide significant contributions. In theory, one could simply fit a function in the form of a sum of K exponentials,

$$C(t) = \sum_{k=1}^{K} c_k e^{-tE_k} \tag{3.22}$$

to the correlator to determine the first K states. However, while this method would work in theory, as well as needing more data points than free parameters being fitted, in practice one would require exact values of the correlator $C(t)$, which one doesn't have when performing a Monte Carlo simulation, the data has statistical errors. Some methods have been proposed to try and get past this, there has been success with Bayesian techniques such as in Ref [35]. Typically, in spectroscopy studies, one is aiming to determine a number of excited states, some of which can be nearly degenerate in energy. A reliable method to determine the masses of excited states on the lattice, is knows as the variational method, Refs [10, 36, 37].

3.3.1 The variational method

The central idea is to construct a matrix of correlators of the form

$$C_{ij}(t, 0) = \langle \mathcal{O}_i(0, t) \mathcal{O}_j^\dagger(0, 0) \rangle = \sum_k \langle 0 | \mathcal{O}_i | k \rangle \langle k | \mathcal{O}_j^\dagger | 0 \rangle e^{-E_k t}, \tag{3.23}$$

for a basis of N interpolating operators, all with the quantum numbers of the states to be studied and a definite momentum. The indices i, j run from $i, j = 1, ..., N$, and the parameter t_0 is a free parameter, that must take a value between 0 and t. The correlation function has a spectral decomposition,

$$C_{ij}(t) = \sum_n \frac{Z_i^{n*} Z_j^n}{2E_n} e^{-E_n t} \tag{3.24}$$

21

with operator overlaps defined as

$$Z_i^{\mathfrak{n}} \equiv \langle \mathfrak{n} | \mathcal{O}_i^{\dagger} | 0 \rangle$$
$$Z_i^{\mathfrak{n}*} \equiv \langle 0 | \mathcal{O}_i | \mathfrak{n} \rangle$$

(3.25)

Diagonalising this matrix allows one to disentangle the physical states to some degree, finding eigenvalue behaviour to be

$$\lambda^{\mathfrak{n}}(t, t_0) \propto e^{-E_{\mathfrak{n}}(t-t_0)}(1 + \mathcal{O}(e^{-\Delta E_{\mathfrak{n}}(t-t_0)})),$$

(3.26)

where $\Delta E_{\mathfrak{n}}$ is the distance of $E_{\mathfrak{n}}$ to nearby levels, and t_0 is a free parameter known as the metric timeslice. A better method however, starts by defining a vector $v^{\mathfrak{n}}$ such that

$$\sum_{i=1}^{N} \frac{Z_i^{\mathfrak{m}}}{\sqrt{2E_{\mathfrak{n}}}} v^{\mathfrak{n}} = \delta_{\mathfrak{mn}}.$$

(3.27)

This implies

$$\sum_{j=1}^{N} C_{ij}(t) v_j^{\mathfrak{n}} = \sum_{m=1}^{N} \sum_{j=1}^{N} \frac{Z_i^{\mathfrak{m}*} Z_j^{\mathfrak{m}}}{2E_{\mathfrak{n}}} v_j^{\mathfrak{n}} e^{-E_{\mathfrak{n}}t}$$
$$= \frac{Z_i^{\mathfrak{n}*}}{\sqrt{2E_{\mathfrak{n}}}} e^{-E_{\mathfrak{n}}t}.$$

(3.28)

By introducing the time $t_0 < t$, the problem is recast as a generalised eigenvalue problem (GEVP),

$$C_{ij}(t) v_j^{\mathfrak{n}} = \lambda^{\mathfrak{n}}(t, t_0) C_{ij}(t_0) v_j^{\mathfrak{n}},$$

(3.29)

where $v^{\mathfrak{n}}$ is an eigenvector of $C^{-1}(t_0)C(t)$ with eigenvalue $\lambda^{\mathfrak{n}}$. $\lambda^{\mathfrak{n}}$ is called the principal correlator of the $\mathfrak{n}^{th}$ state. To actually extract the energies of the spectrum, the principal correlator is fitted to a sum of exponentials of the form

$$\lambda_{\mathfrak{n}}(t) = (1 - A_{\mathfrak{n}})e^{-E_{\mathfrak{n}}(t-t_0)} + A_{\mathfrak{n}} e^{-E_{\mathfrak{n}}'(t-t_0)},$$

(3.30)

with free parameters $E_{\mathfrak{n}}$, $E_{\mathfrak{n}}'$ and $A_{\mathfrak{n}}$. Here $m_{\mathfrak{n}}$ is the energy of the state of interest, and the other free parameters help account for contamination by excited states. The second exponential term is not always included. In practice, a range of t_0's are fitted and compared to ensure robustness in the extracted energies with respect to the free parameter. The eigenvector, $v^{\mathfrak{n}}$, associated with the principal correlator $\lambda_{\mathfrak{n}}$, contains the coefficients of the linear combination of operators that best interpolates the nth state. The overlap factor depends on this eigenvector [29], and is given by

$$Z_i^{\mathfrak{n}} = \sqrt{2E_{\mathfrak{n}}} C(t_0) v_i^{\mathfrak{n}*} e^{E_{\mathfrak{n}} t_0/2}$$

(3.31)
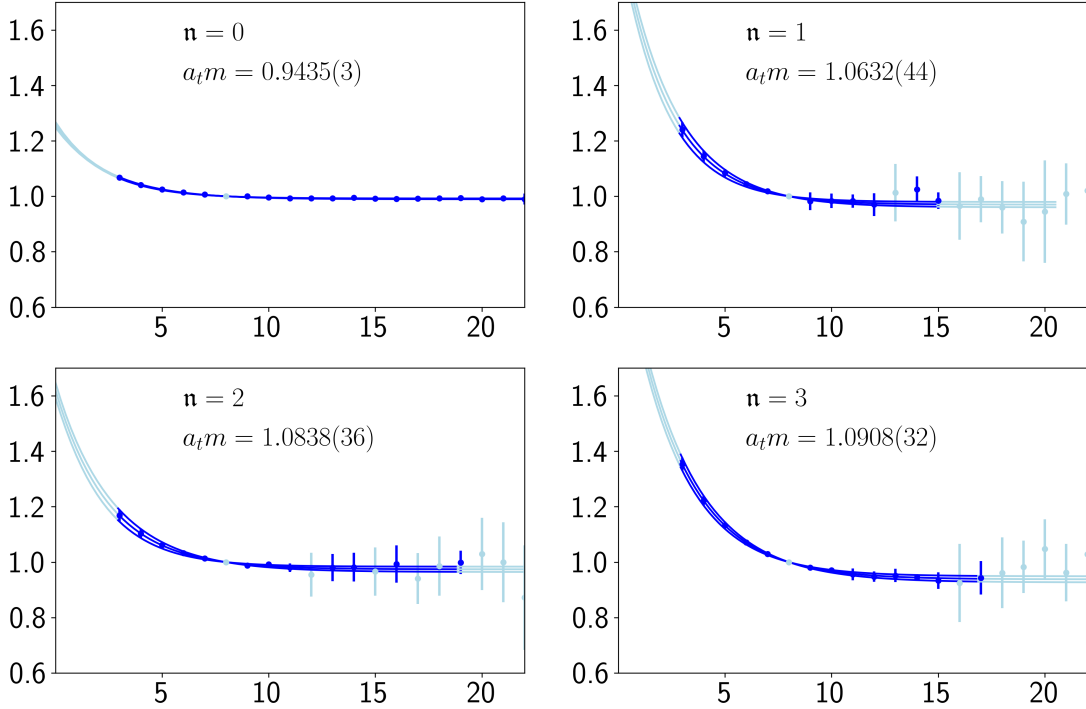
Figure 3.1: Principal correlator fits for the first 4 states, $\mathfrak{n} = 0, ..3$, in T_1^- for the B meson. Shown is $e^{E_n(t-t_0)}\lambda_n(t)$ plotted against t/a_t. Darker points are included in the fits while the lighter ones are not. More details on results discussed in Chapter 5

This overlap factor is very useful for differentiating between nearby states and for classifying the state in the continuum. An example of such a principal correlator fit is shown in Figure 3.1. This shows the fits, and corresponding energies calculated, of the first 4 states in the T_1^- irrep for the B meson. The darker points were included in the fit while the lighter ones were not, and the correlator is normalised such that it approaches 1 asymptotically.

3.3.2 Continuum state classification

First, it is important to note here how the lattice eigenstates are labelled. Rotational symmetry is broken on the lattice due to the finite spatial cubic volume and lattice spacing. Thus the lattice eigenstates are labelled by the irreducible representations (irreps) of the little group $LG(\vec{P})$ when at non-zero momentum $\vec{P}$ and the cubic group O_h when at zero momentum. Focusing on at rest states, for each parity and charge-conjugation, there are five lattice irreps. Continuum spin J subduces into these irreps as shown in Chapter 2, in Table 2.1.

As discussed previously, operators are constructed to have a definite continuum spin J. Correlation functions are created using a basis of operators for each irrep. Once

energies are calculated from the principal correlator fits, the operator overlaps, related to the associated eigenvector, allow for the identification of the continuum spin of the state. By examining the relative strength of the overlaps in the basis of operators for a given state, the continuum spin of the dominant operator(s) is assigned to the state. Notably, as shown in Table 2.1, continuum spins $J \geq 2$ subduce into multiple lattice irreps. This leads to multiple lattice irrep states corresponding to the same continuum J state, yielding, for example, two continuum spin $J = 2$ states, one from the T_2 lattice irrep, and from the the E lattice irrep. Again, examining the operator overlaps allows for clarity. If a state in T_2 is of a similar mass to a state in E and they are both dominated by operators corresponding to continuum spin $J = 2$, one must look closer to determine whether they are in fact the same continuum J state. If the two lattice states are both representing the same continuum state, one would typically find that the dominant operators of each lattice state have a similar construction and operator overlap. This is particularly important when comparing two nearby excited states of the same spin, and trying to distinguish between them. Some examples of continuum spin classification can be found in Chapter 5.

Due to the construction of the operators, as discussed at the start of this chapter, one can determine whether a state is part of a spin multiplet. By comparing overlap of an operator constructed to represent a spin multiplet across multiple states, one can identify candidates for such a multiplet. These operators will typically have a similar overlap value in each of the states that are a part of the multiplet, even though those states span multiple lattice irreps.

Identifying hybrid mesons is also possible through the examination operator overlaps. Hybrid meson states should be created best by operators containing gluon fields, as discussed previously in this chapter. As such they can be identified in a given irrep, provided hybrid meson operators have been included in the basis of that irrep. One can even propose candidate states for hybrid supermultiplets, by comparing the hybrid operator overlap on different spins, in a similar way to the identification of spin multiplets. Examples of hybrid meson state and supermultiplet classification can be seen in Chapter 5.

This discussion has focused on single meson states at rest, but operator overlaps can be examined in a similar way for non-zero momentum states and even multi-meson states. In this case the dominant operator will tell you the constituent particle(s) of the lattice state obtained. This is particularly interesting when quark annihilation is allowed, leading to a basis of single and multi meson operators in each lattice irrep.

There is one more thing to note about classifying states on the lattice, and that is charge-conjugation. As discussed previously, the operator for a single meson takes the form of a quark bilinear, $\bar{\psi}\Gamma\psi$. Γ is constructed such that $\Gamma^T = \pm\Gamma$. The eigenvalue of Γ under this transformation is denoted C_Γ. If the quark and antiquark of the meson being studied have the same flavour, then this C_Γ corresponds to charge conjugation C. If the quark and antiquark are not the same flavour but are degenerate in mass, then C_Γ corresponds to a generalisation of C, known as G-parity. However if the constituent quark and antiquark of the meson being studied are neither the same flavour or mass degenerate, then states created by operators with opposite C_Γ can mix to form an eigenstate of the QCD Hamiltonian. This means that, for such a case, charge-conjugation is not a good quantum number. As the work covered in this thesis is studies of D, B, B_s and B_c, charge-conjugation is not a good quantum number in any of the following work and states can only be labelled by continuum spin and parity J^P.

3.4 Scattering Theory

So far, all particles in the spectra have been assumed to be stable. However many excited hadrons are not stable, they decay to lower energy more stable hadrons quite quickly. These hadrons are typically observed as intermediary states in a scattering process, and as such scattering amplitudes are of great interest. These unstable intermediary states appear as resonances in the amplitude, and identifying their masses and widths is highly desirable. While resonances may appear as an enhancement in the scattering amplitude, a more complete definition is that resonances are poles in the scattering amplitude that appear when it is analytically continued to complex values of energy. To discuss how scattering amplitudes are related to the energies determined on the lattice , first an overview of relevant continuum scattering theory will be provided. The **S**-matrix encodes an entire scattering process. The **S**-matrix is unitary, to ensure probability conservation, and maps a set of in-states to out-states. In QCD, the **S**-matrix is symmetric, due to time-reversal invariance. This allows for the **S**-matrix to be split into two parts, the non-interacting part and interacting part, which defines the **t**-matrix,

$$\mathbf{S} = \mathbf{1} + 2i\sqrt{\rho} \cdot \mathbf{t} \cdot \sqrt{\rho}, \tag{3.32}$$

with ρ a phase space factor. It is a diagonal matrix. In this work, only $2 \rightarrow 2$ meson scattering is considered, with inbound momentum p_i and outbound momentum k_i, as shown in Figure 3.2.

In this case, the elements of **t** are functions of the Mandelstam variables [38], which are
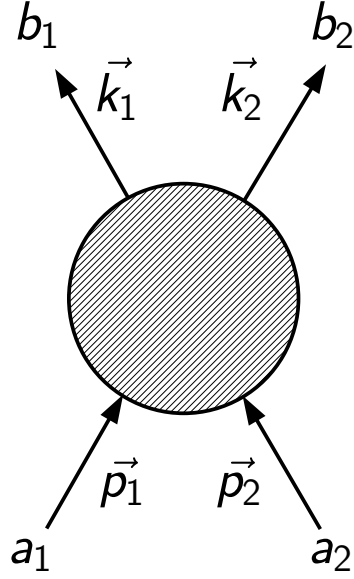
Figure 3.2: A diagram of a 2-2 scattering channel, with in states a_i and out states b_i, which have momenta p_i and k_i respectively.

defined as

$$
\begin{aligned}
s &= (p_1 + p_2)^2, \\
t &= (p_1 - k_1)^2, \\
u &= (p_1 - k_2)^2,
\end{aligned}
\tag{3.33}
$$

with $s + t + u = \sum_{i=1}^{4} m_i^2$. Note s,t, and u are not independent. With this basis, the entries of the phase space factor ρ can be defined $\rho(s) = 2k/\sqrt{s}$ The energy and momentum in the centre of momentum frame are given by

$$
\begin{aligned}
E_{cm} &= \sqrt{s}, \\
k(s) &= \frac{1}{\sqrt{4s}}\sqrt{(s - (m_1 + m_2)^2)(s - (m_1 - m_2)^2)}.
\end{aligned}
\tag{3.34}
$$

Each scattering channel defines a threshold energy, given by $E_{thr} = \sqrt{s_{thr}} = m_1 + m_2$. The scattering amplitude is given by elements of the **t**-matrix, $t_{ab}(s, t)$, but only at real values of $s > \max(s_{thr}^{(a)}, s_{thr}^{(b)})$, with (a) and (b) being the in and out states of the scattering process. It is convenient to expand **t** in a basis of partial waves

$$
t_{ab}(s, t) = \sum_l (2l + 1)P_l(\cos \theta(s, t))t_{ab}^l(s, t),
\tag{3.35}
$$

where $\theta(s, t)$ is the scattering angle and $t_{ab}^l(s)$ is the partial wave amplitude of the

channel, given by

$$t_{ab}^l(s) = \frac{1}{2i}\frac{1}{k}\int_{-1}^{1} P_l(\cos\theta)t_{ab}(s,t)d(\cos\theta). \tag{3.36}$$

This expansion is useful as for spinless scattering state, intermediate states with spin J contribute to only a single partial wave. For states with spin, partial waves and spins can mix, leaving only the overall angular momentum of the state conserved. The presence of a composite particle with angular momentum ℓ is indicated by a pole singularity in the partial-wave amplitude, of the form $\frac{r_{ab}}{m_r^2 - s}$. In the energy region of the mass of the particle $s \approx m_r$, the amplitude is dominated by this term. The residue can be factorized as $r_{ab} = g_a g_b$ giving couplings g_a, g_b to scattering channels, as shown in Ref [39]. More discussion on poles in scattering amplitudes will be given in Chapter 4.

3.4.1 Parameterising the t-matrix

When parameterising the **t**-matrix, it is important to consider any constraints on its properties. An important constraint is enforced by the unitarity of the **S**-matrix, giving the condition

$$\mathbf{t} - \mathbf{t}^\dagger = 2i\mathbf{t}\rho\mathbf{t}^\dagger. \tag{3.37}$$

For pseudoscalar-pseudoscalar scattering the **t**-matrix is block diagonal, due to the absence of coupling between partial waves in the continuum. In the following work, only elastic scattering is considered, which means the **t**-matrix is in fact diagonal. The parameterisation

$$t^\ell(s) = e^{i\delta^\ell}\sin(\delta^\ell)/\rho, \tag{3.38}$$

is suitable for partial wave ℓ with phase shift δ^ℓ and phase space factor $\rho = 2k/\sqrt{s}$. This fixes the imaginary part of the scattering amplitude to $\text{Im}[t^l] = -1/\rho$ and the real part to $\text{Re}[t^l = 1/(\rho\cot\delta^\ell)$.

Effective Range

One common parameterisation of the scattering amplitude is obtained by Taylor expanding the expression $k^\ell \cot\delta^\ell$ for the partial wave $\ell = 0$, giving

$$k\cot\delta = \frac{1}{a} + \frac{1}{2}r_0 k^2 + P_2 k^4 + \mathcal{O}(k^6), \tag{3.39}$$

which characterizes the scattering by a series of constants with a and r_0 being the scattering length and effective range. Truncating this expression to the first two terms is the effective range parameterisation. To treat higher partial waves, it is important to

build the correct threshold behaviour into the expression. In scattering, as momentum $p \to 0$, the wave function behaves $\approx p^{2\ell+1}$ [40]. It follows that near-threshold, $(t^\ell)^2 \approx (k^\ell)^2$. Thus the general expression for the effective range parameterisation is given by

$$k^{2\ell+1} \cot \delta^\ell = \frac{1}{a_\ell} + \frac{1}{2} r_\ell k^2 + \mathcal{O}(k^4). \tag{3.40}$$

Note, the threshold behaviour $(t^\ell)^2 \approx (k^\ell)^2$ is incorporated into all parameterisations of the **t**-matrix used in this work.

Breit-Wigner

For amplitudes with isolated resonances, the relativistic Breit-Wigner is often used. It is obtained by parameterising the phase shift as

$$\delta^I = \arctan\left(\frac{\sqrt{s}\,\Gamma_\ell(s)}{m_r^2 - s}\right) \tag{3.41}$$

with m_R being the so-called "Breit-Wigner mass" identified as the mass of the resonance, and Γ_ℓ being the width. With this phase shift, the scattering amplitude becomes

$$t^{(\ell)}(s) = \frac{1}{\rho(s)} \frac{\sqrt{s}\,\Gamma_{\ell(s)}}{m_R^2 - s - i\sqrt{s}\,\Gamma_{\ell(s)}}, \tag{3.42}$$

where the width is given by

$$\Gamma_\ell(s) = \frac{g_R^2}{6\pi} \frac{k^{2\ell+1}}{s\, m_R^{2(\ell-1)}}, \tag{3.43}$$

with g_R a coupling constant. This form for the width ensures the correct near-threshold behaviour.

K-matrix formalism

The parameterisation used most often in this work is the K-matrix formalism. This arises from rewriting the unitarity condition as

$$\left(t^\dagger\right)^{-1} - t^{-1} = 2i\rho. \tag{3.44}$$

A parameterisation that fulfils this condition is

$$t^{-1} = K^{-1} - i\rho,$$
$$t = K(1 - i\rho K)^{-1}. \tag{3.45}$$

K is a matrix comprised of functions of s that are real for real values of s. A variety of K-matrix parameterisation forms can be used, any polynomials in s satisfy the unitarity condition, as long as any poles included are of the form $\frac{r}{m_r^2 - s}$. To include the correct near-threshold behaviour in this formalism, the parameterisation is written as

$$(t^{(\ell)})^{-1}(s) = \frac{1}{(2k)^\ell} K^{-1}(s) \frac{1}{(2k)^\ell} + I(s), \qquad (3.46)$$

for a partial wave ℓ with phase factor $I(s)$. The factors $(2k)^{-\ell}$ ensure the expected threshold behaviour. Unitarity of the S-matrix is guaranteed if $\operatorname{Im} I(s) = -\rho(s)$ above threshold and zero below. This places no constraint on $\operatorname{Re} I(s)$. One choice is to set $\operatorname{Re} I(s)$ to zero, giving $I(s) = -i\rho(s)$. Another option is the Chew-Mandelstam prescription [41], which uses the known $\operatorname{Im} I(s)$ to determine $\operatorname{Re} I(s)$ through a dispersion relation. This has a better analytic structure, and the dispersion relation, which is an integral, is made finite by a subtraction at an arbitrary point. A general form of K-matrix parameterisations is,

$$K(s) = \frac{\left(g^{(0)} + g^{(1)}s\right)^2}{m^2 - s} + \gamma^{(0)} + \gamma^{(1)}s, \qquad (3.47)$$

where $g^{(n)}$, $\gamma^{(n)}$ and m are real free parameters that are fitted as described previously. Various parameters can be set to zero for different fits. When a pole parameter is used, the Chew-Mandelstam phase is subtracted at the pole, $s = m^2$. Another form of K-matrix parameterisation used is a ratio of polynomials

$$K^{-1}(s) = \frac{\sum_{n=0}^{N} c_n s^n}{1 + \sum_{m=1}^{M} d_m s^m}, \qquad (3.48)$$

where c_n and d_n are real free parameters. Although several low-order truncations of Eqn 3.48 are similar to the previous form of K-matrix in Eq 3.47, the parameter correlations can differ quite significantly and as such it is important to fit samples of both forms. When using this form of parameterisation, the Chew-Mandelstam phase is subtracted at threshold, $s = (m_1 + m_2)^2$.

3.4.2 From finite volume spectra to infinite volume scattering amplitudes

The spectrum calculated in a finite volume is discrete. Meanwhile, in reality, the spectra of particles is continuous in an infinite volume, due to the continuous momentum that particles have. To map between the finite-volume spectra obtained and the infi-

nite volume scattering amplitudes, the Lüscher quantisation condition [42–44] and its extensions [45–53] are used. The form used in this work is given by

$$\det\left[\mathbf{1} + i\rho(s) \cdot \mathbf{t}(s) \cdot (\mathbf{1} + i\mathcal{M}(s, L))\right] = 0, \tag{3.49}$$

where $\mathbf{t}(s)$ is the infinite volume $\mathbf{t}$-matrix which was defined above in equation 3.32. $\mathcal{M}(s, L)$ is a volume-dependent matrix of known energy functions. Its indices are the angular momenta J, M, J', M'. As such, a cutoff must be made at some maximal orbital angular momentum. It should be noted that Eqn 3.49 holds up to exponential finite-volume corrections. The solutions of the Lüscher quantisation condition for a given $t(s)$ is the specific finite-volume spectrum for that parameterisation. It should be noted that while this approach uses finite-volume symmetry breaking, it assumes that the symmetry breaking due to finite lattice spacing is negligible. With Eqn 3.49, the procedure for a lattice scattering calculation can finally be established. One first follows the previous sections to compute the finite-volume spectrum using suitable operators to represent the states interested in. Then, one must suitably parameterise the $\mathbf{t}$-matrix (discussed in section 3.4.1). With this, for a given set of input parameters, the solution of the Lüscher quantisation condition is a specific-finite volume spectrum. Through a fitting procedure, these input parameters can be tuned until the output matches the previously calculated finite-volume spectrum, thus obtaining the parameters of the $\mathbf{t}$-matrix representing the scattering amplitude. The application of this method, and results obtained from this procedure will be discussed in more detail in Chapters 4 and 6.

4 Isospin 1/2 $D\pi$ scattering

In this chapter, the determination of isospin-1/2 $D\pi$ scattering amplitudes is described. The calculation is relevant due to the long-standing puzzle that emerged with the experimental observation of the charm-light D_0^* and the charm-strange D_{s0}^* mesons. In the quark model, both meson are states with $J^P = 0^+$, with P-wave $q\bar{q}$ construction. A mass difference arises due to the different quark content of the two mesons. Surprisingly, the two hadrons were found experimentally to be of similar mass with very different widths, the D_0^* being very broad compared to the narrow D_{s0}^* [54–56]. This work, following the methodology outlined in Chapter 3, made a robust determination of the isospin-1/2 $D\pi$ scattering and offers a possible resolution to the puzzle.

This work was carried out on a single lattice of dimensions $(L/a_s)^3 \times (T/a_t) = 32^3 \times 256$ with a periodic boundary condition in space and an antiperiodic boundary condition in time for the quark fields. An anisotropic lattice is used with $a_t \ll a_s$. The anisotropy is given by $\xi \equiv a_s/a_t \approx 3.5$. An unphysical pion mass of 239 MeV is used in this study. The D_0^* was studied previously with HadSpec formalism at $m_\pi = 391$ MeV [2]. Studies of the D_{s0}^* exist for both pion masses, which included coupled-channel analysis [3]. Thus this work completes a series of studies, allowing for an investigation of the dependence of the results on the light quark mass. The energy scale was determined by demanding that the calculated Ω baryon mass obtained on the lattice corresponds to the physical value, giving $a_t^{-1} = 6.079$ GeV. This corresponds to $a_s = 0.11$ fm, giving a physical spatial lattice volume of $(3.6 \text{ fm})^3$ [57]. The strange quark in this study was tuned to approximate its physical value while the light quark mass is heavier than physical, such that $m_\pi = 239$ MeV. The charm-quark is calculated with the same tadpole-improved Wilson clover action as the strange and light quarks. The charm quark was tuned to reproduce the η_c mass and pion anisotropy in the pseudoscalar dispersion relation, which were previously determined in Refs [32, 58]. These parameters are used in this study. In Table 4.1 the relevant masses and thresholds for this calculation are listed.

	$a_t m$			$a_t E_\text{threshold}$
π	0.03928(18) [59]			
K	0.08344(7) [59]	$D\pi$	0.34851(21)	
η	0.09299(56) [59]	$D\pi\pi$	0.38779(27)	
D	0.30923(11) [58]	$D\eta$	0.40222(57)	
D_s	0.32356(12) [3]	$D_s\bar{K}$	0.40700(14)	
D^*	0.33058(24) [3]	$D^*\pi\pi$	0.40914(35)	
Ω	0.2751(6) [57]			

Table 4.1: A summary of the stable meson masses and kinematic thresholds relevant for this calculation. Masses were determined previously through dispersion relations.

4.1   Finite Volume Spectra

To calculate the finite volume spectra, the variational method is employed, as detailed in Chapter 3. The operators used include quark bilinears of the form $\bar{\psi}\Gamma D...\psi$, where as discussed in Chapter 2, Γ represents a monomial of γ-matrices, D is a gauge-covariant derivative and the "..." indicates that up to 3 derivatives are used. Including derivatives allows for the construction of operators with higher angular momenta than can be obtained using only γ-matrices. The operator bases also include meson-meson-like operators of the form $\sum_{\vec{p_1}+\vec{p_2}=\vec{P}} \mathcal{C}(\vec{p_1}, \vec{p_2})\Omega^\dagger_{M_1}(\vec{p_1})\Omega^\dagger_{M_2}(\vec{p_2})$, where $\Omega^\dagger_{M_i}(\vec{p_i})$ interpolates meson M_i with lattice momenta $\vec{p_i}$. These operators are constructed for each momentum from eigenvectors v^n that were determined in variational analyses of π, K, η, D, D_s and $D^\star$ mesons [30, 60].

Several constructions representing a "single-meson" were used in each irrep, and the non-interacting energies were used to decide which "meson-meson"-like operators were used. The non-interacting energy of a meson-meson state is given by $E = \sqrt{m_1^2 + |p_1|^2} + \sqrt{m_2^2 + |p_2|^2}$, for mesons 1 and 2. All meson-meson operators expected to produce a level in the energy region below the $D\pi\pi$ threshold were used in this study. Extra operators that should only produce levels above $D\pi\pi$ threshold were also included, to ensure an accurate spectrum was obtained.

These operators were projected into the irreps of the cubic group O_h when at rest, and into the little group $LG(\vec{P})$ when at non-zero momentum $\vec{P}$. In this sector, mesons are not a eigenstates of charge conjugation, as discussed in Chapter 3. Thus states are labelled by their continuum J^P. The subduction of continuum J^P into relevant lattice irreps, and which partial waves of $D\pi$ and $D^*\pi$ these correspond to, are shown in Table 4.2.

$\vec{P}$	Irrep Λ	J^P ($\vec{P}=\vec{0}$) $\;\|\lambda\|^{(\tilde{\eta})}$ ($\vec{P}\neq\vec{0}$)	$D\pi\ ^{2S+1}\ell_J$	$D^*\pi\ ^{2S+1}\ell_J$
[000]	A_1^+	$0^+,\ 4^+$	$^1S_0$	...
	T_1^-	$1^-,\ 3^-$	$^1P_1$	...
	E^+	$2^+,\ 4^+$	$^1D_2$	...
[n00]	A_1	$0^{(+)},\ 1^{(-)},\ 2^{(+)},\ 4$	$^1S_0,\ ^1P_1,\ ^1D_2$	...
	E_2	$1,\ 2,\ 3$	$^1P_1,\ ^1D_2$	$^3S_1$
[nn0]	A_1	$0^{(+)},\ 1^{(-)},\ 2,\ 4$	$^1S_0,\ ^1P_1,\ ^1D_2$	...
	$B_2,\ B_2$	$1,\ 3$	$^1P_1,\ ^1D_2$	$^3S_1$
[nnn]	A_1	$0^{(+)},\ 1^{(-)},\ 2^{(+)},\ 3$	$^1S_0,\ ^1P_1,\ ^1D_2$	...

Table 4.2: The lowest $D\pi$ (and similarly $D\eta$ and $D_s\bar{K}$) and $D^*\pi$ continuum J^P and helicity λ that subduce in each of the irreps with $\tilde{\eta} = P(-1)^J$. $\vec{P}$ corresponds to the momentum with $n \in \mathbb{N}$, while ℓ represents the partial wave. Only the partial wave contributions listed are considered in the study.

Using this operator basis, principal correlators were computed in each irrep, and were fitted, as described in Chapter 3. For each irrep, a range of t_0 was considered. The correlators were compared across t_0 to ensure consistency, and a suitable choice of t_0 was made for each irrep. Shown in Figure 4.1 is the principal correlator fits of the first 4 states obtained in the $[110]A_1$ irrep are shown. $e^{E_n(t-t_0)}\lambda_n(t)$ is plotted against t/a_t, such that the correlators converge to 1. Darker points are included in the fits while the lighter points are not. In general a good signal is observed, that is stable with respect to variation of t_0 and with reasonable $\chi^2/N_{d.o.f}$.

Using the relevant states, dispersion relations were computed. Here the fitted anisotropy is not just a consistency test, it is quite important both in the conversion of our spectra to rest frame energy, E_{cm}, and in the scattering analysis performed. The anisotropy obtained from the pion dispersion relation is $\xi_\pi = 3.453(6)$ and from the D is $\xi_D = 3.443(7)$. $\xi = \xi_\pi$ was used to obtain scattering amplitudes but the systematic uncertainty takes both into account.
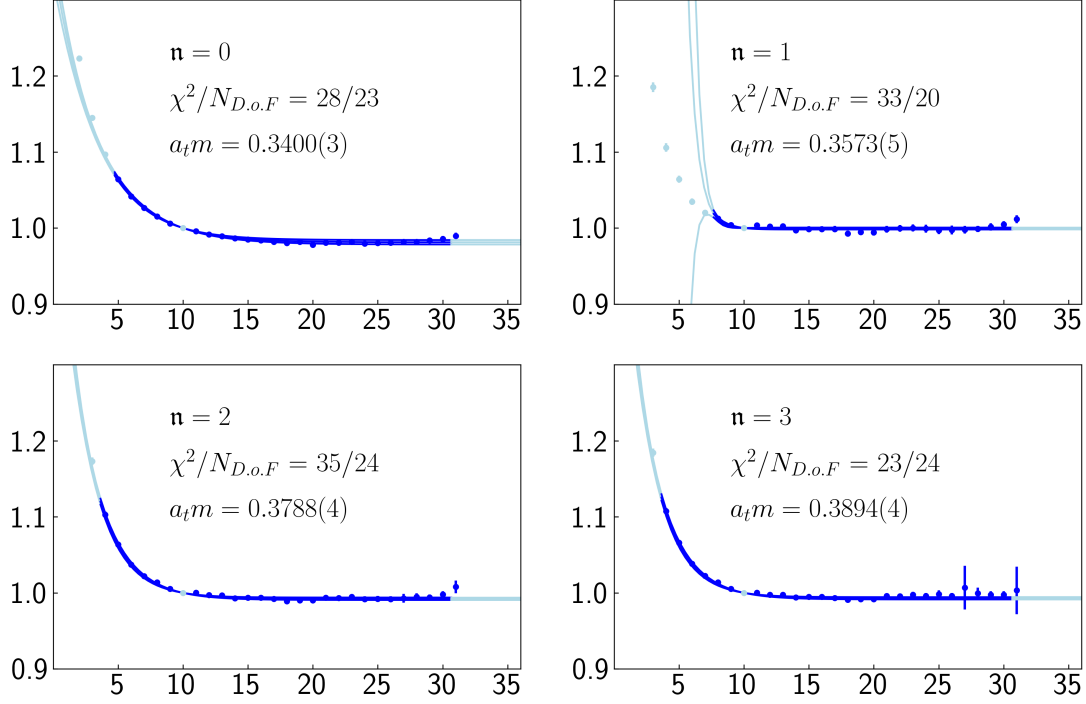
Figure 4.1: Principal correlator fits for the first 4 states, $\mathfrak{n} = 0, ..3$, in $[110]A_1$. Shown is $e^{E_n(t-t_0)}\lambda_n(t)$ plotted against t/a_t. Darker points are included in the fits while the lighter ones are not.

The finite volume spectra obtained from the principal correlator fits for the at-rest irreps is shown in Figure 4.2 and the spectra of the moving frame irreps is shown in Figure 4.3. Energy levels used in the scattering amplitude analyses are shown in black, while other energy levels obtained but not used are shown in grey. Various energy cutoffs were trialed before the $D\pi\pi$ threshold was chosen to be the cutoff for the rest of the analysis.

The $D\pi$ S-wave ($\ell = 0$) only subduces into $[000]A_1^+$ in the at-rest irreps. The $D\pi$ P-wave ($\ell = 1$) subduces into $[000]T_1^-$, while the lowest contribution for $[000]E^+$ is the $D\pi$ D-wave ($\ell = 2$), as summarised in Table 4.2. $[000]E^+$ will not be used in any of the fits as the effects of all partial waves with $\ell \geq 2$ were found to be negligible. The moving-frame irreps are shown in Figure 4.3. The $D\pi$ S-wave subduces into the top four of these, which are $[100]A_1$, $[110]A_1$, $[111]A_1$ and $[200]A_1$. The lower three, $[100]E_2$, $[110]B_1$ and $[110]B_2$ predominantly contain the $D\pi$ P-wave close to threshold and the $D^*\pi$ S-wave at slightly higher energies.
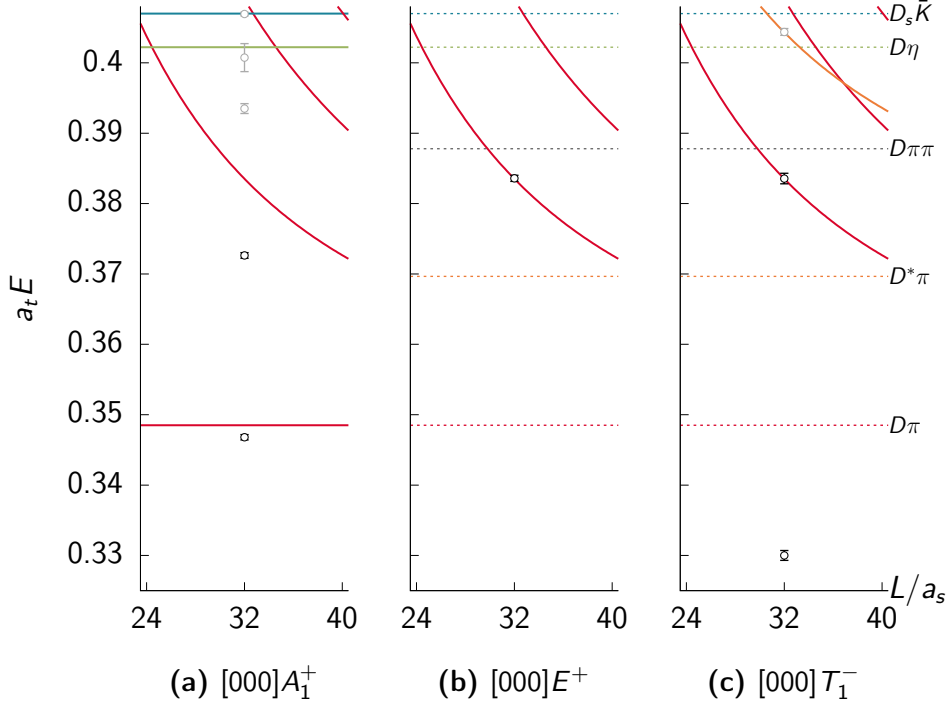
Figure 4.2: Finite-volume spectra obtained in the at-rest $[000]A_1^+$, $[000]E^+$ and $[000]T_1^-$ irreps. Dotted lines correspond to channel thresholds. Solid lines indicate non-interacting energy levels corresponding to operators included in the simulation. Points with error bars represent the energy levels obtained from the variational analysis. Black points will be included in the subsequent scattering analysis while grey points will be excluded.

All irreps that have an $\ell = 1$ contribution have a level far below threshold which may be associated with a deeply bound vector state. In all irreps with an $\ell = 0$ contribution a level around $D\pi$ threshold is present, that is shifted downward with respect to the nearby non-interacting level. A possible extra level also appears at around $a_t E_{cm} = 0.37$ and an upward shift of higher-up energy levels with respect to their non-interacting energies is observed. This indicates non-trivial S-wave interactions. In comparison, irreps having $\ell = 1$ as the lowest partial wave contribution show levels which are only marginally shifted away from the nearby non-interacting energies.
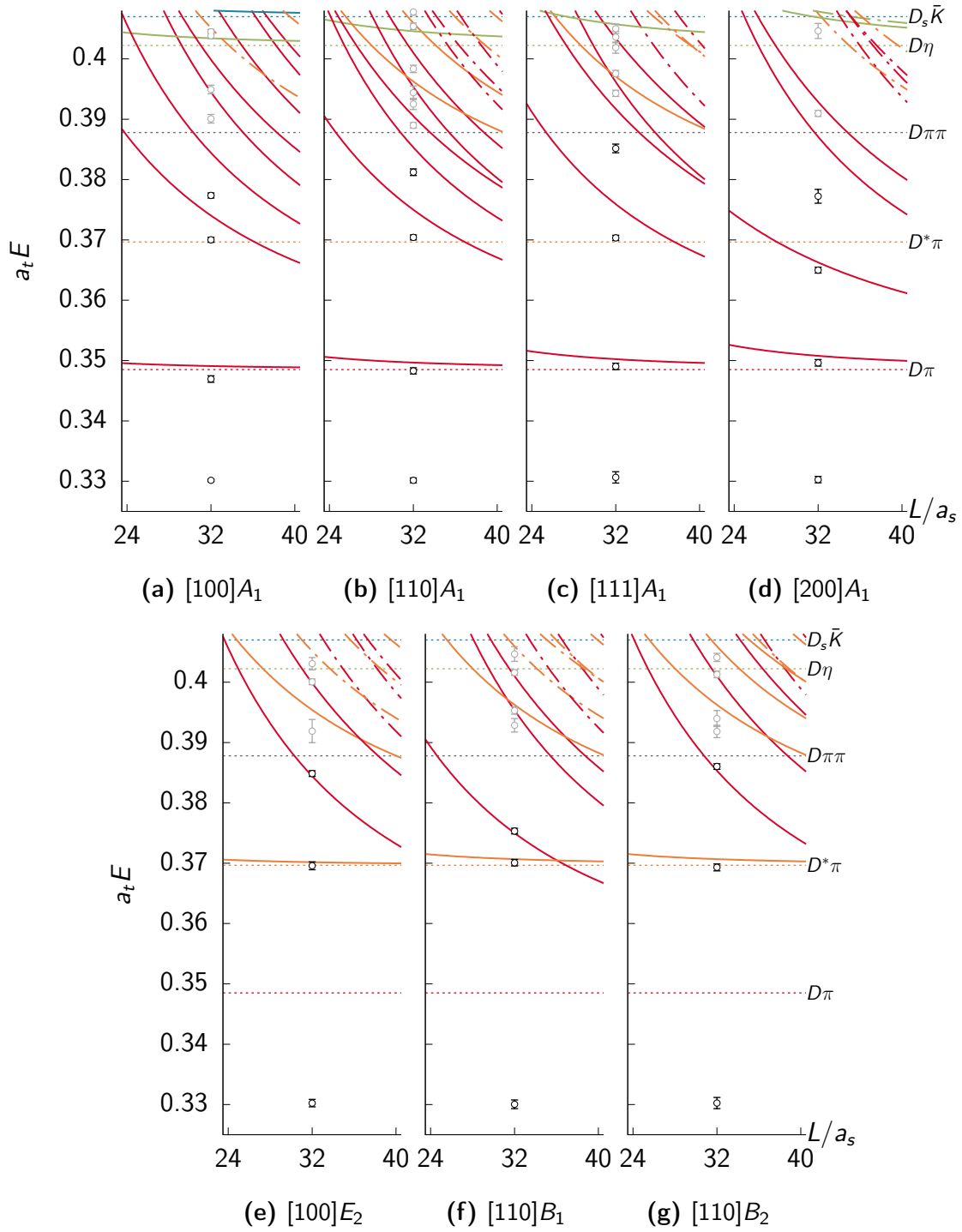
Figure 4.3: As in Figure 4.2, but for the moving-frame $[100]A_1$, $[110]A_1$, $[111]A_1$, $[200]A_1$ irreps (top) and $[100]E_2$, $[110]B_1$ and $[110]B_2$ irreps (bottom). The dash-dotted curves indicate an operator corresponding to a non-interacting level that was not included in the basis.

4.1.1 Operator Basis Variation

Figure 4.4 shows how the spectrum obtained for $[000]A_1^+$ varies when different operators are included in its basis. The grey blocks show the 1σ uncertainties of the energies obtained from the principal correlator fits. The histograms plotted next to each energy represent the components of the eigenvector, normalised to their maximum contribution seen in any state. The solid curves indicate the non-interacting energies. It is clear from the plot, that neither the $D\pi$-like or the $q\bar{q}$-like operators alone are enough to fully compute the spectrum up to the cutoff ($D\pi\pi$ threshold). Using only the $D\pi$-like operator gives three levels of the spectrum, whereas using only the $q\bar{q}$-like operator gives a single level. Clearly these two operators are necessary to get an accurate description of the spectrum up to the $D\pi$ threshold. Adding the $D\eta$-like and the $D_s\bar{K}$-like operators does not affect the spectrum below the $D\pi$ threshold, but more levels are found above it, specifically near the non-interacting levels for $D[000]\eta[000]$ and $D_s[000]\bar{K}[000]$.
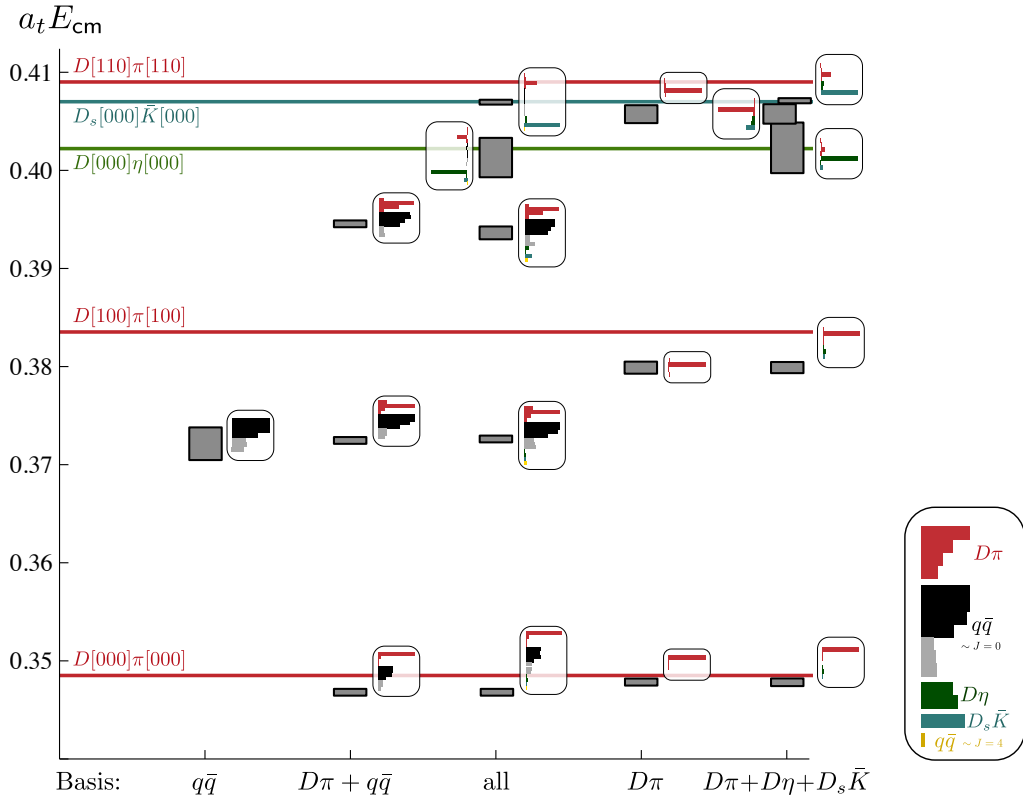
Figure 4.4: The spectra obtained in $[000]A_1^+$ when varying the operator basis. The operators included are marked below each column. The grey blocks show the 1σ uncertainties of the energies obtained from variational method. The histograms plotted next to each energy represent the operator overlaps, normalised to their maximum contribution seen in any state. The solid curves indicate the non-interacting energies. The lowest two energies from the column marked "all" corresponds to the levels used in the scattering analyses.

4.2   Scattering Analysis

The finite volume spectra calculated above are used to constrain the infinite volume scattering amplitudes through the Lüscher determinant condition as described in Chapter 3. The $D\pi$ S-wave contribution ($\ell = 0$) is the most interesting as non-trivial S-wave interactions are suspected from the finite volume spectra shown above. The $D\pi$ P-wave and the $D^*\pi$ S- wave contributions are also investigated.

At rest, the only irrep with S-wave contributions is $[000]A_1^+$. Below cutoff, there are only two states found in this irrep. Thus to constrain a scattering amplitude with more than two parameters, it is necessary to include moving-frame irreps, and therefore one must also consider P-wave contributions. For non-zero momentum, the A_1 irreps contain $J^P = 0^+, 1^-, 2^+$ $D\pi$ contributions, thus these partial waves must be considered. Across the moving-frame A_1 irreps, the lowest $D^*\pi$ contribution is P-wave, while the lowest non-interacting $D^*\pi$ level is in $[110]A_1$ and lies well above the $D\pi\pi$ threshold. Thus one scattering analysis will be of the $D\pi$ S- wave and P-wave, using the $[000]A_1^+$, $[000]T_1^-$ and moving frame A_1 irreps. For the other moving frames, namely $[100]E_2$ and $[110]B_1, B_2$, the leading partial wave is the $D\pi$ $P-wave$. However these irreps also include a $D^*\pi$ contribution with $J^P = 1^+$, and the lowest non-interacting level above $D\pi$ threshold is $D^*_{[100]}\pi_{[000]}$, meaning that $D^*\pi$ must be included in the t-matrix when using these irreps. Therefore a second scattering analysis is performed, using the $[000]T_1^-$, $[100]E_2$, and $[110]B_1, B_2$ irreps, to constrain the $D\pi$ P-wave, and assess the significance of the $D^*\pi$ S-wave. To show that contributions with $\ell \geq 2$ are negligible, the $[000]E^+$ irrep was considered, which has $D\pi$ D-wave ($\ell = 2$) as its lowest contribution. Only one state is found below the $D\pi\pi$ threshold. This state is found to be consistent with the lowest non-interacting level, $D[100]\pi[100]$, at $a_t E_{cm} = 0.38333 \pm 0.00049$. Using the Lüscher method, this is found to correspond to a D-wave phase shift of $\delta_2 = (0.49 \pm 1.29)^\circ$, which is consistent with zero. This allows the conclusion that the $D\pi$ D-wave contribution is negligible, and due to the k^{2l+1} suppression factor at threshold, this allows the same conclusion for higher ℓ contributions.

4.2.1 $D\pi$ with $J^P = 0^+$ and $J^P = 1^-$

The S and P-wave amplitudes were determined simultaneously using energy levels below $a_t E = a_t m_D + 2 a_t m_\pi$ from the $[000]A_1^+$, $[000]T_1^-$, and the four moving-frame A_1 irreps. As discussed in Chapter 3, a choice of parameterisation of the t-matrix is required. To avoid bias and explore the sensitivity of the amplitude, a range of parameterisation choices are fitted. First, a "reference" amplitude was fitted, which consisted of the form

$$K_0 = \frac{g^2}{m^2 - s} + \gamma,$$

$$K_1 = \frac{g_1^2}{m_1^2 - s}.$$

(4.1)

The S-wave is a K-matrix with a pole term and a constant γ, while a P-wave with just a pole term was chosen. Both have a Chew-Mandelstam phase subtracted at the pole parameter in each partial wave. The following parameters were obtained

$$
\begin{aligned}
m &= (0.401 \pm 0.010 \pm 0.007) \cdot a_t^{-1} \\
g &= (0.419 \pm 0.083 \pm 0.066) \cdot a_t^{-1} \\
\gamma &= (-2.0 \pm 1.3 \pm 0.9) \\
m_1 &= (0.33018 \pm 0.00016 \pm 0.00002) \cdot a_t^{-1} \\
g_1 &= (0.63 \pm 0.51 \pm 0.30)
\end{aligned}
\qquad
\begin{bmatrix}
1.00 & 0.93 & -0.62 & 0.23 & -0.10 \\
 & 1.00 & -0.85 & 0.17 & 0.05 \\
 & & 1.00 & -0.08 & -0.30 \\
 & & & 1.00 & -0.10 \\
 & & & & 1.00
\end{bmatrix}
$$

$$\chi^2 / N_{\text{dof}} = \frac{13.49}{20 - 5} = 0.90$$

(4.2)

where the parameters with a subscript "1" describe the P-wave, and those without describe the S-wave. The first uncertainty on each parameter is from the χ^2 minimum. The second uncertainty is obtained by performing many minimisations, after varying the π, D, and D^* masses and anisotropies. The masses were each varied to their maximum and minimum values within their 1σ uncertainties. The anisotropy was varied between $\xi_\pi + \delta\xi_\pi$ and $\xi_D - \delta\xi_D$. The maximum deviation obtained from the result obtained by these variations is the figure quoted as the second uncertainty. This is the procedure used for all minima that have multiple errors quoted. Other systematic errors due to the use of a single volume and single lattice spacing were beyond the scope of this study. The matrix beside the parameters is a measure of the correlation between free parameters in the χ^2 minimisation fit. It is a symmetric matrix with the lower triangular block not written. All results of t-matrix parameterisation fits will have a matrix of this kind presented.

The spectra obtained from this reference parameterisation are plotted in Figures 4.5 and 4.6, with the solutions of the Lüscher condition, Eq. 3.49. The levels below $a_t E \approx 0.39$ are in good agreement with the solutions of the Lüscher condition.

The phase shift of both the $D\pi$ S-wave and P-wave is plotted in Figure 4.7. The S-wave amplitude starts rising monotonically at threshold until the edge of the elastic region. This causes significant energy shifts in the finite volume.
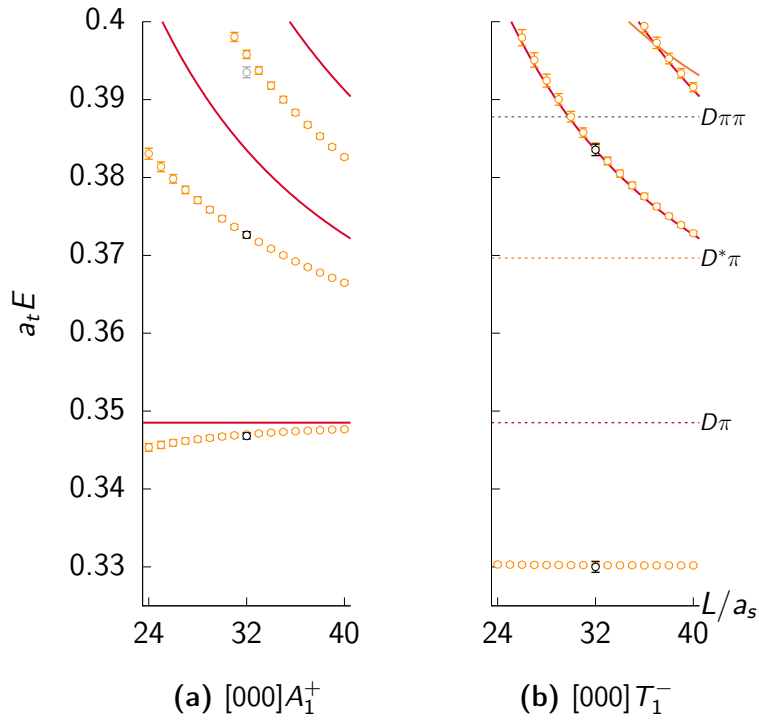
Figure 4.5: Finite-volume spectra obtained in the at-rest A_1^+ and T_1^- irreps, as in Fig. 4.2. This is plotted with the solutions of the Lüscher determinant condition using the reference parametrisation with the parameters resulting from the χ^2-minimisation, represented by orange points.
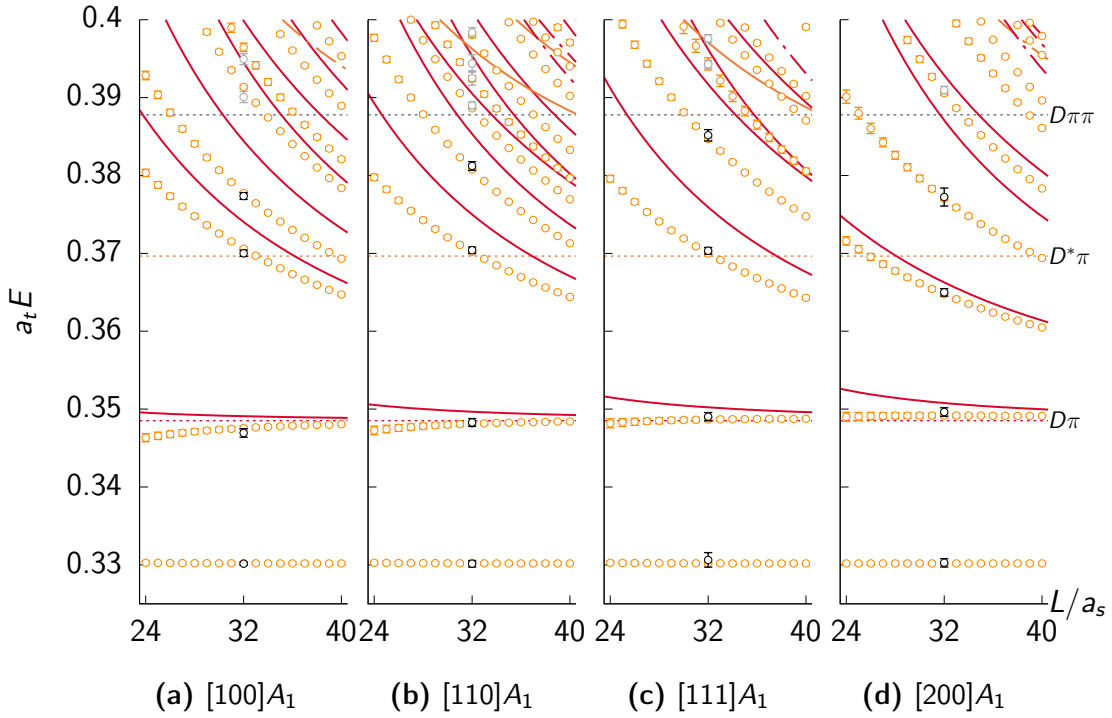
Figure 4.6: As Fig. 4.5, but for the moving frame A_1 irreps.

40
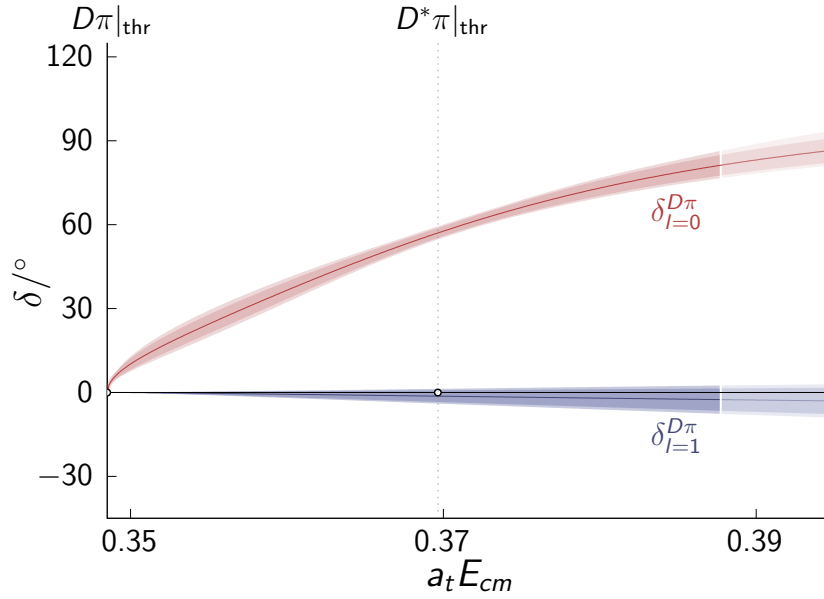
Figure 4.7: Phase shifts of the S-wave (red) and P-wave (blue) amplitudes. The inner line corresponds to the reference parameterisation. The inner dark error band represents the statistical error from the χ^2-minimisation while the outer light error band additionally includes uncertainties from varying the input hadron masses and anisotropy within 1σ.

A full list of parameterisations and values obtained can be found in the appendix, in Tables A1.3 and A1.4. The fits given in Table A1.3 exclude the deeply bound level which can be seen in the moving frame irreps and only a constant K-matrix in P-wave is used. The fits listed in Table A1.4 use the same spectra as used for the reference amplitude. In the region above threshold, all of the P-wave amplitudes produced phase shifts that are approximately zero. The amplitudes in Tables A1.3 and A1.4 are very similar at real energies. However, when continued to complex energies, there is a difference which will be discussed in the next section. But first, a selection of parameterisation variations will be further examined.

As discussed in Chapter 3, two common choices of parameterisation for single-channel elastic scattering are the effective range parametrisation and the relativistic Breit-Wigner. The Breit-Wigner fit gave the following parameter values

$$
\begin{aligned}
m_R &= (0.3913 \pm 0.0041 \pm 0.0014) \cdot a_t^{-1} \\
g_R &= (5.39 \pm 0.45 \pm 0.11) \\
m_1 &= (0.33014 \pm 0.00016 \pm 0.00003) \cdot a_t^{-1} \\
g_1 &= (0.3 \pm 1.3 \pm 0)
\end{aligned}
\qquad
\begin{bmatrix}
1.00 & 0.92 & 0.26 & -0.03 \\
 & 1.00 & 0.17 & -0.04 \\
 & & 1.00 & -0.01 \\
 & & & 1.00
\end{bmatrix}
$$

$$
\chi^2/N_{\text{dof}} = 14.63/(20 - 4) = 0.91 \tag{4.3}
$$

where the subscript "1" indicates the P-wave parameters, and the others are S-wave. The fit of the effective range parametrisation yielded

$$
\begin{aligned}
a_0 &= & (21.9 \pm 1.9 \pm 0.5) \cdot a_t \\
r_0 &= & (-22.1 \pm 4.3 \pm 1.6) \cdot a_t \\
m_1 &= & (0.33013 \pm 0.00016 \pm 0.00003) \cdot a_t^{-1} \\
g_1 &= & (0.2 \pm 1.1 \pm 0.5)
\end{aligned}
\qquad
\begin{bmatrix}
1.00 & 0.90 & 0.09 & -0.25 \\
 & 1.00 & 0.21 & -0.23 \\
 & & 1.00 & -0.08 \\
 & & & 1.00
\end{bmatrix}
$$

$$
\chi^2/N_{\text{dof}} = 14.81/(20 - 4) = 0.93 \; . \tag{4.4}
$$

It is worth mentioning that as well as the various t-matrix parameterisations discussed in Section 3.4.1, one other type was utilised in this study. The final type of parameterisation used is a unitarised chiral amplitude. A simple K-matrix form was used that can be written as

$$
K^{-1}(s) = \left(-\frac{1}{16\pi} \mathcal{V}_{J=0} \right)^{-1} + \frac{\alpha(\mu)}{\pi} + \frac{1}{\pi} \left(\frac{2m_2}{m_1 + m_2} \log \frac{m_2}{m_1} + \log \frac{m_1^2}{\mu^2} \right) \; . \tag{4.5}
$$

where

$$
\mathcal{V}_{J=0} = \frac{C_0}{8sF^2} \left(3s^2 - 2s(m_D^2 + m_\pi^2) - (m_D^2 - m_\pi^2)^2 \right) \tag{4.6}
$$

is the leading-order elastic $D\pi$ scattering amplitude projected onto the S-wave. F and $\alpha(\mu)$ are free parameters that are determined in the fit. The renormalisation scale μ must be fixed. For this study, this was fixed to $a_t \mu = 0.1645$ corresponding to $\mu \approx 1000\,\text{MeV}$. For the $u_{\chi PT}$ amplitude the parameters obtained were

$$
\begin{aligned}
F &= & (0.0191 \pm 0.0016 \pm 0.0002) \cdot a_t^{-1} \\
\alpha(\mu) &= & (-1.92 \pm 0.25 \pm 0.14) \\
m_1 &= & (0.33020 \pm 0.00016 \pm 0.00003) \cdot a_t^{-1} \\
g_1 &= & (0.76 \pm 0.39 \pm 0.11)
\end{aligned}
\qquad
\begin{bmatrix}
1.00 & -0.99 & -0.18 & 0.30 \\
 & 1.00 & 0.21 & -0.28 \\
 & & 1.00 & -0.12 \\
 & & & 1.00
\end{bmatrix}
$$

$$
\chi^2/N_{\text{dof}} = 13.78/(20 - 4) = 0.86 \; . \tag{4.7}
$$

4.2.2 $D\pi$ with $J^P = 1^-$ and $D^\star\pi$ with $J^P = 1^+$

A fit of the $D\pi$ P-wave and $D^\star\pi$ S-wave was also computed in this study. This fit used the $[000]T_1^-$, $[100]E_2$, $[110]B_1$ and $[110]B_2$ irreps. These irreps do not have a $D\pi$ S-wave contribution. However the moving frame irreps do contain a $D^*\pi$ S-wave

contribution ($J^P = 1^+$). A K-matrix parametrisation was used with a pole term in $\ell = 1$ $D\pi$ and a constant in $\ell = 0$ $D^*\pi$. The following parameters were obtained

$$
\begin{aligned}
\gamma^{D^*\pi} &= & (1.35 \pm 0.83 \pm 0.45) \\
g_1^{D\pi} &= & (0.72 \pm 0.31 \pm 0.13) \\
m_1 &= & (0.33028 \pm 0.00052 \pm 0.00005) \cdot a_t^{-1}
\end{aligned}
\qquad
\begin{bmatrix}
1.00 & -0.72 & -0.41 \\
 & 1.00 & 0.34 \\
 & & 1.00
\end{bmatrix}
$$

$$
\chi^2 / N_{\text{dof}} = \tfrac{8.59}{11-3} = 1.07 \,, \tag{4.8}
$$

with the uncertainties obtained as described previously for the $D\pi$ with $J^P = 0^+$ and $J^P = 1^-$ fits.

A phase shift for $D\pi$ P-wave and $D^*\pi$ S-wave was determined using the above parameterisation. A plot of these phase shifts is shown in Figure 4.8. The elastic $D\pi$ P-wave is small, but the parameters are non zero within uncertainties. The $D^*\pi$ contribution rises at threshold, perhaps indicating the tail of a higher D_1 resonance.
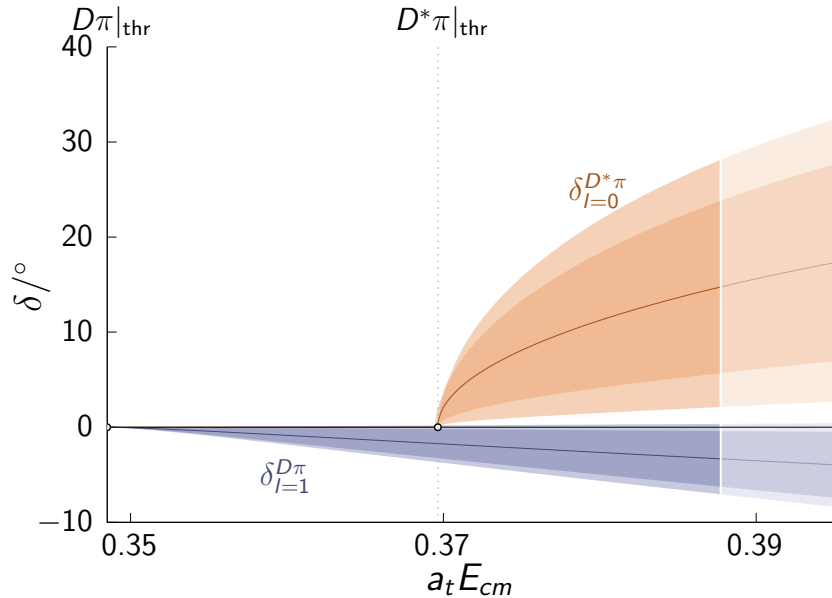
Figure 4.8: The phase shift for the $D\pi$ P-wave (blue) and $D^*\pi$ S-wave (orange) amplitude. The inner band corresponds to the statistical uncertainties from the χ^2-minimum in Eq. 4.8. The outer band shows the maximum possible deviation when varying the scattering particle masses and anisotropy within their uncertainties.

4.3   Pole Analysis

By analytically continuing amplitudes to complex $s = E_{cm}^2$, one can find differences between amplitudes that seem very similar at real energies. However, although they can differ, if a pole is present in the channel, it is often found in all parameterisations. This gives a way to compare the different parameterisations with each other and even with experiment.

The presence and position of poles allow for the determination of bound states and resonances in the amplitude. Near the pole, the t-matrix becomes dominated by a term of the form $\frac{r}{s_0 - s}$, where r is the residue of the pole and s_0 is the pole position. $c = \sqrt{r}$ is used as a measure of the coupling of the pole to the scattering channel.

The amplitudes used are analytic in s, except for cuts that appear due to the momentum $k(s)$ being a square root, and poles. The s-channel cut leads to a multi-sheeted complex s plane, where each contributing channel doubles the number of sheets. In this analysis we only consider a single channel, as $D\pi$ is the only relevant meson-meson threshold in $J^P = 0^+$. This leads to two Riemann sheets, known as the physical ($Im[k] > 0$) and unphysical ($Im[k] < 0$) sheets. Any complex pole on the physical sheet would violate causality and as such all complex poles only appear on the unphysical sheet. These correspond to resonances and appear as complex conjugate pairs. The complex energies at which resonances are found are given by, $\sqrt{s_0} = m - i\Gamma/2$ where m is the resonance mass and Γ is the width. Bound states correspond to poles on the physical sheet that appear below threshold on the real axis. Typically the further away a bound state is from threshold, the less effect it has on the amplitude above threshold. A bound state near threshold can significantly affect the behaviour just above threshold.

4.3.1   *S*-wave pole

The reference amplitude, Eq. 4.2, has an S-wave pole on the unphysical sheet at $a_t\sqrt{s_0} = (0.3592 \pm 0.0036) - \frac{i}{2}(0.0512 \pm 0.0095)$. A pole was found in all parameterisations, shown in Figure 4.9, where the notable parameterisations have been marked with black shapes.

Two clusters of poles were found for the S-wave, one with $a_t Im\sqrt{s_0} \approx -0.03$, and one slightly deeper in the complex plane with $a_t Im\sqrt{s_0} \approx -0.04$. Where the pole is found depends on the number of free parameters that are in the choice of S-wave paramaterisation. The nearer cluster corresponds to three-parameter S-wave amplitudes, and the deeper cluster arises from amplitudes with only two free parameters. Thus the

pole appears to shift upwards with extra free parameters. A four-parameter fit with a linear term $\gamma^{(1)}\hat{s}$ was also tried (amplitude (f)). It resulted in a slighter shift than observed going from two to three free parameters, with a pole found near the two clusters previously found. However the four parameter fit resulted in an amplitude with *two* poles, an additional one appearing around $a_t m \approx 0.29$, far below threshold. The χ^2/N_{dof} is higher for this parameterisation, possibly suggesting that there is too much freedom. Two, three and four-parameter S-wave fits are compared in Table 4.3.

amp	$a_t m$	$a_t g$	$\gamma^{(0)}$	$\gamma^{(1)}$	$\frac{\chi^2}{N_{\mathrm{dof}}}$	$\mathrm{Re}(a_t\sqrt{s_0})$	$-2\mathrm{Im}(a_t\sqrt{s_0})$	$a_t\lvert c\rvert$
(a)	0.3916(42)	0.313(22)	-	-	0.90	0.3590(80)	0.0797(83)	0.381(33)
ref.	0.4011(98)	0.419(83)	-2.0(13)	-	0.90	0.3592(35)	0.0512(95)	0.257(33)
(f)	0.4222(92)	0.789(57)	-8.6(16)	-14.7(87)	*0.94*	*0.3638(35)*	*0.0465(74)*	*0.218(27)*

Table 4.3: The result of varying the number of free parameters in the S-wave amplitude with a two-parameter P-wave as used in Eq. 4.2. "ref." indicates the reference amplitude, Eq. 4.2. The final amplitude (f) results in a parameterisation that produces two poles, one of them around $a_t m \approx 0.29$, far below threshold.
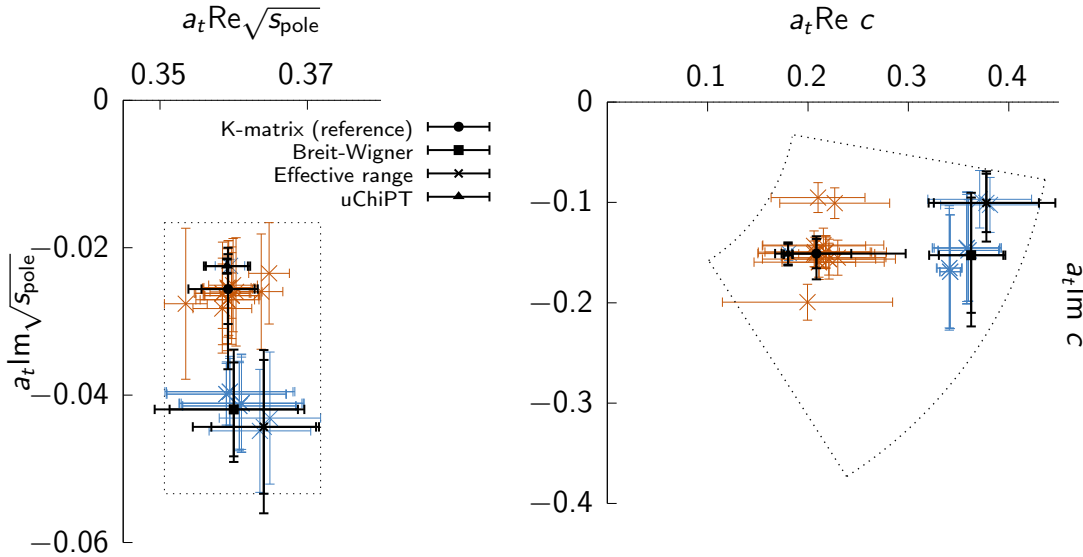
Figure 4.9: Poles on the complex energy plane (left) and couplings (right). The black filled circle corresponds to the reference amplitude. Other amplitudes discussed in the text are shown with different markers (see key). The coloured data points in both panels show the spread of poles (couplings) produced by the complete set of parameterisation variations (see tables A1.3 and A1.4). Orange crosshairs correspond to three-parameter S-wave amplitudes, blue crosshairs to two-parameter ones. The dotted rectangle encompasses the entire spread of the parameterisations including their statistical uncertainties but excluding variations of mass or anisotropy for amplitudes other than the reference parameterisation.

Looking at Figure 4.9, it is clear that only using one paramaterisation, or even one type of paramaterisation can not give a reliable estimate of the pole and its uncertainties. A final value that corresponds to the box around all the poles in Figure 4.9 is,

$$
\begin{aligned}
a_t \sqrt{s_0} &= (0.361 \pm 0.011) - \tfrac{i}{2}(0.070 \pm 0.037) \\
a_t c &= (0.32 \pm 0.13)\exp i\pi(-0.59 \pm 0.41)
\end{aligned}
\tag{4.9}
$$

In physical units fixed by the Ω baryon mass this corresponds to

$$
\begin{aligned}
\sqrt{s_0}/\text{MeV} &= (2196 \pm 64) - \tfrac{i}{2}(425 \pm 224) \\
c/\text{MeV} &= (1916 \pm 776)\exp i\pi(-0.59 \pm 0.41) \;.
\end{aligned}
\tag{4.10}
$$

No additional poles were found consistently in the S-wave.

4.3.2 P-wave pole

For all parameterisations that include a pole term for the P-wave and include the lowest $J^P = 1^-$ states, a very deeply-bound pole was found, with

$$
a_t \sqrt{s_0} = 0.3301 \pm 0.0012
\tag{4.11}
$$

which in physical units this corresponds to

$$
\sqrt{s_0} = 2006.9 \pm 7.4 \ /\text{MeV}.
\tag{4.12}
$$

While a coupling can be extracted for this pole, the uncertainties are very large. The $D\pi$ P-wave is largely unaffected by the presence of this pole, and can be approximated well by a constant K-matrix parameterisation. The mass found is consistent with the deeply bound state seen in irreps where $J^P = 1^-$ appears. The deeply bound finite-volume level can be found at a consistent energy when only $q\bar{q}$ operators are used, suggesting very little dependence on the $D\pi$ operators. If the pion mass was close to physical, this would become a shallow bound state due to the lowering of the $D\pi$ threshold, resembling the experimental D^*.

4.4 Outlook

To gain an understanding of the significance of the results presented above, it is useful to compare to the previous study of $D\pi$ scattering at the heavier pion mass of $m_\pi = 391$ MeV [2]. Context for this will then be provided by comparing the experimentally found D_0^* and D_{s0}^* to those found on the lattice, in this study and others.

4.4.1 Dependence on m_π

In Ref [2], $D\pi$ scattering was studied at a pion mass of $m_\pi = 391$ MeV, on three different volumes. In Figure 4.10, the reference scattering amplitude found at each pion mass is plotted in the left panel, with $m_\pi = 239$ MeV in red and $m_\pi = 391$ MeV in blue. The right panel shows the pole positions found for each study, with the error taking into account parameterisation variations, as well as the magnitude of the pole coupling to the $D\pi$ channel. For $m_\pi = 391$ MeV, a near-threshold bound state was found, with the amplitude turning on rapidly at threshold. With a resonance found for a closer to physical pion mass, this suggests that the dependence of the D_0^* on the pion mass is less than that of the $D\pi$ threshold.

It is also informative to examine the $k \cot \delta_0$ of each scattering amplitude, plotted against k^2. This is shown in Figure 4.11. Again, $m_\pi = 239$ MeV is plotted in red and $m_\pi = 391$ MeV in blue. For a bound state, the mass can be extracted at the intersection the amplitude and a $-|k|$ curve, as the mass of a bound state is given by $m_b = \sqrt{s_{thr} - |k|^2}$ for $|k|$ such that $k \cot \delta_0 = -|k|$. This is seen in Figure 4.11, as the blue curve corresponding to $m_\pi = 239$ MeV intersects the dotted $-|k|$ curve, while the red curve does not.

Interestingly, a similar phenomenon was found in a study of $\pi\pi$ scattering in Ref [61]. Here, a σ-like pole was found at the same masses, with a near-threshold bound state at the higher mass that evolves into a resonance pole at the lower mass. A very similar $k \cot \delta_0$ plot is produced in Figure 4 of Ref [61] to Figure 4.11 in this study.
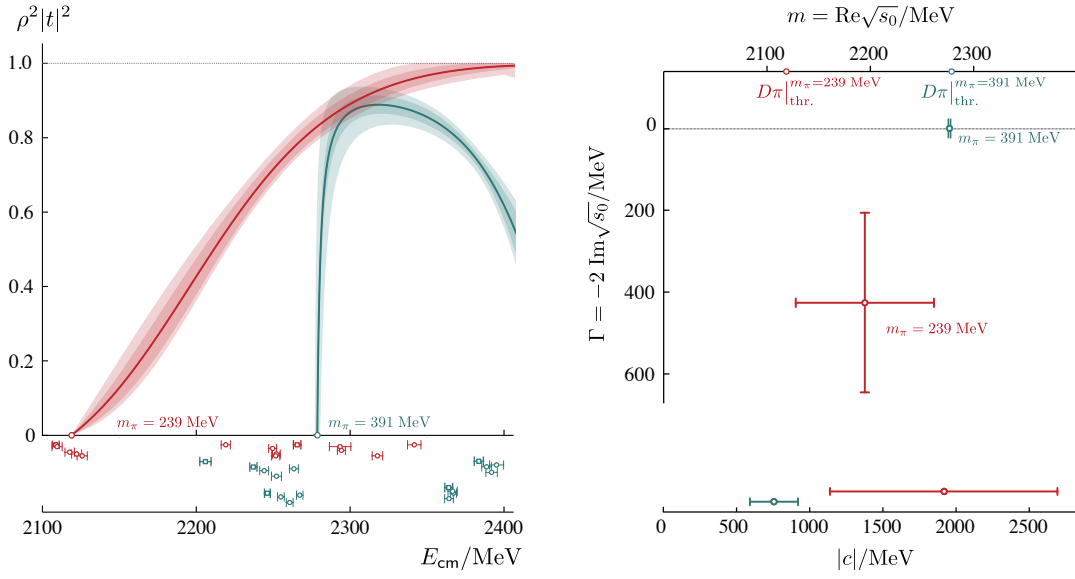
Figure 4.10: The left panel shows the reference scattering amplitude at $m_\pi = 239$ MeV (red) and 391 MeV (blue) plotted as $\rho^2 |t|^2$ with the energies that were used to constrain them shown below. The upper right panel shows the pole positions including the additional uncertainty found from the variation over parameterisation. The pole at the lower pion mass is a resonance found on the unphysical sheet, and at the higher pion mass is a bound state found on the physical sheet. The lower right panel shows the magnitudes of pole couplings to the $D\pi$ channel.
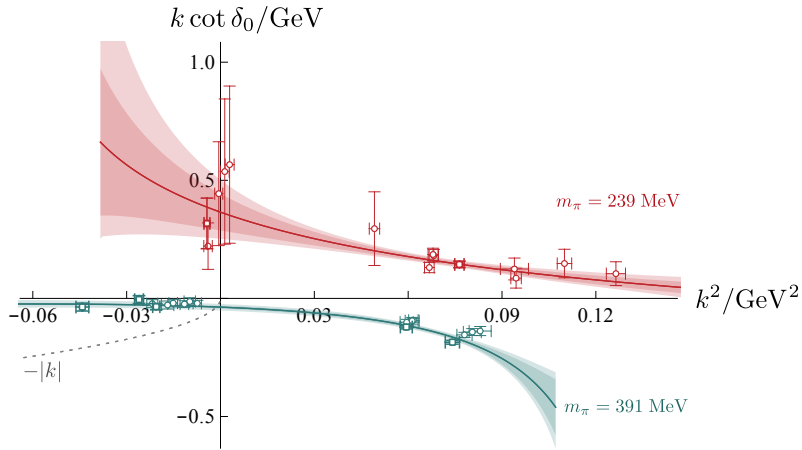
Figure 4.11: The scattering amplitudes at $m_\pi = 239$ and 391 MeV plotted as $k \cot \delta$ as a function of k^2. Red shows the $m_\pi = 239$ MeV amplitude and the $m_\pi = 391$ MeV amplitude is shown in blue. The points shown come from using the finite volume energies individually in the Lüscher determinant condition. The bound state mass at $m_\pi = 391$ MeV can be read off from the intersection of the blue curve with the dotted $-|k|$ curve at negative k^2.

4.4.2 The D_0^* in experiment

Experimentally, the D_0^* cannot be created in isolation. Because of this, it is typically studied as part of a decay chain. Various experiments have identified the D_0^* as an intermediary state of B meson decays. The first observation of the D_0^* was by Belle, in a Dalitz plot analysis of the $B^- \to D^+ \pi^- \pi^-$ decay [54]. The amplitude they fitted contained a Breit-Wigner parameterisation for the D_0^*. They found the mass of the D_0^* to be $m_{D_0^*} = 2308 \pm 17 \pm 15 \pm 28$ MeV. The same decay process was analysed by BaBar [55], who found $m_{D_0^*} = (2297 \pm 8 \pm 5 \pm 19)$ MeV. A more recent study that included the D_0^* was by LHCb of the $B^0 \to \bar{D}_0 \pi^+ \pi^-$ decay [56], using methods including partial waves up to $\ell = 4$, and using the K-matrix formalism to model $\pi^+\pi^-$. They found $m_{D_0^*} = (2354 \pm 7 \pm 11 \pm 2)$ MeV. The experimental average mass reported by the Particle Data Group (PDG) is $m_{D_0^*} = (2343 \pm 10)$ MeV with a width of $\Gamma_{D_0^*} = (229 \pm 16)$ MeV [7].

All of the studies above use a relativistic Breit-Wigner to model the D_0^* decay. Thus it is reasonable to compare these experimental results to the Breit-Wigner parameterisation used in this study. In the left pane of Figure 4.12, the Breit-Wigner parameterisation of the $D\pi$ scattering amplitude is plotted for both pion masses, with $m_\pi = 239$ MeV plotted in red and $m_\pi = 391$ MeV in blue. The table in the right pane of Figure 4.12 shows the parameters obtained from the fits for each of these parameterisations.

The shape of this amplitude is similar to that found in the referenced experiments above. The mass parameter of the Breit-Wigner parameterisation for the lighter pion mass of $m_\pi = 239$ MeV is 2380 ± 36 MeV, where the error includes both the systematic and

m_π / MeV	239	391
m_D / MeV	1880	1887
m_{BW} / MeV	2380(36)	2206(32)
g_{BW}	5.39(56)	7.62(75)
χ^2/N_{dof}	$\frac{14.6}{20-4}$	$\frac{36.0}{29-5}$
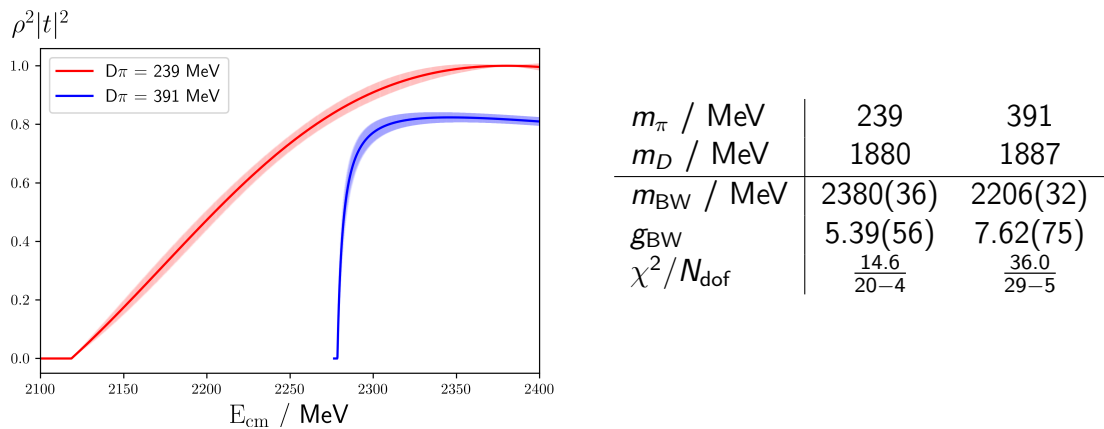
Figure 4.12: The plot on the left shows the Breit-Wigner parameterisations at both pion masses, with the lighter bands representing the statistical uncertainty. $m_\pi = 239$ MeV is plotted in red and $m_\pi = 391$ MeV in blue. The parameters obtained and the χ^2/N_{dof} for each are listed in the right table.

mass, anisotropy variations. This is within error of the quoted PDG value.

As mentioned at the start of this chapter, the D_0^* and D_{s0}^* were found experimentally to be of similar mass but with very different widths, the D_0^* being very broad compared to the narrow D_{s0}^*. In the lattice studies at two pion masses, described in this chapter, the D_0^* was consistently found at a mass below that of the D_{s0}^*, as expected from the quark model. This is apparent in Figure 4.13, which is a summary of the real parts of the pole positions for the D_0^* and D_{s0}^* at pion masses of $m_\pi = 239$ MeV and $m_\pi = 391$ MeV.

At $m_\pi = 391$ MeV, both states were found as bound states, but at $m_\pi = 239$ MeV, while the real part of the pole remains close to $D\pi$ threshold, the complex part is deeper in the complex plane. However, it is still found to preserve the expected mass ordering. Both studies of the D_0^* found its mass below the experimentally reported one. If one was to extrapolate to physical pion mass from the two points in Figure 4.13, then the current estimate of the D_0^* mass from experimental data would appear a little too high. However, given the large width it is possible that the experimental amplitudes are also compatible with a lower pole mass.
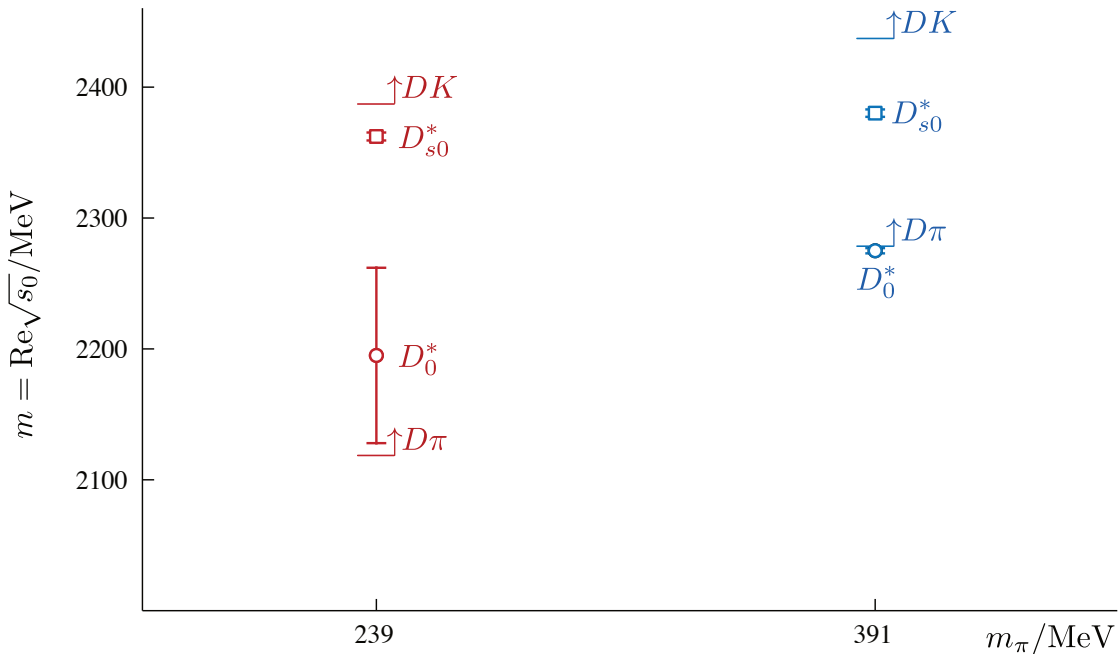
Figure 4.13: A summary of the real parts of the pole positions found in this analysis and Ref. [2] in S-wave $D\pi$ scattering, and Ref. [3] in S-wave DK scattering. The D_0^* resonance pole found in this study lies on the unphysical sheet with a large width. The other 3 poles are bound states.

5   Heavy–Light Meson Spectroscopy

In this chapter, the calculation of the excited and exotic spectra of the B, B_s and B_c mesons is described. Inspired by the success of studies in the charm-(light,strange,charm) meson sector spectra, detailed in Refs [4, 32], and of scattering calculations involving the D and D_s mesons, as described in Refs [1, 2], this study is a first-look at the spectra of bottom-(light,strange,charm) mesons. Relatively little has been observed experimentally in these meson sectors, with 4 low-lying states observed in the bottom-light and bottom-strange meson sector and only the $2S$, $1S$ states observed in bottom-charm. However, significant accelerator upgrades at the SuperKEKB accelerator means that the probing of bottom physics at Belle II, and the search for exotic bottom states, may soon improve the experiment knowledge of mesons containing bottom quarks [12]. LHCb has recently finished Upgrade I, and has plans to perform another improvement, Upgrade II in the 2030's [11]. It is currently performing Run III, which will include investigations into bottom-light, bottom-strange and bottom-charm states. This all motivates a lattice study into B, B_s and B_c meson spectra, attempting to predict states that may be found.

Various predictions of the B, B_s and B_c mesons have been made using the quark model [62–71]. From the perspective of lattice QCD, earlier work has studied bottom-(light, strange, charm) spectroscopy using static quarks with Heavy Quark Effective Theory in Refs [72–79], Non-Relativistic QCD in Refs [80–85], the Highly Improved Staggered Quark action in Refs [86, 87], and the Fermilab method, with the bottom quark treated as a valence quark in Ref [88], while Ref [89] did the same but included a scattering analysis of $B_s\pi^+$ using Luscher's method. B_s was studied using heavy meson chiral perturbation theory in Ref [90]. In a recent study of tetraquarks, positive parity B_s states were calculated using lattice NRQCD [91]. As in the previous studies of D, D_s, charmonium, and bottomonium, this study also investigated the presence of exotic states in the B, B_s and B_c spectra, specifically identifying the lightest hybrid supermultiplet in each of the sectors. The B_c hybrids have been studied previously using sum rules in Ref [92] and pNRQCD in Ref [93], while the B and B_s hybrids were studied using sum

rules in Ref [94].

In this study, 2+1 flavours of dynamical quarks were used on an anisotropic lattice where the temporal lattice spacing a_t is finer than the spatial lattice spacing a_s and the anisotropy $\xi = a_s/a_t \approx 3.44$. In the gauge sector a tree-level Symnazik-improved action is used, with larger-than physical light quark masses yielding a pion mass of ~ 391 MeV. Fermions are calculated with a tadpole-improved Sheikholeslami-Wohlert (Wilson clover) action including stout-smeared spatial links [20, 22], as discussed in Chapter 2. In the work presented in both this chapter and the next, the bottom quark is treated relativistically. It is calculated with the same tadpole-improved clover action as the other fermions in the calculations. The tuning of the bottom quark mass was done to recover the experimental η_b mass from the pseudoscalar dispersion relation. Details of this tuning can be found in Ref [95]. The anisotropy parameters determined in that tuning are used here, with two time-sources on a volume $(L/a_s)^3 \times T/a_t = 20^3 \times 128$ and with distillation for quark propagation.

5.1   Obtaining the spectra

To obtain the finite volume spectra of the B, B_s and B_c mesons, the variational method was employed, as discussed in Chapter 3. The operator basis for each lattice irrep consisted of single meson operators of the form $\bar{\psi}\Gamma\psi$, with Γ representing a monomial of gamma-matrices and forward-backward derivatives as discussed in Chapter 2. In addition, operators proportional to the field strength tensor were included, to allow for the investigation of hybrid mesons. The number of operators included in each lattice irrep is shown in the right side of Table 5.1, while the left side of this shows a breakdown of continuum spin into each lattice irrep. As described in Chapter 3, the energies of the spectrum are obtained through the variational method, by solving the GEVP and fitting

J	Λ
0	A_1
1	T_1
2	$T_2 \oplus E$
3	$T_1 \oplus T_2 \oplus A_2$
4	$A_1 \oplus T_1 \oplus T_2 \oplus E$

Λ	A_1	A_2	E	T_2	T_1
Λ^+	18	10	26	36	44
Λ^-	18	10	26	36	44

Table 5.1: The left table shows the distribution of continuum spin up to $J = 4$ into the irreducible representations of O_h, labelled Λ. The right table shows the number of operators used in each lattice irrep in this study. The operators are fermion bilinears of the form $\bar{\psi}\Gamma D_i D_j...\psi$ which are constructed using gamma matrices, Γ, and forward-backward derivatives, D_i, as described in text.

the principal correlators to exponentials. An example of such fits is shown in Figure 5.1. This shows the principal correlator fits of the first 11 states of the T_1^- irrep in the B_c sector. The value plotted is $e^{E_\mathfrak{n}(t-t_0)}\lambda(t)$ so that the curve tails off to 1. In general, a good signal was observed. It did not vary significantly against change of t_0 and the χ^2/N_{dof} obtained are reasonable. Similar quality was obtained for all other irreps in B, B_s and B_c.
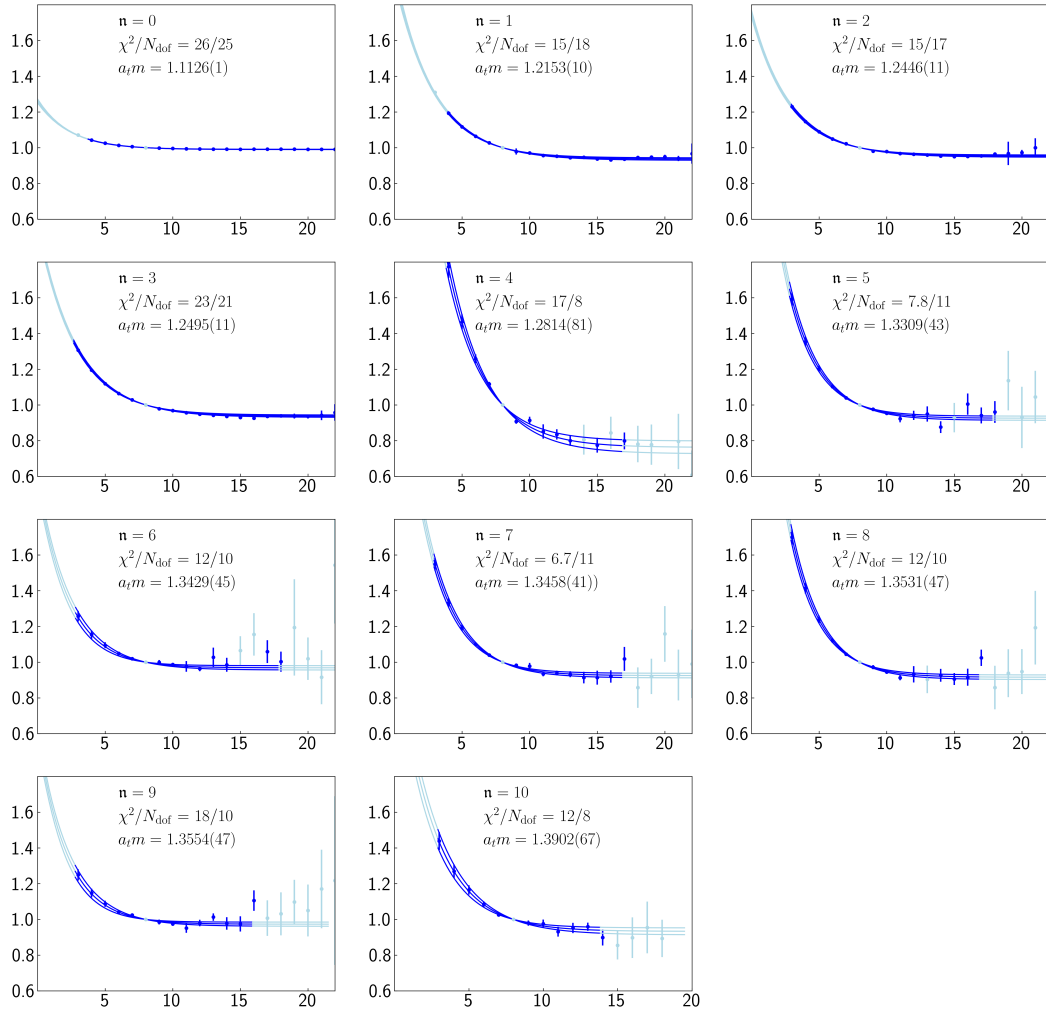
Figure 5.1: Principal correlator fits for the first 11 states, $\mathfrak{n} = 0, ..10$, in T_1^- in B_c. Shown is $e^{E_n(t-t_0)}\lambda_n(t)$ plotted against t/a_t. Darker points are included in the fits while the lighter ones are not.

The operator overlaps of the first 11 states in the T_1^- irrep in B_c is shown in 5.2. The overlaps are presented as histograms, and have been normalised such that the largest overlap corresponds to 1. The operators are color coded according to their continuum spin J, with black for $J = 0$, red for $J = 1$, green for $J = 2$, blue for $J = 3$ and gold for $J = 4$. Lighter shades in each colour represent hybrid-like operators of the corresponding continuum spin. As is evident from the plots, examining these operator

overlaps allows one to determine the continuum spin J of each lattice state calculated, as discussed in Chapter 3.
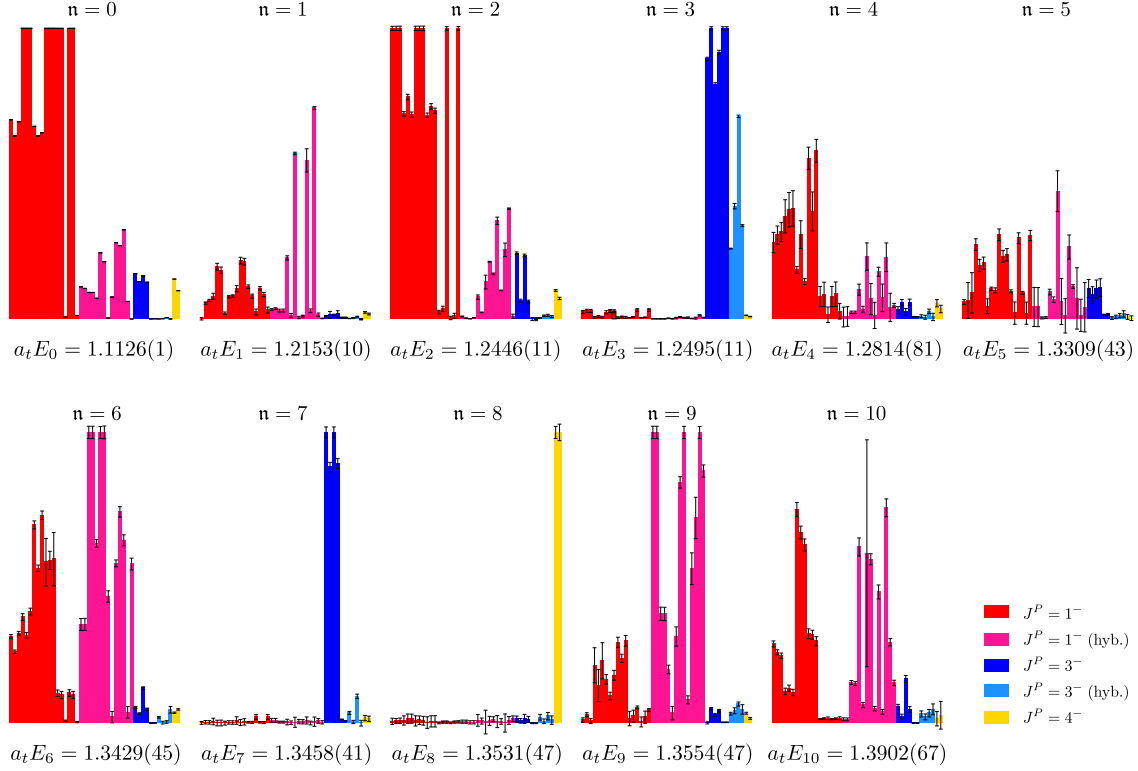
Figure 5.2: The normalised operator overlaps $|\tilde{Z}|$ of the first 11 states, $\mathfrak{n} = 0, ..10$, found in the T_1^- irrep of B_c sector. Operator overlaps are normalised relative to the largest operator overlap amongst the states shown. The operators are coloured according to their continuum spin, with lighter shades of colours representing hybrid-like operators. The energy in lattice units, $a_t E$, of each state is shown on the horizontal-axis.

5.1.1   Dispersion Relations

The relativistic anisotropic dispersion relation for a meson A can be written

$$(a_t E_A)^2 = (a_t m_A)^2 + \left(\frac{1}{\xi_A}\right)^2 (a_s p)^2, \tag{5.1}$$

where the lattice momenta are quantised so that $a_s \vec{p} = \frac{2\pi}{L}(n_x, n_y, n_z)$ for $n_i \in \mathbb{Z}$ and are labelled by $[n_x n_y n_z]$ by convention. From Eqn 5.1 the measured anisotropy for a given meson can be determined from the slope of its dispersion relation.

Using the relevant states, both the pseudoscalar and vector dispersion relations were computed for B, B_s and B_c, for a range of momenta up to [200]. The plots of these dispersion relations are shown below in Figure 5.3. The energies at each momentum were again determined from a large basis of interpolating operators using a variational analysis. These fitted energies are represented by points with errorbars contained in

the symbols. The dashed lines are the fits to Equation 5.1. The extracted anisotropies, compared with that extracted in bottomonium [95], is shown in Table 5.2. The obtained anisotropies were within $2 - 5\%$ of the target value, 3.444. These fits were repeated with states up to momentum [211], and similar results were obtained.
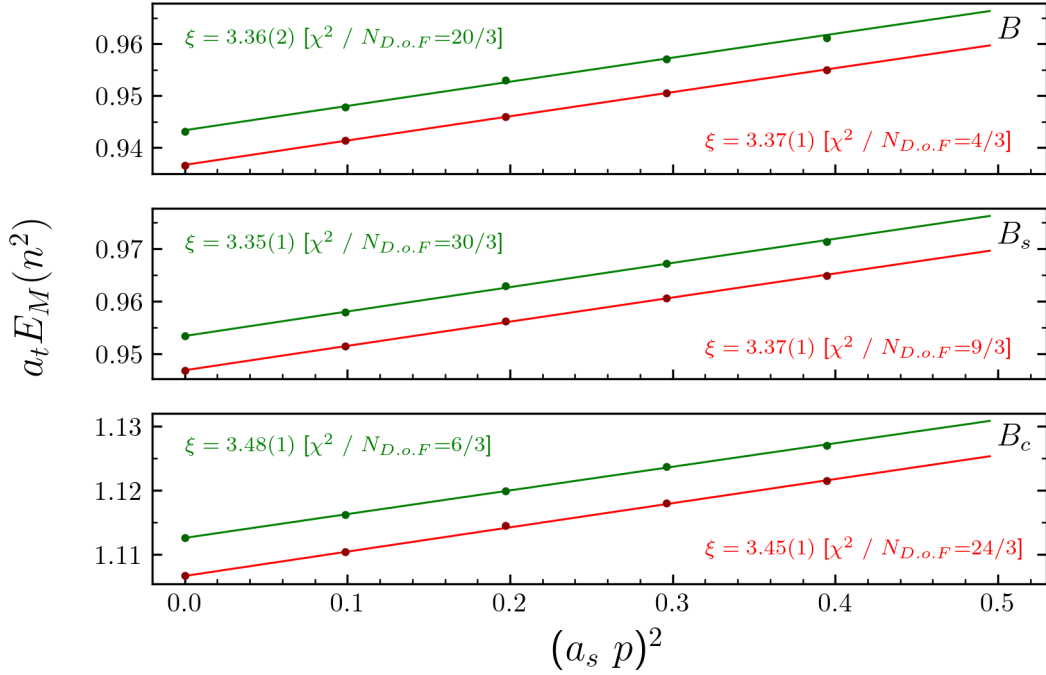
Figure 5.3: Pseudoscalar (shown in red) and vector (shown in green) dispersion relations for B, B_s and B_c using momenta up to [200]. States are represented by points with errorbars contained in the symbols. The solid lines are the best fits to Equation 5.1

.

	$a_t m$	ξ	χ^2/N_{dof}
B	0.93666(21)	3.365(14)	4/3
B^*	0.94335(24)	3.357(21)	20/3
B_s	0.94693(16)	3.371(11)	9/3
B_s^*	0.95329(19)	3.352(14)	30/3
B_c	1.10667(6)	3.447(5)	24/3
B_c^*	1.11260(8)	3.478(13)	6/3
η_b	*1.66302(5)*	*3.590(15)*	*0.81*
Υ	*1.66650(7)*	*3.574(26)*	*1.11*

Table 5.2: The mass and anisotropy determined from the intercept and slope respectively of dispersion relation fits for each of B, B_s and B_c. The bottomonium results from Ref [95] are shown in italics as comparison, as this is the sector the mass and valence anisotropy of the bottom quark was tuned in. All fits in this study were done using momenta up to and including [200]

It is worth noting that these dispersion relation fits have a rather large χ^2/N_{dof}. This arises from the small statistical errors in the determined energy levels inputted into the fit, and highlights the undetermined systematic errors in these calculations. The scale of the difference between the pion anisotropy and the anisotropies of the heavy-light meaons is small but is noteworthy. The difference is largest in bottom-light and bottom-strange mesons. The scale of this difference may give an idea of the discretisation effects present in the bottom meson sector.

5.1.2   Spin Identification

As discussed in Chapter 3, the operator overlaps are very useful in identifying the continuum spin of lattice states and especially when the same continuum state is subduced into multiple lattice states ($J \geq 2$). An example of this procedure is detailed here. In Figure 5.4, the overlaps of the continuum spin 4 operator $(a_1 \times D_{J_{13}=2,J=3})^{J=4}$ into four candidate continuum spin 4 states, in irreps A_1^-, T_1^-, T_2^- and E^-, in the B_c meson sector is shown. This operator was dominant in each of the four candidate states. As can be seen from the plot, the operator overlap is of a similar magnitude across all four states. The energy of each state is also consistent within errors. Thus it is concluded that these four states are part of the same continuum spin 4 state, and the average of their masses is taken to be the mass of the continuum state. This process was used to identify and calculate the mass of all states with continuum spin $J \geq 2$.

Figure 5.4: Operator overlaps for an operator with continuum $J^P = 4^-$ subduced into A_1^-, T_1^-, T_2^- and E^- states in B_c. For details on the operators used in this work and their naming convention, see Ref [29]. The energy and overlaps are consistent across the four irreps. These four lattice states are therefore identified as the same continuum 4^- state.

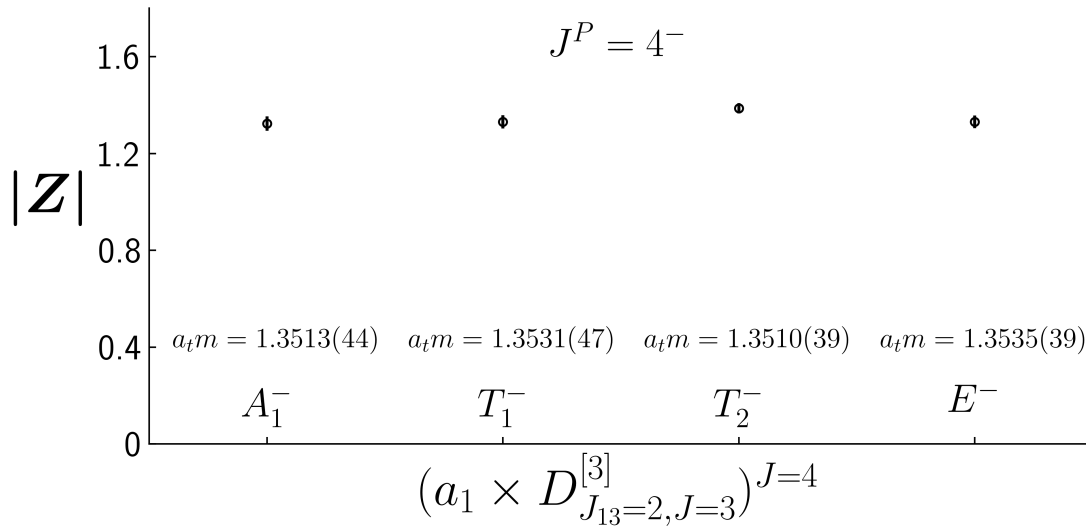## 5.2 Finite Volume Spectra by Lattice Irrep

The spectra of excited and exotic B, B_s and B_c mesons arranged by lattice irrep is shown in Figures 5.5 and 5.6. Results are presented as mass splittings, with half the mass of the η_B meson subtracted. This is done to mitigate uncertainties arising from the tuning of the bottom quark mass. The energy levels shown are coloured according to their continuum spin, with black for $J = 0$, red for $J = 1$, green for $J = 2$, blue for $J = 3$ and gold for $J = 4$, identified as described above. Lighter colors represent hybrid-like states with the corresponding continuum spin. The vertical height of the boxes represents the one sigma statistical uncertainty about the mean. The orange dashed lines show the lowest OZI (Okubo–Zweig–Iizuka) connected and OZI disconnected lattice thresholds determined in this work. An extensive spectrum of states, with both positive and negative parity, were determined in each meson sector. The pattern of states observed is similar across the three sectors. Similar patterns were also found in bottomonium [95], charmonium [4], and D and D_s [32].

5.2.1 Volume Dependence: a study of the B spectrum

To investigate the volume dependence of the heavy-light meson spectrum, the B spectrum was recalculated for lattices with volume $(L/a_s)^3 \times T/a_t = 16^3 \times 128$ and $24^3 \times 128$. A comparison of these spectra to the $20^3 \times 128$ spectrum, is plotted in Figure 5.7. The irreps plotted are those with states below the lattice $B_s\bar{K}$ threshold. The pattern of states observed is consistent across the 3 volumes. The lightest states in A_1^-, T_1^-, E^+ and T_2^+ are in agreement, but there is a slight shift observed in the lightest A_1^+ and T_1^+ states, corresponding to the lightest $J^P = 0^+, 1^+$ states. The error on the 24^3 A_1^+ state is too large to draw any meaningful conclusions but the lowest $J^P = 0^+$ state found on the 16^3 volume is $\approx 3\sigma$ away from the same state on the larger 20^3 volume. For $J^P = 1^+$, the lightest state found in the 24^3 volume is 2σ away from the lowest in the 20^3, as is the lightest 1^+ state found on the 16^3. This is very similar to what was found in the D meson sector [32], where finite volume effects were apparent in 0^+ and 1^+. A scattering analysis of the $D\pi$ channel offered clarity on the situation [1, 2], as mixing with two meson states was occurring. This was discussed in detail in Chapter 4. There is some shifting down of masses occurring in the $(L/a_s)^3 = (16)^3$ lattice for states above threshold, most significantly in A_1^+. This investigation highlights some interesting channels where near-threshold effects could be fruitfully studied. One of these is covered in the next chapter. The remaining sources of systematic error, namely the unphysical pion mass and finite lattice spacing, were not investigated in this work.
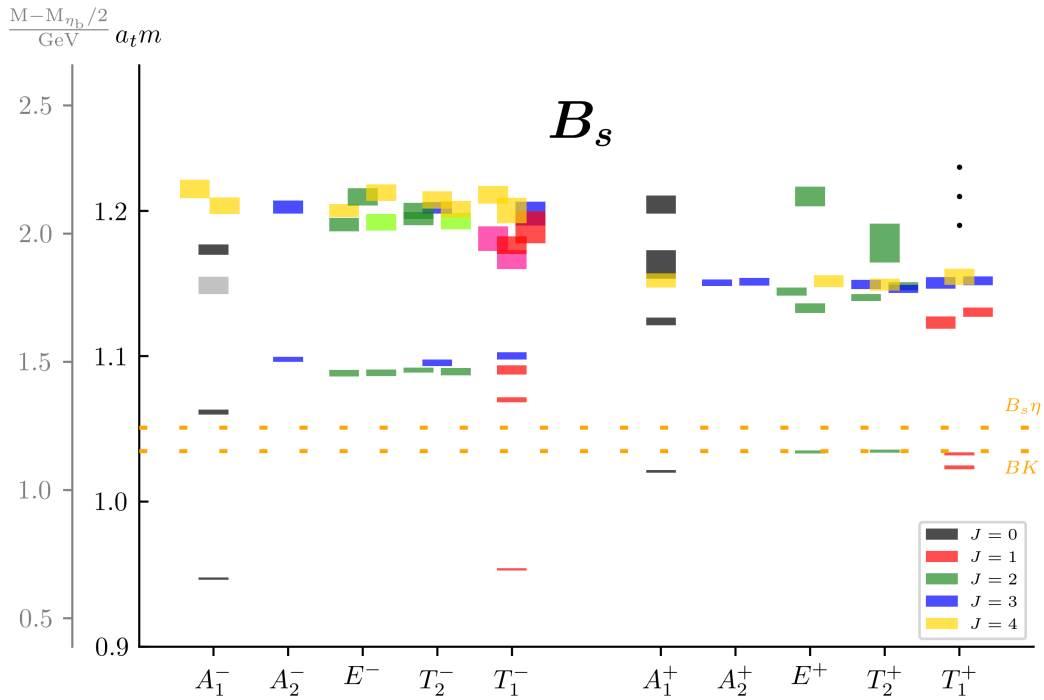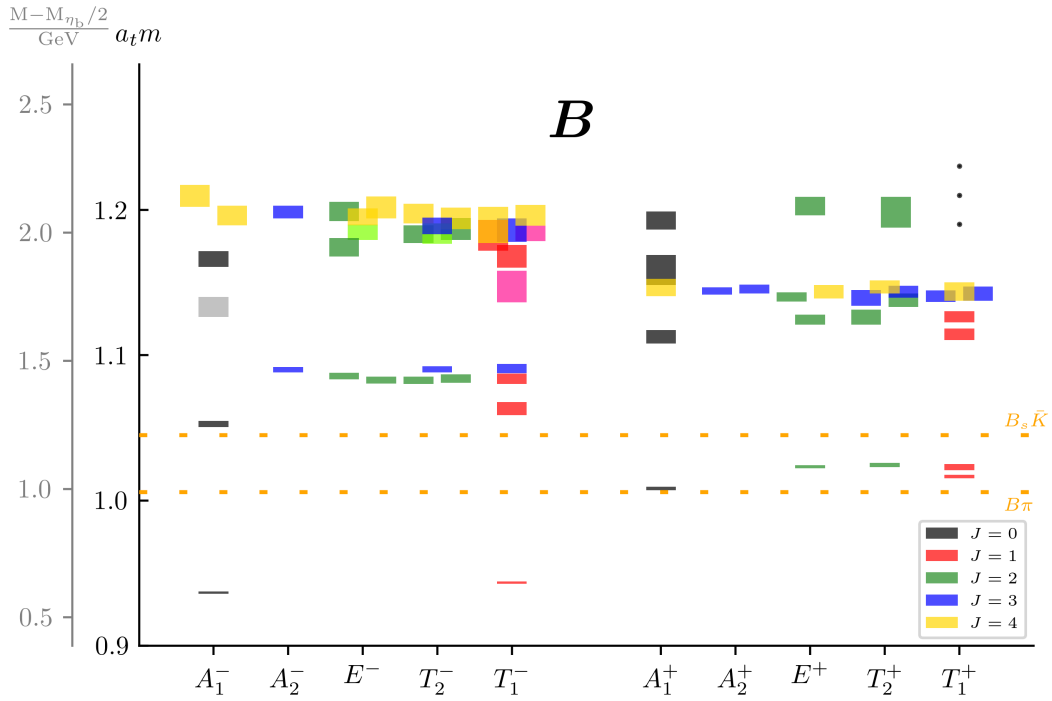
Figure 5.5: Spectra grouped by lattice irrep for B and B_s. States are colour coded according to their spin. The vertical height of the boxes represents the one sigma statistical uncertainty. The orange dashed lines represent lattice thresholds from this work. Ellipses indicate that more states may be present but were not robustly determined in this study.

58
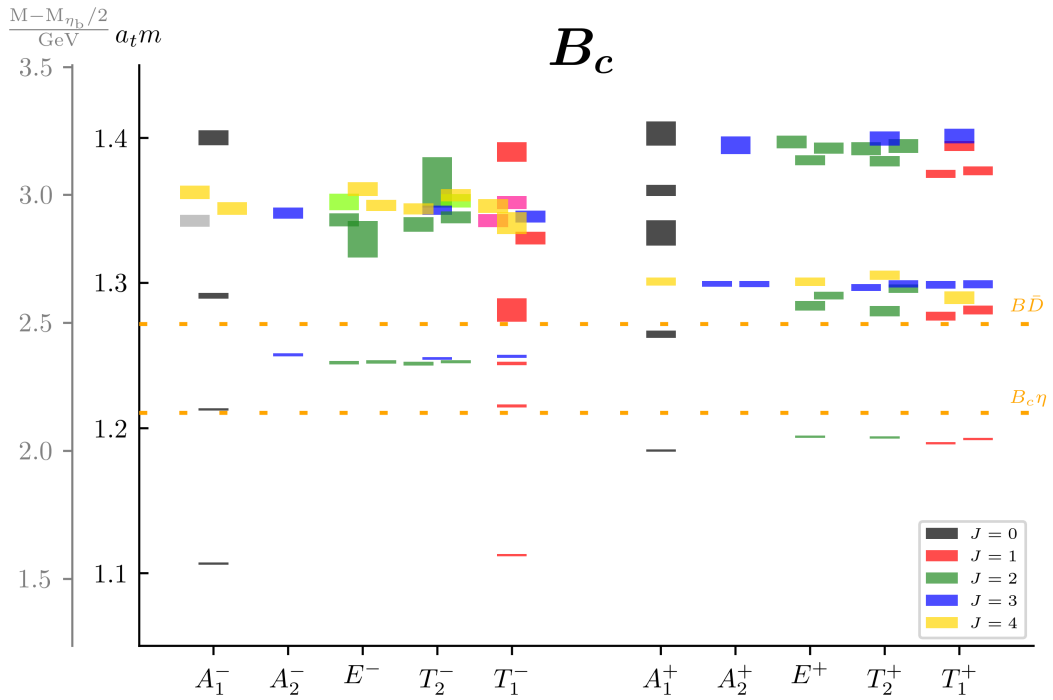
Figure 5.6: Same as Figure 5.5 but for B_c
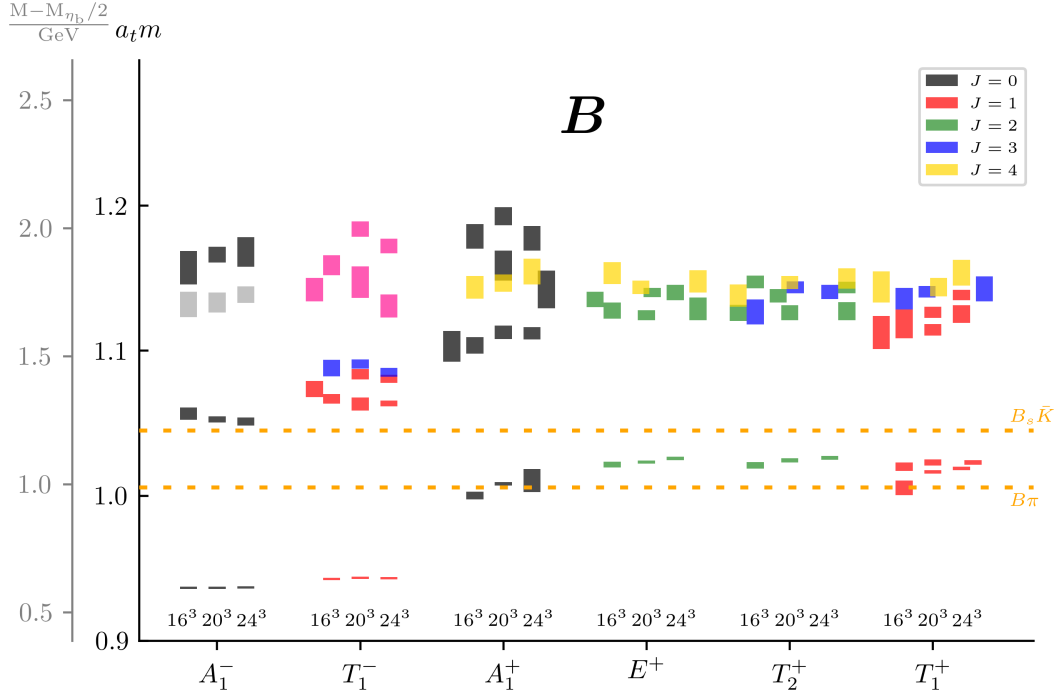
Figure 5.7: A comparison of a selection of irreps in the B meson spectrum across three different volumes. States are colour coded according to their spin. The vertical height of the boxes represents the one sigma statistical uncertainty. The orange dashed lines represent lattice thresholds from this work for the $(L/a_s)^3 = 20^3$.

5.3 Finite Volume Spectra by Continuum Spin

The spin-identified spectra labelled by continuum J^P is shown in Figures 5.9 and 5.8. To identify the different components for each state with spin $J = 2, 3, 4$ across the lattice irreps, the operator-state overlaps were used as described previously. The vertical height represents the one sigma statistical uncertainty about the mean. States in red are those calculated in this work which are dominated by operators with a hybrid construction. States in green are conventional states calculated in this work, while states in black are experimental states taken from the PDG [7]. Again, the thresholds shown are the lowest OZI connected and OZI disconnected thresholds in each of the meson sectors, with green showing the lattice thresholds from this work and black indicating experimental thresholds. Masses are presented with half the mass of the η_B meson subtracted. The pattern of states observed is similar to previous patterns seen in bottomonium [95], charmonium [4], and charmed mesons [32]. As in these previous studies, by using the same methods, an extensive spectrum of states was determined in each of B, B_s and
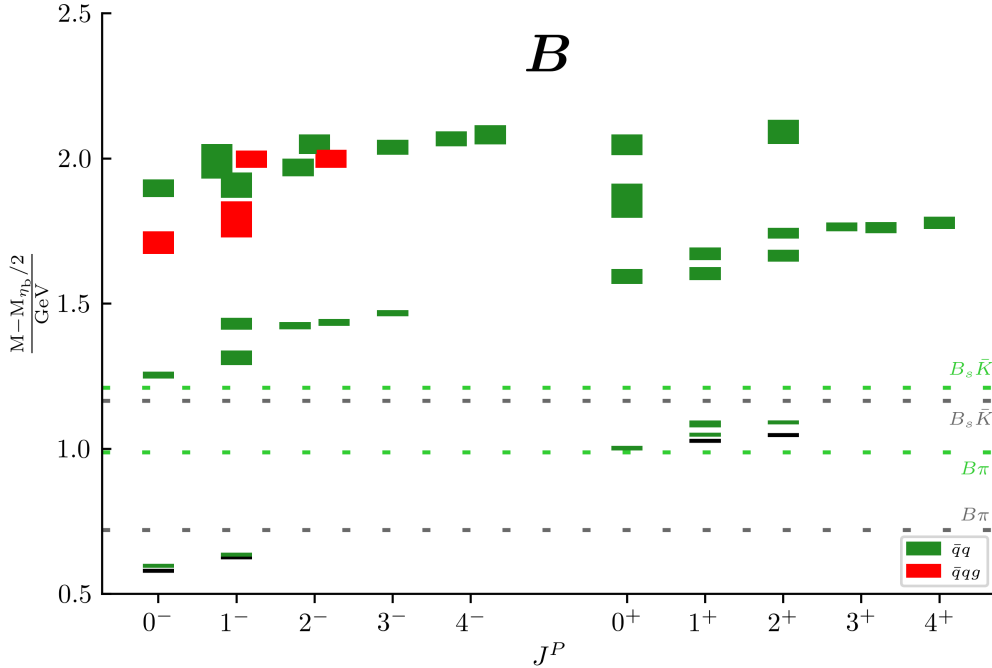
Figure 5.8: Spin-identified spectra labelled by continuum quantum numbers for B. States are labelled by J^P. The vertical height of the boxes represents the one sigma statistical uncertainty. States in red and green are those calculated in this study, while states in black are experimental. States in red are dominated by operators with a hybrid construction. Thresholds marked in green are from this work while black represents experimental thresholds. Ellipses indicate that more states may be present but were not robustly determined in this study.

B_c, with robust continuum spin identification and the ability to identify and differentiate which spin-multiplet nearby states belong to. Errors presented are statistical only. An assessment of the systematic errors, other than the finite size effects discussed previously, are beyond the scope of this study.
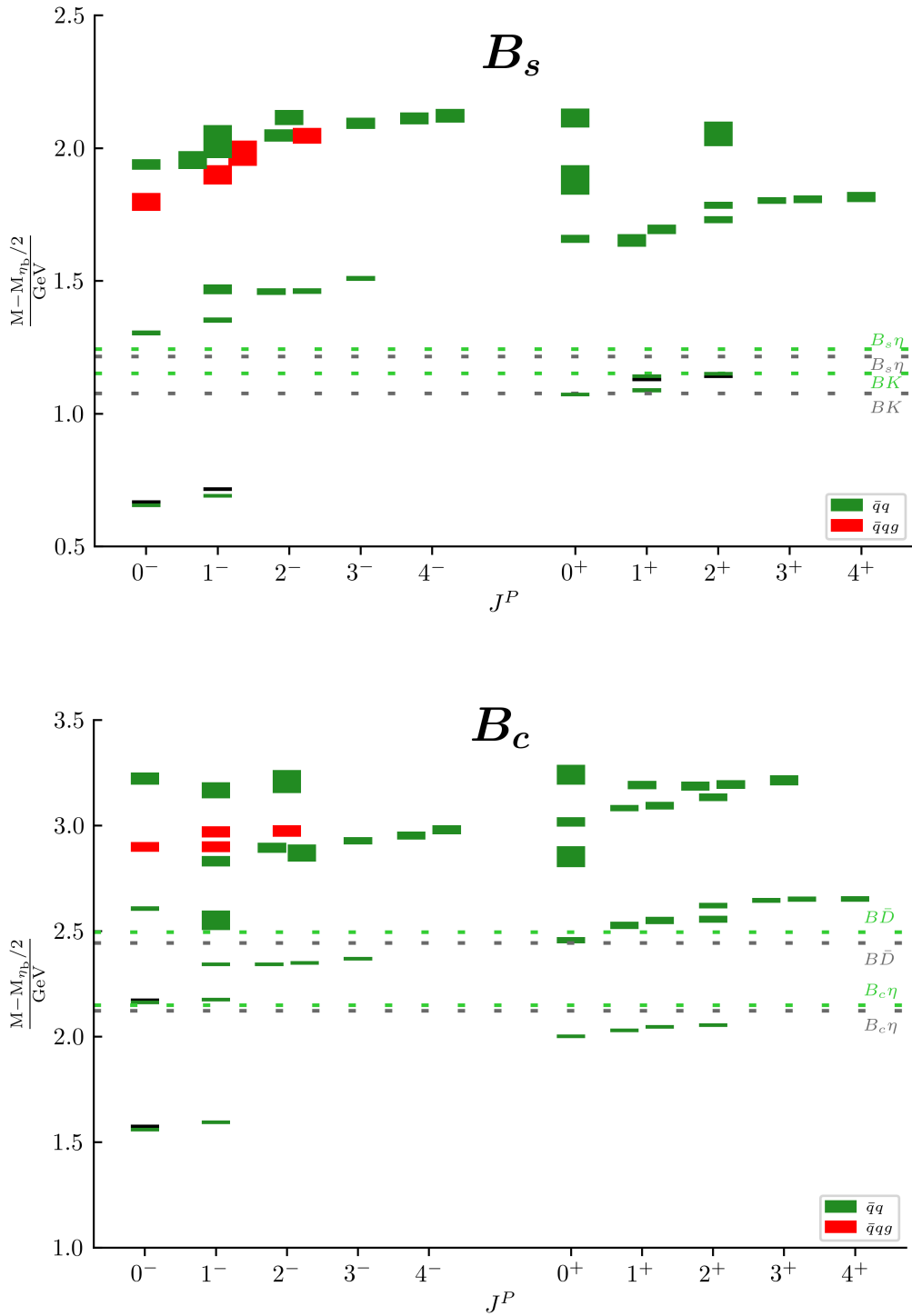
Figure 5.9: Same as Figure 5.8 but for B_s and B_c.

5.4   Outlook

To gain an understanding of the B, B_s and B_c spectra presented above, various aspects of the spectra will be examined, namely hybrid states and state mixing. The results above will also be compared to a selection of theoretical predictions, lattice calculations and experimental findings. This will give a broader view of the current state of bottom-(light, strange, charm) physics, and provide some context to the spectra shown above.

5.4.1   Hybrid States

As mentioned previously, operators proportional to the field strength tensor were included in the operator basis of each lattice irrep. This allows for the investigation into hybrid states in the bottom-(light,strange,charm) sectors. In Figures 5.5 and 5.6, the candidate hybrid states identified are marked by a lighter color than the other states of the same continuum spin J, and are found scattered across the lattice irreps. Perhaps more clearly, they are colored red in Figures 5.9 and 5.8. The continuum spin 2 state shown is the average of the candidates found in the T_2^- and E^- lattice irreps. The groups of four states in each meson sector, with continuum spin $J = (0, 1, 2)^-$, are proposed to be the lightest hybrid supermultiplet of B, B_s and B_c respectively.

The process for identifying this hybrid supermultiplet is very similar to how lattice states with the same continuum-spin are identified as the same continuum state, as was discussed in Chapter 3. By investigating the magnitude of the operator overlaps of hybrid-like operators in each of the candidate states, and comparing the values across the five irreps, it was found that they were of a similar value. The operator overlaps of the simplest hybrid-like operator in each of the candidate lattice states for each of the meson sectors is shown in the right-hand plots of Figure 5.10. These operators are the dominant operators in each of the candidate energy levels. The left-hand plots of Figure 5.10 shows a closer look at the continuum spins which were identified as containing hybrid candidates states. As is clear from these plots, the candidate states are of a similar mass and have similar overlap values for hybrid-like operators. These states are thus proposed to be a hybrid supermultiplet, the lightest one in each of the meson sectors.

The pattern of these candidate states, and the energy scale they were found at above the respective lightest state in each spectrum, is very similar to what was observed previously in bottomonium [95], charmonium [4], and D and D_s [32].
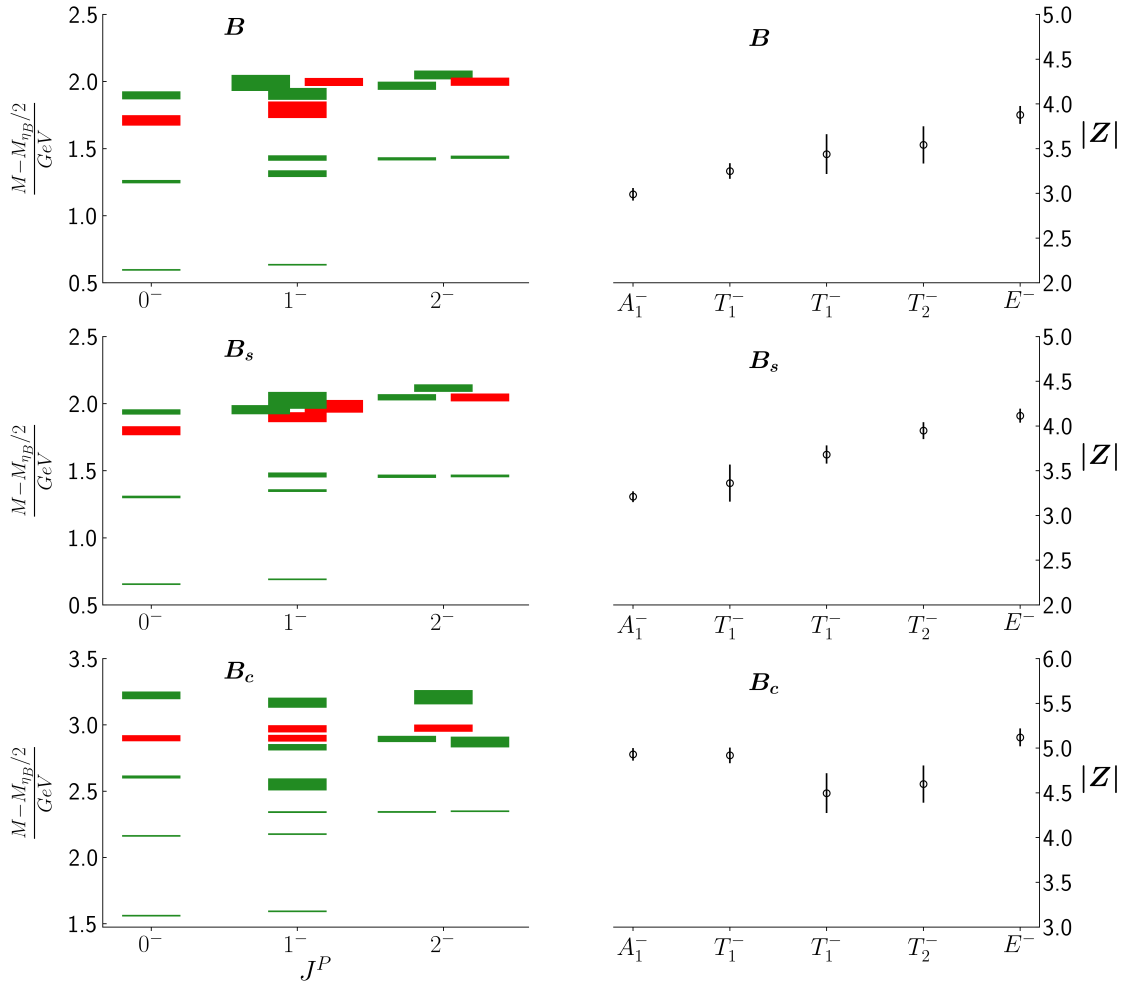
Figure 5.10: The left-sided plots show the continuum spins which were identified to contain hybrid candidates (0^-, 1^-,2^-) in each of B, B_s and B_c. Hybrid candidate states identified are shown in red. The right-hand plots show the overlaps of the simplest operator proportional to the field-strength tensor, $\left((\pi, \rho) \times D_{J=1}^{[2]}\right)^J$, for the candidate hybrid states in B, B_s, and B_c. As these are of a similar magnitude across each state, and each state is of a similar mass, these states are identified as a hybrid supermultiplet.

In Ref [93], quarkonium hybrids were calculated using effective field theory methods, including B_c hybrids. The B_c hybrid candidate states determined here are within 1σ of the hybrid mass proposed in that calculation, while they are at a slightly higher energy than those calculated using sum rules in Ref [92].

5.4.2 Comparing to Quark Model Predictions

Comparing to early quark model predictions of B, B_s, and B_c states [62], the predicted pattern of states and splittings between them is observed in the work above. The only difference of note is present in the B_c spectrum, where the splitting between the first $J^P = 3^-$ state and the first excited 0^- and 1^- states calculated in this study is larger than was predicted. A later study of the B_c in the relativistic quark model [63] solved this problem, and the results of this work have a very similar pattern of states to the predictions. This more recently predicted spectrum included higher energy states than the previous, and it is noteworthy that for states significantly above threshold, this study calculates them at a higher energy than predicted. This is also true in other quark model predictions that went to such energies, in B, B_s and B_c [64–69]. This is not very surprising as direct comparisons with quark models to a lattice study at finite lattice spacing with an unphysical pion mass will differ. Notably, the states identified as hybrid candidates above are not present in the quark model predicted spectra, which is to be expected, as exotic states are not contained in the quark model.

Comparing to much more recent predictions of B_c states [70, 71], which used a constituent non-relativistic quark model, a similar pattern of states predicted is present in the B_c spectrum presented previously in this chapter. In these newer predictions, two S-wave multiplets, two P-wave multiplets, and a D-wave multiplet are predicted to be below the BD threshold. However, while all of these multiplets are present in the B_c spectrum calculated above, the second P-wave multiplet, consisting of states with $J^P = (0^+, 1^+, 2^+)$, is found above BD threshold. This discrepancy may be resolved by the inclusion of *meson-meson* operators.

5.4.3 B, B_s and B_c in Experiment

As mentioned at the start of this chapter, not many states have been observed in the bottom-(light, strange, charm) meson sectors, particularly in the bottom-charm meson sector, where only B_c $(2S)$ and $(1S)$ have been observed. In the spectra plots grouped by continuum spin J above (Figures 5.9 and 5.8), the observed states are shown as black boxes, with the energy values having been obtained from the Particle Data Group (PDG) [7]. It is clear from these plots, that each of the currently observed experimental states have corresponding lattice states in the spectra computed earlier in this chapter. However, when comparing to experimental results, it is more appropriate to compare mass splittings rather than just the calculated energies of states. Doing this helps mitigate some discretisation effects from the tuning of the quark masses. Table 5.3 shows a selection of mass splittings obtained from the PDG and the corresponding

B / MeV	this work	PDG	B_s / MeV	this work	PDG
$B^* - B$	39.07 ± 1.59	45.21 ± 0.21	$B_s^* - B_s$	38.03 ± 0.83	$48.5^{+1.8}_{-1.5}$
$B_1 - B^*$	413.1 ± 6.1	401.4 ± 1.2	$B_{s2}^* - B$	553.72 ± 4.23	560.52 ± 0.14
$B_1 - B$	452.2 ± 6.1	446.7 ± 1.3			
$B_2^* - B$	494.1 ± 5.7	457.5 ± 0.7			
$B_2^* - B_1$	41.9 ± 8.2	13.4 ± 1.4			

B_c / MeV	this work	PDG
$B_c^* - B_c$	33.74 ± 0.28	
$B_c(2s) - B_c$	602.01 ± 3.40	597.73 ± 1.27
$B_c - B_s$	905.79 ± 0.71	$907.75 \pm 0.37 \pm 0.27$

Table 5.3: A selection of splittings in B(top left), B_s(top right) and B_c(bottom middle). This work refers to results obtained in this study, and PDG values were obtained from the Particle Data Group [7].

splittings from this work. All quoted values are in MeV.

The first thing to note is the S-wave hyperfine splittings, which are underestimated in this study. This underestimation arises due to the sensitivity of the hyperfine splitting to the light quark mass and discretisation effects. Part of this issue can also be attributed to the choice of the spatial clover coefficient in the quark field action. This study used the tree level tadpole improved value, but increasing this typically improves the value of the hyperfine splitting, as was investigated in charmonium [4] and bottomonium [95]. This would also improve the relative positions of the spin-singlet and spin-triplet states with $J^P = (0, 1, 2)^+$. Other splittings calculated are close to those measured experimentally, even though this was not the goal of this study.

5.4.4 The mixing of spin-singlet and spin-triplet states

As discussed in Chapter 3, charge is not a good quantum number in the heavy-light meson sector. As a result of this, states with $J = L$ ($^3L_{J+L}$ and $^1L_{J+L}$) can mix on the lattice. These correspond to spin-triplet and spin-singlet states respectively. For flavourless mesons, the states correspond to $J^{PC} = J^{\pm\pm}$ and $J^{\mp\pm}$ respectively.

One can attempt to quantify the level of mixing between a spin-singlet and spin-triplet state in the same lattice irrep through the calculation of mixing angles. To do this, one uses a two-state hypothesis, and assumes that energy independent mixing can occur (that the energy difference between the spin-singlet and spin-triplet states is negligible). This allows for the expansion of states A and B in terms of spin-singlet and spin-triplet basis states,

$$
\begin{aligned}
|A\rangle &= +\cos\theta \, |{}^1L_{J=L}\rangle + \sin\theta \, |{}^3L_{J+L}\rangle, \\
|B\rangle &= -\sin\theta \, |{}^1L_{J=L}\rangle + \cos\theta \, |{}^3L_{J+L}\rangle,
\end{aligned}
\tag{5.2}
$$

with the choice $m_B > m_A$. In the non-relativistic limit, certain operators only overlap onto spin-triplet and spin singlet states. These are given by $\left[(\rho - \rho_2) \times D_L^{[L]}\right]_{J=L}$, and $\left[\{\pi, \pi_2\} \times D_L^{[L]}\right]_{J=L}$ respectively. For 1^- hybrid, operators for spin-triplet and spin-singlet states are given by $\left[(\rho - \rho_2) \times D_1^{[2]}\right]_{J=1}$ and $\left[\{\pi, \pi_2\} \times D_1^{[2]}\right]_{J=1}$. Taking a ratio of the operator overlaps in states A and B allows for the determination of the mixing angle θ, with the ratio corresponding to either $\tan\theta$ or $\cot\theta$. The determined angle gives an estimate to the amount of mixing, with $\theta = 45°$ corresponding to maximal mixing, and $\theta = 0°$ or $90°$ corresponding to zero mixing (where the spin-triplet and spin-singlet states can be differentiated).

Tables 5.4 and 5.5 show the calculated mixing angles between the lightest pairs of P-wave (1^+), D-wave (2^-) and hybrid (1^-) states. Also shown in table 5.4, are the previously determined mixing angles in the study of the D and D_s mesons [4]. The heavy-quark limit for the mixing of the lightest pair of P-wave and D-wave states, as predicted in Ref [96] is also shown. The overall sign of the mixing angle is not observable in the calculation, so the absolute value is presented. Note the variation in the results based on choice of operator. This gives an insight into systematic uncertainties present in this calculation.

	Q-q	$\sim (\rho - \rho_2)$	$|\theta|/°$ $\sim \pi$	$\sim \pi_2$
1^+	c-s	60.9(0.6)	64.9(0.2)	66.4(0.4)
	c-l	60.1(0.4)	62.6(0.2)	65.4(0.2)
	b-s	59.3(0.6)	62.9(0.4)	63.5(0.4)
	b-l	58.7(0.6)	61.1(0.6)	62.0(0.6)
	H.Q.L.		54.7 or 35.3	
2^-	c-s	64.9(1.9)	68.7(2.0)	70.9(1.8)
	c-l	63.3(2.2)*	67.8(3.7)*	71.1(3.9)*
	b-s	55.6(1.1)	61.5(0.9)	62.2(0.9)
	b-l	52.4(0.5)	57.7(0.5)	58.7(0.5)
	H.Q.L.		50.8 or 39.2	
1^- (hybrid)	c-s	59.9(1.7)	67.9(0.9)	67.3(0.9)
	c-l	59.7(1.1)	68.4(0.8)	67.4(0.9)
	b-s	60.3(1.1)	61.6(1.2)	61.3(1.2)
	b-l	57.3(1.4)	65.1(1.1)	64.7(1.2)
	H.Q.L.		—	

Table 5.4: The absolute value of the mixing angles calculated for the lightest pairs of P-wave (1^+), D-wave (2^-) and hybrid (1^-) states in the b-l and b-s meson sectors, as well as c-l and c-s results calculated in Ref [4]. Angles extracted using different operators are presented. H.Q.L. stands for the heavy-quark limit, as predicted in Ref [96]. The results marked with * correspond to $(90 - |\theta|)$, as there was a difference in mass ordering in the previously calculated results in Ref [4].

	J^P		$|\theta|/^\circ$	
		$\sim (\rho - \rho_2)$	$\sim \pi$	$\sim \pi_2$
b-c	1^+	78.6(0.5)	79.1(0.5)	79.1(0.5)
	2^-	88.0(0.9)	89.4(0.4)	89.5(0.4)
	1^- (hybrid)	69.4(1.4)	71.3(1.2)	71.2(1.2)

Table 5.5: The absolute value of the mixing angles calculated for the lightest pairs of P-wave (1^+), D-wave (2^-) and hybrid (1^-) spin-singlet and spin-triplet states in the b-c meson sector. Angles extracted using different operators are presented.

The heavy-quark limit is the limit where the mass of the heavy quark Q in a meson $Q\bar{q}$, is taken to be much larger than the light quark q, $m_{c,b} \gg m_{u,d,s}$. In this limit, the heavy-quark spin decouples, and states appear in doublets j^P, where j is the total angular momentum of the light degrees of freedom. For more details, see Ref [4].

The results for the mixing angles in the b-l and b-s meson sectors is presented in Table 5.4. Similar mixing angles are found in the two meson sectors. This is not surprising, as in this study heavier than physical light quarks were used while the strange quarks used had near-physical mass, meaning that SU(3) flavour symmetry is not badly broken. Due to the unphysical light quark mass, one might expect the b-s meson results to be closer to physical value than the b-l. As can be seen, the values of $|\theta|$ for the P-wave and D-wave states are between the heavy-quark limit predictions, and the previously determined mixing angles for the c-l and c-s meson sectors, as was predicted to be the case in Ref [4]. A plot of the absolute values of the mixing angles for the lightest P-wave and D-wave spin-singlet and spin-triple state pairs, for each meson sector, ordered by relative quark mass difference, is plotted in Figure 5.11. This illustrates the trend towards the heavy-quark limit, but also highlights the systematic uncertainty introduced by the choice of operator.

Table 5.5 shows the absolute value of the mixing angles determined for the lightest pairs of P-wave (1^+), D-wave (2^-) and hybrid (1^-) states in B_c. As is evident from the table, these mixing angles are significantly larger than those determined for the heavy-(light,strange) meson sectors. These results are further away from the heavy-quark limit than the others. However, in this case, the separation of scale between the bottom and charm quarks may not be large enough for the heavy-quark limit to apply. Instead, bottom-charm mesons seem to be approaching the results of quarkonium, where charge is a good quantum number, meaning zero mixing occurs and the spin-singlet and spin-triplet states can be differentiated. The mixing angles calculated agree with this, being closer to zero mixing (which corresponds to 0∘ or 90°) than any of the other meson sectors, especially the D-wave ($J^P = 2^-$) spin-singlet and spin-triplet state mixing.
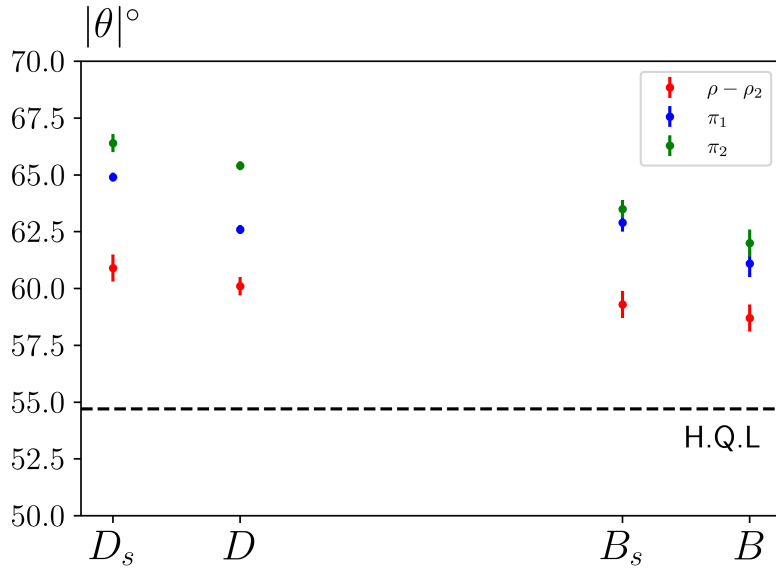
(a) *P*-wave
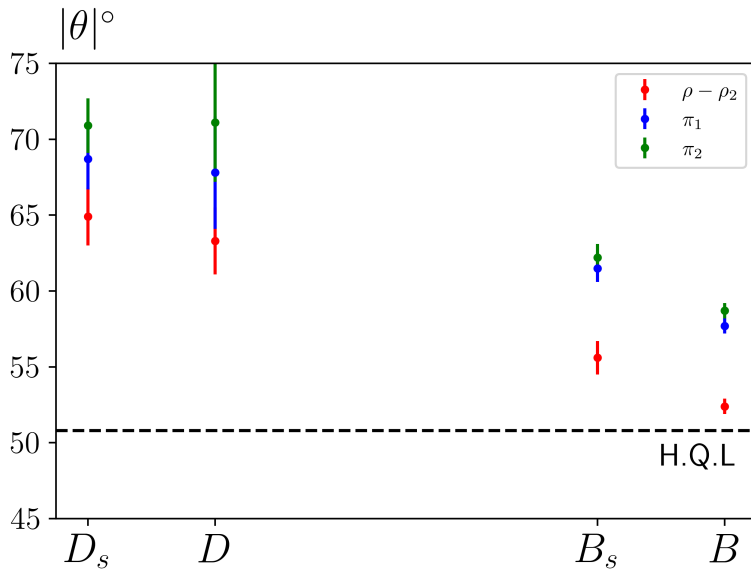
(b) *D*-wave

Figure 5.11: A plot of the absolute value of the mixing angles calculated for the lightest (a)*P*-wave and (b)*D*-wave spin-singlet and spin-triplet state pairs, for each meson sector, ordered by relative quark mass difference. Each choice of operator has been coloured differently with red for $\sim (\rho - \rho_2)$, blue for $\sim \pi$ and green for $\sim \pi_2$. The heavy-quark limits are marked as dashed lines

A plot of the absolute value of the mixing angles calculated for the lightest hybrid (1^-) spin-singlet and spin-triplet state pairs, for each meson sector, ordered by relative quark mass difference, is shown in Figure 5.12. This plot suggests that the mixing angle for the hybrid spin-singlet and spin-triplet states does not depend as strongly on constituent quark masses. The systematic uncertainties from the choice of operators are quite significant for some of the mesons, while mixing angles for the bottom-charm and bottom-strange have less difference between choice of operator used to determine the mixing angle.
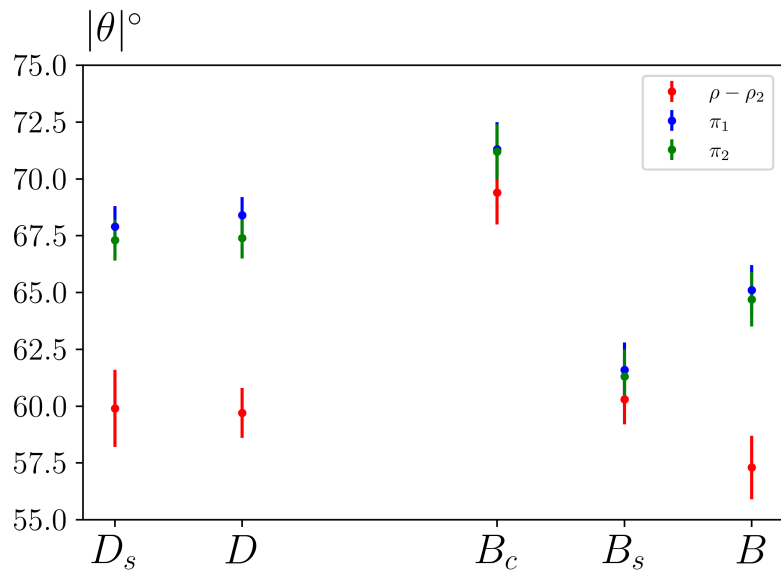
Figure 5.12: A plot of the absolute value of the mixing angles calculated for the lightest hybrid (1^-) spin-singlet and spin-triplet state pairs, for each meson sector, ordered by relative quark mass difference. Each choice of operator has been coloured differently with red for $\sim (\rho - \rho_2)$, blue for $\sim \pi$ and green for $\sim \pi_2$.

5.5   Next Steps

As mentioned in the previous sections, the pattern of states observed in B and B_s is very similar to that observed in the D and D_s mesons [32]. A particularly interesting set of states in B and B_s are the low-lying positive parity states that sit near $B\pi$ and BK thresholds respectively. A plot of the $\eta_b/2$ mass splittings of these states is shown in Figure 5.13, with experimental states and thresholds marked in black and those calculated in this study marked in green, as before.

The previous Chapter 4 discussed how a study of $D\pi$ scattering provided clarity on the shifts away from non-interacting levels observed in the D meson spectrum as well as the finite volume effects observed. Inspired by this, the next chapter describes an exploratory study of Isospin 3/2 $B\pi$ scattering, which examines how the scattering methods, detailed in Chapter 3, can be applied in the heavy-light sector.
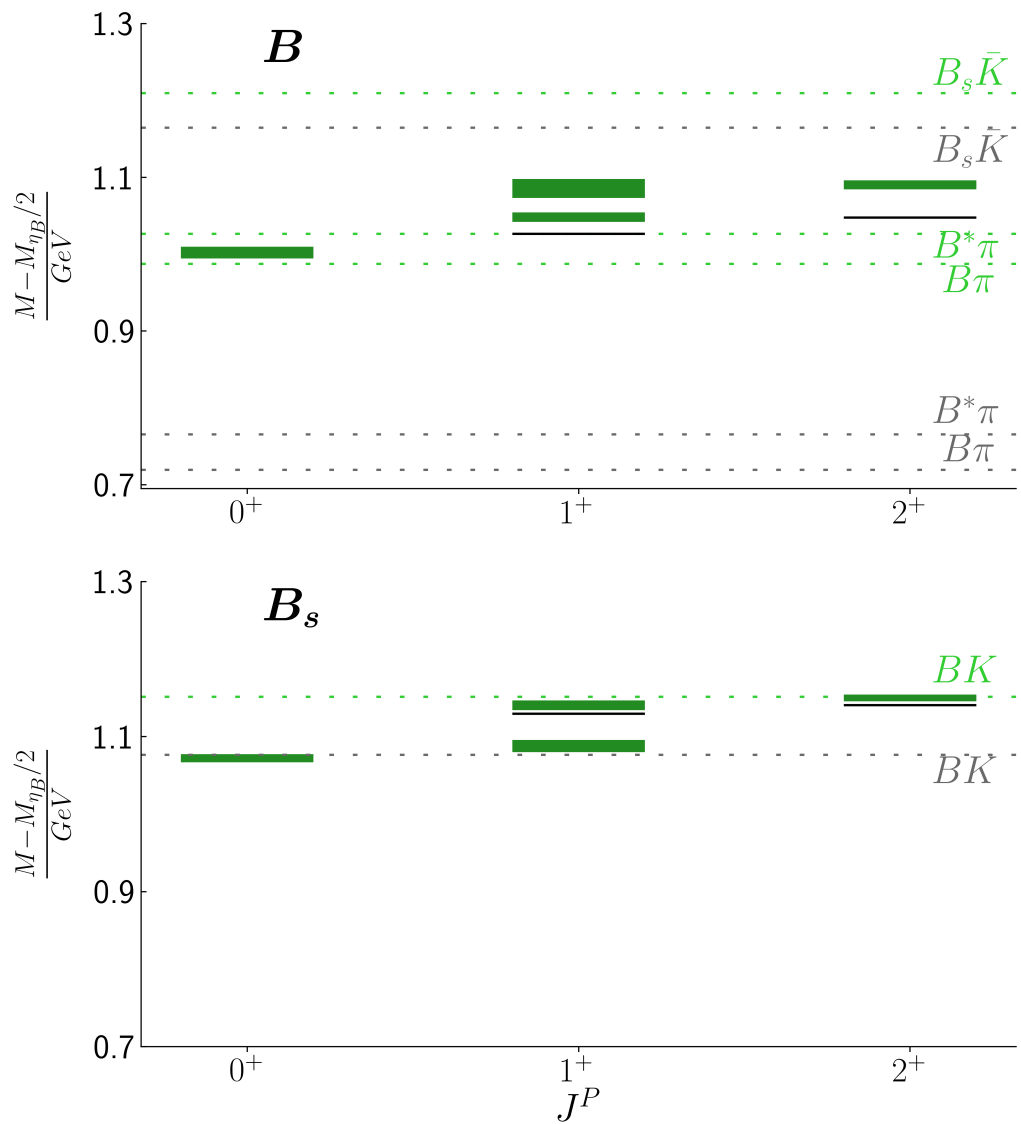
Figure 5.13: A zoom in of the low lying positive parity states in B and B_s. States and thresholds from this work are shown in green, while experimental states and thresholds are marked in black. These are of note due to the proximity to threshold of these states.

6   Isospin 3/2 $B\pi$ scattering

As mentioned in the previous chapter, significant accelerator development at the Su-perKEKB accelerator means that the probing of bottom physics at Belle II, and the search for exotic bottom states, may soon improve the experimental knowledge of mesons containing bottom quarks [12]. In particular, B meson spectroscopy and de-cays are to be investigated at Belle, as well as BB scattering. LHCb has also recently finished Upgrade I, and has plans to perform another improvement, Upgrade II in the 2030's [11]. It is currently performing Run III, which includes further investigation of B meson states and their decays. Motivated by this, a further lattice study of the B spectrum is performed. As discussed in Chapter 3, many of the excited states deter-mined through principal correlator fits are not actually stable, despite the assumption that they are. This is true for the spectra calculated in the previous chapter. Thus to further examine the B meson spectra, a scattering analysis must be performed.

In this chapter, the results of an exploratory investigation of isospin-3/2 $B\pi$ scattering will be presented. Following the calculation of the B spectrum in the last chapter, performing a scattering analysis is the next sensible step in investigating heavy-light mesons on the lattice. Based on the previous results, the positive parity near-threshold states are of particular interest. For this exploratory study, a scattering analysis of $B\pi$ was performed at isospin-3/2. The main difference between this study, and the isospin-1/2 $D\pi$ scattering study presented in Chapter 4, (besides the use of the B meson versus the D meson), is that at isospin-3/2, no single meson out-states are allowed, all out-states are meson-meson. Isospin-3/2 $D\pi$ scattering was investigated previously in [2]. Those results will be compared to the $B\pi$ results, in the outlook of this chapter.

This study was performed on three lattices, with volumes of $(L/a_s)^3 \times (T/a_t) = (16, 20, 24)^3 \times 128$. The details of each ensemble can be found in Table 6.1. In this study, 2+1 flavours of dynamical quarks were used on three anisotropic lattices where the temporal lattice spacing a_t is finer than the spatial lattice spacing a_s and the anisotropy $\xi = a_s/a_t \approx 3.44$. In the gauge sector a tree-level Symnazik-improved action is used, with larger-than physical light quark masses yielding a pion mass of ~ 391

$(L/a_s)^3 \times (T/a_t)$	N_{cfgs}	N_{tsrcs}	N_{vecs}
$16^3 \times 128$	479	4	64
$20^3 \times 128$	603	4	128
$24^3 \times 128$	553	2	160

Table 6.1: The gauge field ensembles used in this study. N_{cfgs} is the number of gauge field configurations used while N_{tsrcs} is the number of time sources used per configuration. N_{vecs} is the number of eigenvectors used in the distillation framework.

	$a_t m$		$a_t E_{\text{threshold}}$
π	0.06906(13)	$B\pi$	1.00572(24)
B	0.93666(21)	$B^*\pi\pi$	1.08147(30)
B^*	0.94335(24)	$B\pi\pi\pi$	1.14384(33)

Table 6.2: A summary of the stable meson masses and relevant kinematic thresholds for this calculation. The masses were determined through dispersion relations, with the B and the B^* dispersion relations shown in the previous chapter in Figure 5.3.

MeV. Fermions are calculated with a tadpole-improved Sheikholeslami-Wohlert (Wilson clover) action including stout-smeared spatial links [20, 22], as discussed in Chapter 2.

The anisotropy obtained from the pion dispersion relation is $\xi_\pi = 3.444(6)$ [30], while the anisotropy obtained from the B meson dispersion relation is $\xi_B = 3.365(14)$ (Chapter 5). For this calculation, the pion anisotropy will be used, but the systematic uncertainty resulting from the choice of anisotropy will be examined. The relevant meson masses calculated from dispersion relations, as well as the kinematic thresholds for this calculation are listed in Table 6.2.

6.1 Finite Volume Spectra

To calculate the finite volume spectra, the variational method is employed, as detailed in Chapter 3. The operator bases used only included meson-meson-like operators which are of the form $\sum_{\vec{p_1}+\vec{p_2}=\vec{P}} \mathcal{C}(\vec{p_1}, \vec{p_2})\Omega^\dagger_{M_1}(\vec{p_1})\Omega^\dagger_{M_2}(\vec{p_2})$, where $\Omega^\dagger_{M_i}(\vec{p_i})$ interpolates meson M_i with lattice momenta $\vec{p_i}$. These operators were constructed for each momentum from eigenvectors v^n that were determined in variational analyses of π, ρ, D, and D^* mesons. No "$q\bar{q}$"-like operators are included, as no states like this exist as an output for isospin-3/2 $B\pi$ scattering. Only at-rest irreps were considered in this study, such that the overall momentum of each state determined is zero. Tables listing the operators included in each irrep can be found in Appendix A2.

To obtain the energy levels, principal correlator fits were performed, as discussed in Chapter 3. Figure 6.1 shows the principal correlator fits of the first four energy levels
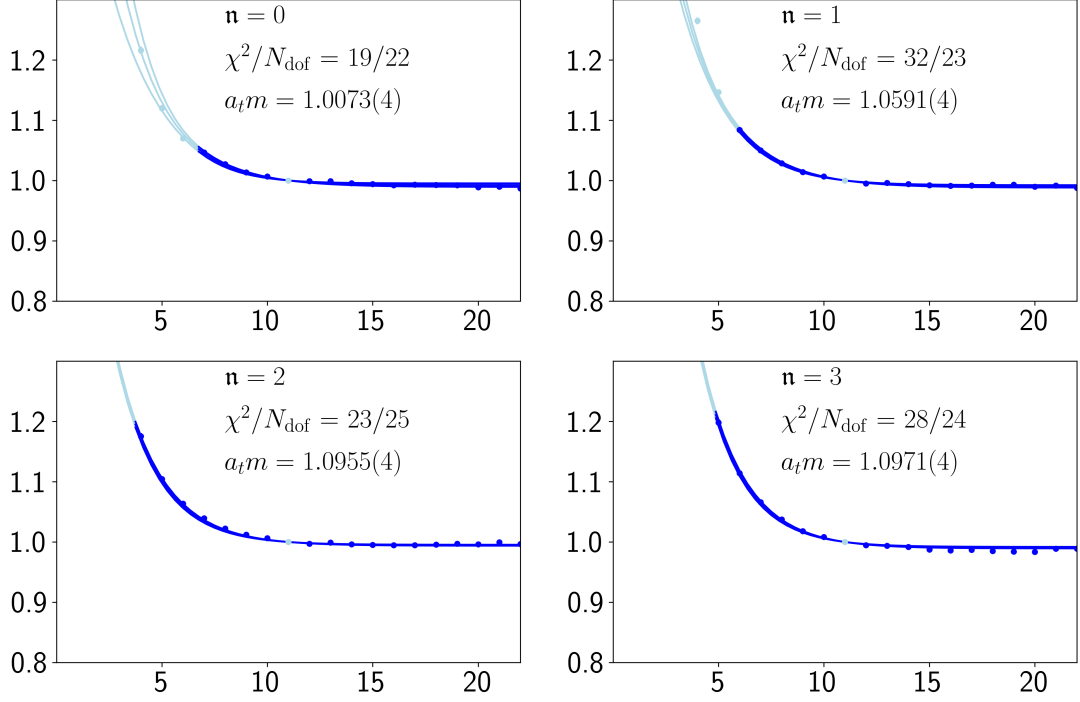
Figure 6.1: Principal correlator fits for the first 4 states, $\mathfrak{n} = 0, ..3$, in A_1^+ for $B\pi$ with $(L/a_s) = 20$. Shown is $e^{E_n(t-t_0)}\lambda_n(t)$ plotted against t/a_t. Darker points are included in the fits while the lighter ones are not.

calculated in the A_1^+ irrep, at $(L/a_s) = 20$. As in previous chapters, the dark points were included in the fit, while the lighter points were excluded. The masses and $\chi^2/N_{\rm dof}$ for each energy level are shown. A similar quality of fit was obtained across the different irreps and volumes.

Figure 6.2 shows the finite volume energy levels of the $[000]A_1^+$ on each of the three volumes, obtained from principal correlator fits. The states are marked as black/grey points, with the errorbars contained within the points. Red curves indicate relevant $B\pi$ non-interacting levels. The $B^*\rho$ non-interacting level is marked as a grey dashed line. Only states below this level were included in the subsequent scattering analysis, corresponding to the states coloured black. Other states determined in this analysis are coloured grey. Note that the effect of including $B^*\rho$ operators in the basis was investigated for states below the $B^*\rho$ non-interacting level. The effect was found to be negligible.

Figure 6.3 shows the finite volume spectra of the $[000]T_1^-$ and $[000]E^+$ irreps on the two volumes with $(L/a_s) = 16, 20$. Again, relevant non-interacting $B\pi$ levels are marked by the red curves. As can be seen, the states determined are consistent with the non-interacting levels. Similar to $D\pi$, as discussed in Chapter 4, this suggests that the

contributions of $B\pi$ partial waves with $\ell \geq 1$ are negligible, although no scattering analysis was performed for $\ell \geq 1$ in this study to verify this.
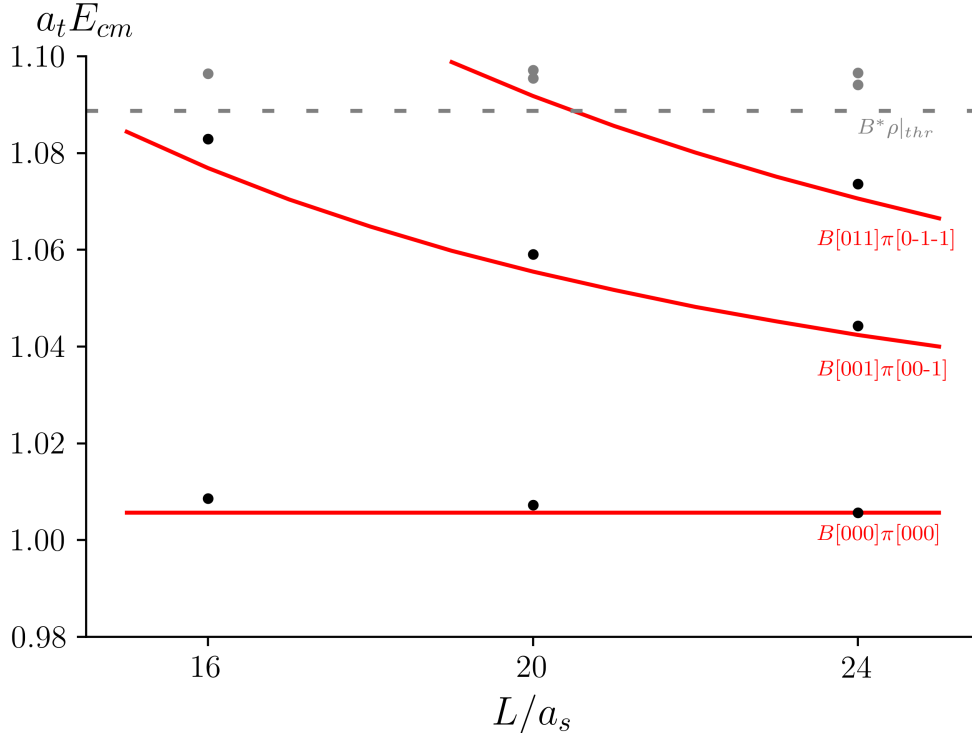
Figure 6.2: The finite volume spectrum determined for isospin-3/2 $B\pi$ scattering in the $[000]A_1^+$ irrep. Energy levels included in the subsequent scattering analysis are represented as black points. Grey points represent energy levels determined that were not included in the subsequent analysis, as discussed in the text. The red curves correspond to the non-interacting $B\pi$ energies. The grey-dashed line represents the $B^*\rho$ threshold, only levels below this threshold were used in the scattering analysis
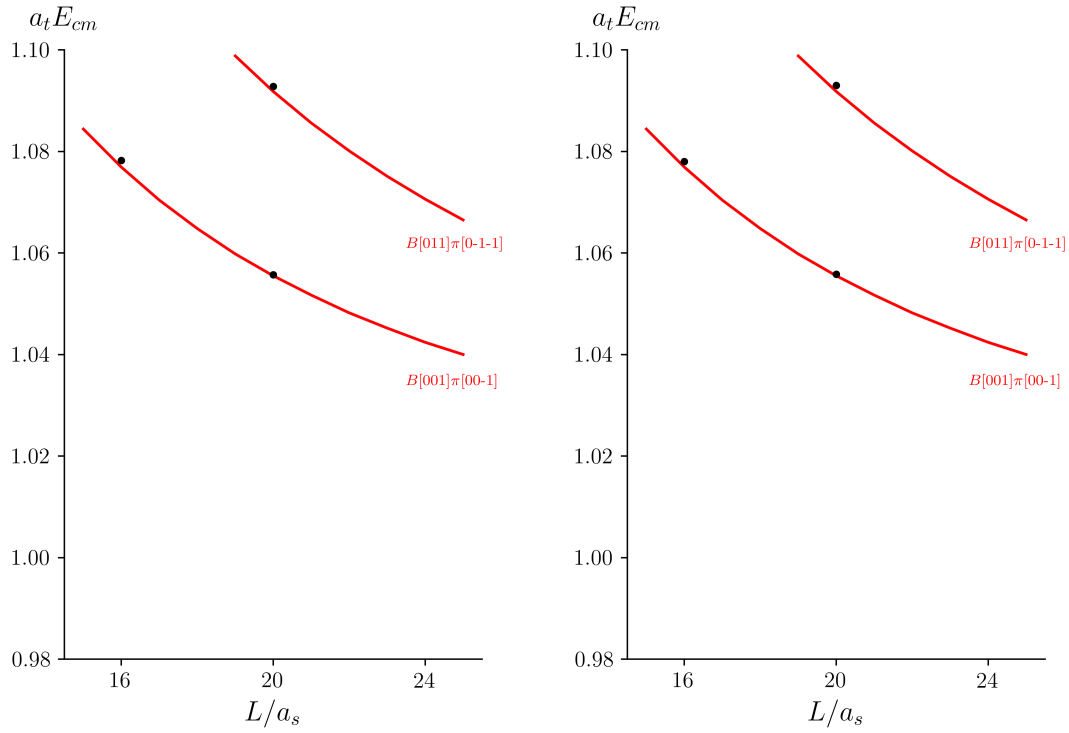
Figure 6.3: The finite volume spectrum determined for Isospin-3/2 $B\pi$ scattering in the $[000]\,T_1^-$ (left plot) and $[000]\,E^+$ (right plot) irreps. The red curves correspond to the non-interacting $B\pi$ energies.

6.2   Scattering Analysis

The S-wave isospin-3/2 $B\pi$ scattering amplitude was determined using Lüscher's determinant condition, as discussed in Chapter 3. The only at-rest irrep with $\ell = 0$ contributions is the $[000]\,A_1^+$ irrep. Below the $B^*\rho$ non-interacting level, there are seven energy levels across the three volumes. These were used to constrain the t-matrix parameterisations.

Using these energies, the phase shift δ was determined, calculating a value of δ for each energy level, while neglecting higher partial waves. The resulting phase shift is shown in Figure 6.4. The form of the phase shift is that of a weakly repulsive interaction.

As a reference parameterisation, a K-matrix parameterisation of the form

$$K = \gamma^0, \tag{6.1}$$

was used, with no pole term and with a Chew-Mandelstam phase space. A fit with this
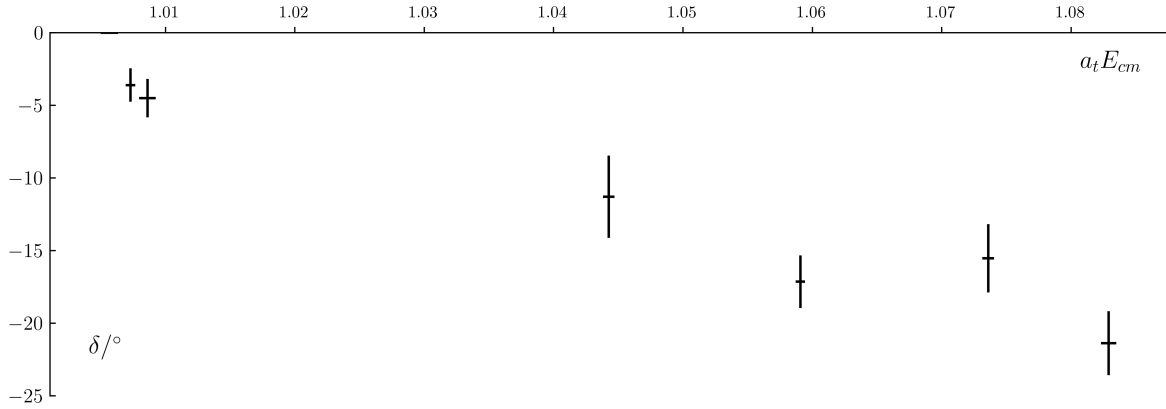
Figure 6.4: The S-wave phase shift δ for isospin-3/2 $B\pi$ scattering. The points were determined using the $[000]A_1^+$ energy levels shown in Figure 6.2.

parameterisation resulted in the parameter

$$
\begin{aligned}
\gamma_0 &= -1.57 \pm 0.10, \\
\chi^2/N_{\text{dof}} &= 1.02.
\end{aligned}
\tag{6.2}
$$

Using this reference amplitude parameterisation, the energy solutions to Lüscher's determinant condition were found. These are plotted as orange points in Figure 6.5. The previously determined states are plotted in black, and the non-interacting levels are the red curves, as before. One can see that the Lüscher solutions from the reference parameterisation are in agreement with the previously determined $B\pi$ energy levels, suggesting that the parameterisation is an adequate description of the data.

6.2.1 Parameterisation Variation

To determine the robustness of the results with respect to choice of parameterisation, a number of different parameterisations were fitted. Table 6.3 shows the parameterisations for which a fit succeeded. It is worth noting that any K-matrix parameterisation consisting of 2 free parameters failed to converge, suggesting that there are not enough energy levels are present to constrain the amplitude to multiple free parameters. However, a fit using a 2-parameter effective range expansion succeeded, and yielded the results

$$
\begin{aligned}
a_0 &= (-3.79 \pm 0.61) \cdot a_t \\
r_0 &= (-11.71 \pm 8.70) \cdot a_t
\end{aligned}
\qquad
\begin{bmatrix} 1.00 & 0.89 \\ & 1.00 \end{bmatrix}
$$

$$
\chi^2/N_{\text{dof}} = 1.17 \ .
\tag{6.3}
$$
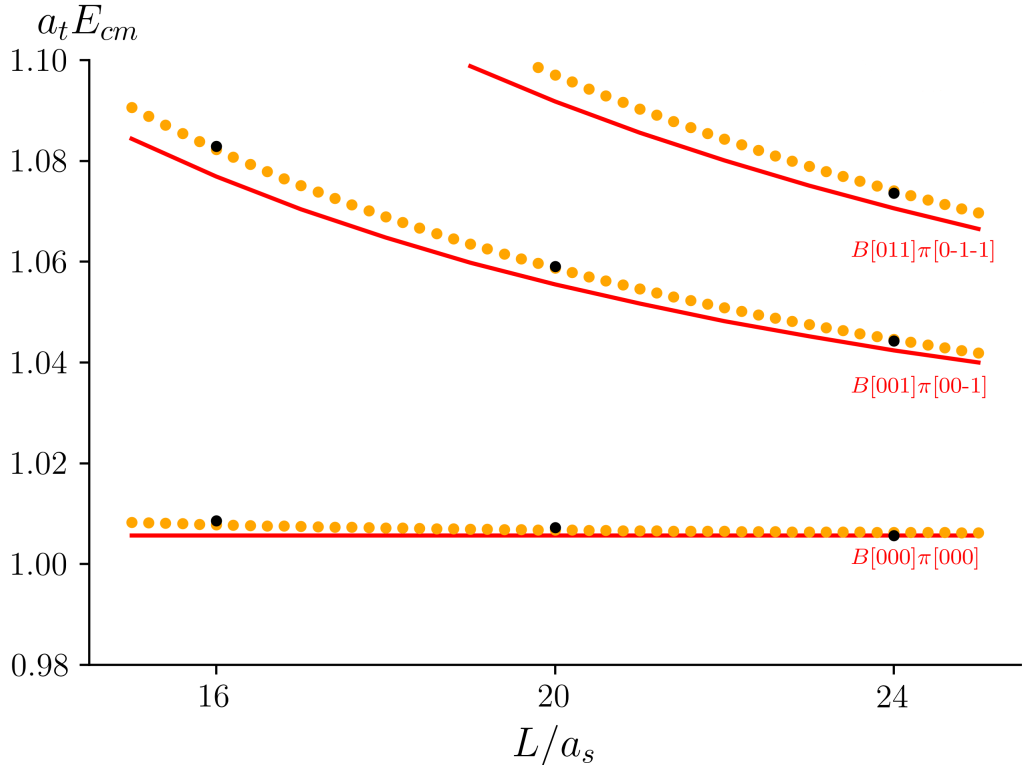
Figure 6.5: Same as Figure 6.2 but with the solutions to the Lüscher condition from the reference parameterisation (of the form shown in Eq 6.1) plotted as orange points

Using the parameterisations listed in Table 6.3, a phase shift δ can be determined. This is shown in Figure 6.6, where the phase shift determined from the reference amplitude is plotted as a solid red curve. The inner error band arises from the variation of parameterisation. The outer band represents the systematic error, which arises from the variation of the input hadron masses to their maximum and minimum values within their statistical errors. The previously determined phase shift from Figure 6.4 are also shown as points, demonstrating the consistency between the two approaches.

Parameterisation	N_{pars}	χ^2/N_{dof}
K-matrix with a Chew-Mandelstam $I(s)$		
$K = \gamma^{(0)}$	1	1.02
$K = \gamma^{(1)}$	1	1.69
K-matrix with $I(s) = -i\rho(s)$		
$K = \gamma^{(0)}$	1	0.99
$K = \gamma^{(1)}s$	1	1.64
Effective range expansion		
$k\cot\delta_0 = 1/a_0$	1	1.29
$k\cot\delta_0 = 1/a_0 + \frac{1}{2}r_0^2 k^2$	2	1.17

Table 6.3: The parametrisations used in the study of elastic isospin-3/2 $B\pi$ scattering for $\xi = \xi_\pi = 3.444$. N_{pars} indicates the number of free paramaters in each parametrisation.
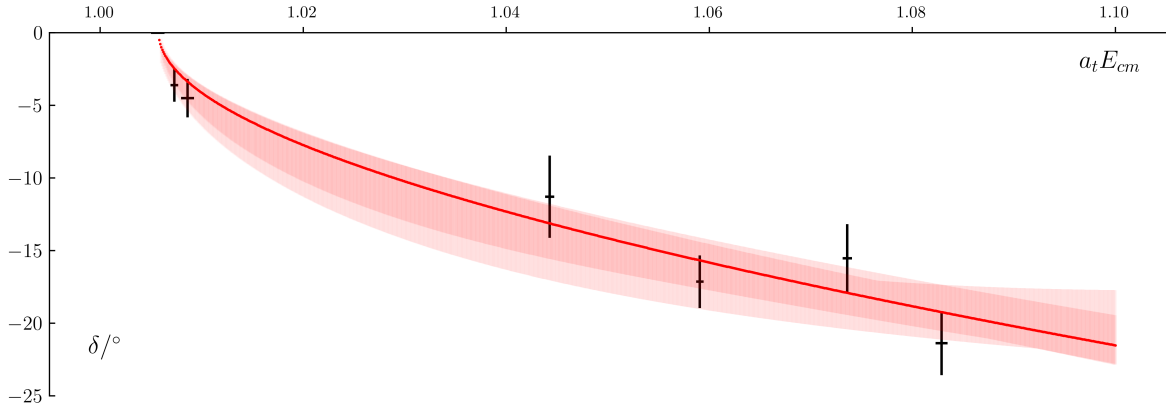
Figure 6.6: The S-wave phase shift δ_0 for isospin-3/2 $B\pi$ scattering with anisotropy $\xi = \xi_\pi = 3.444$. The reference parameterisation of the form Eq 6.1 is shown as a solid line. The inner band encompasses all parameterisations determined with acceptable χ^2/N_{dof}, while the outer band accounts for uncertainties arising from the variation of input masses within their statistical error. The points from Figure 6.4 are also shown.

6.2.2 Anisotropy Variation

The variation of systematics was discussed above, but the systematic uncertainty due to the choice of anisotropy has not been included in the analysis so far. As mentioned in the Chapter 5, the anisotropy determined from the B meson dispersion relation, on a lattice of volume $(20)^3 \times 128$, is $\xi_B = 3.365(14)$ (see Table 5.2). This difference from $\xi_{pi} = 3.444(6)$ was taken into account and the anisotropy was varied between $\xi \in [\xi_B, \xi_\pi]$, as an investigation into the dependence of the results on the anisotropy.

Figure 6.7 shows the effect of varying the anisotropy on the reference parameterisation given in Eqn 6.1. The left plot shows the effect on the free parameter γ_0 (from
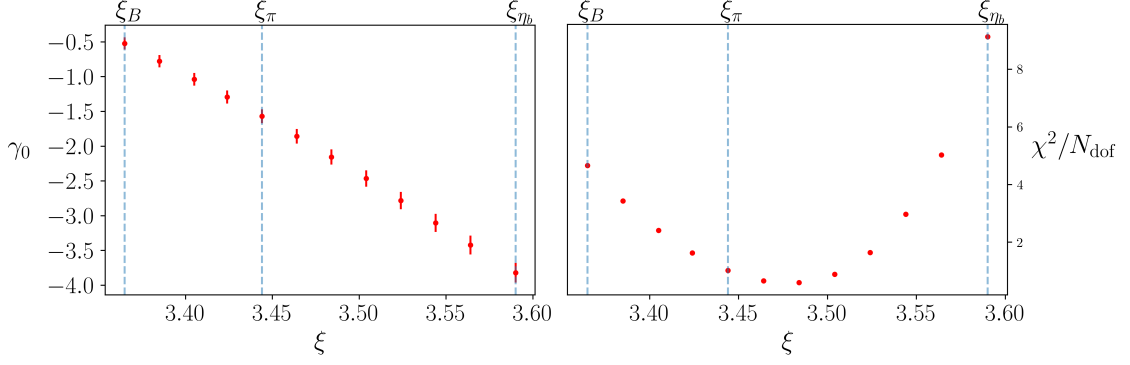
Figure 6.7: The effect of varying the anisotropy ξ on the reference parameterisation. The change in the parameter γ_0 is shown in the left plot, while the corresponding χ^2/N_{dof} are shown in the right plot.

the reference parameterisation in Eq 6.1) while the right plot shows the corresponding χ^2/N_{dof} for each fit. As a dependence on the anisotropy was found, this investigation was extended to include the anisotropy determined from the η_b dispersion relation in Ref [95], $\xi_{\eta_b} = 3.590(15)$.

Varying to an anisotropy greater than ξ_π does not make sense physically, as the interaction is between the B meson and the π meson. However, the systematic uncertainty rising from the choice of anisotropy must also be taken into account. For this reason, a second set of fits were performed for $\xi = 3.424$, as it was the only anisotropy tested in the range $\xi = [\xi_B, \xi_\pi]$, with a $\chi^2/N_{\mathrm{dof}} < 2$, other than the already fitted pion anisotropy. The corresponding reference parameterisation for $\xi = 3.424$ is

$$
\begin{aligned}
\gamma_0 &= -1.29 \pm 0.09, \\
\chi^2/N_{\mathrm{dof}} &= 1.62,
\end{aligned}
\tag{6.4}
$$

which is within 3σ of the previously determined fit in Eqn 6.2.

The list of parameterisations successfully fitted at this second anisotropy $\xi = 3.424$ is shown in Table 6.4, with the number of free parameters and χ^2/N_{dof} noted. Once again, the only 2-parameter fit to successfully converge was the effective range expansion, yielding

$$
\begin{aligned}
a_0 &= (-3.71 \pm 0.71) \cdot a_t \\
r_0 &= (-21.88 \pm 11.53) \cdot a_t
\end{aligned}
\qquad
\begin{bmatrix} 1.00 & 0.88 \\ & 1.00 \end{bmatrix}
$$

$$
\chi^2/N_{\mathrm{dof}} = 1.58 \ . \tag{6.5}
$$

The parameters are within 1σ of those obtained from the effective range expansion fitted at the pion anisotropy (Eqn 6.3), although it must be noted that the r_0 parameter is

Parameterisation	N_{pars}	χ^2/N_{dof}
K-matrix with a Chew-Mandelstam $I(s)$		
$K = \gamma^{(0)}$	1	1.63
$K = \gamma^{(1)}$	1	2.27
K-matrix with $I(s) = -i\rho(s)$		
$K = \gamma^{(0)}$	1	1.60
$K = \gamma^{(1)}s$	1	2.24
Effective range expansion		
$k \cot \delta_0 = 1/a_0$	1	1.91
$k \cot \delta_0 = 1/a_0 + \frac{1}{2}r_0^2 k^2$	2	1.58

Table 6.4: The parametrisations used in the study of elastic isospin-3/2 $B\pi$ scattering for $\xi = 3.424$. N_{pars} indicates the number of free paramaters in each parametrisation.

significantly larger with a sizeable error at this second anisotropy. It is worth noting that at this second anisotropy, the linear K-matrix parameterisation fit had a $\chi^2/N_{\text{dof}} > 2$, for both choices of phase $I(s)$. Thus both these fits were excluded from the final results.

Shown in Figure 6.8 is the comparison between the phase shifts at the two different anisotropies. The phase shift calculated from the reference parameterisation is plotted as a solid curve, with red corresponding to $\xi = 3.444$ and blue corresponding to $\xi = 3.424$. The errorbands around each of the curves correspond to the variation rising from changing the parameterisation, only considering parameterisations with a $\chi^2/N_{\text{dof}} < 2$. The points from Figure 6.4 are shown in red, while the blue points correspond to the phase shift determined using the energy levels coloured black in Figure 6.2 with $\xi = 3.424$
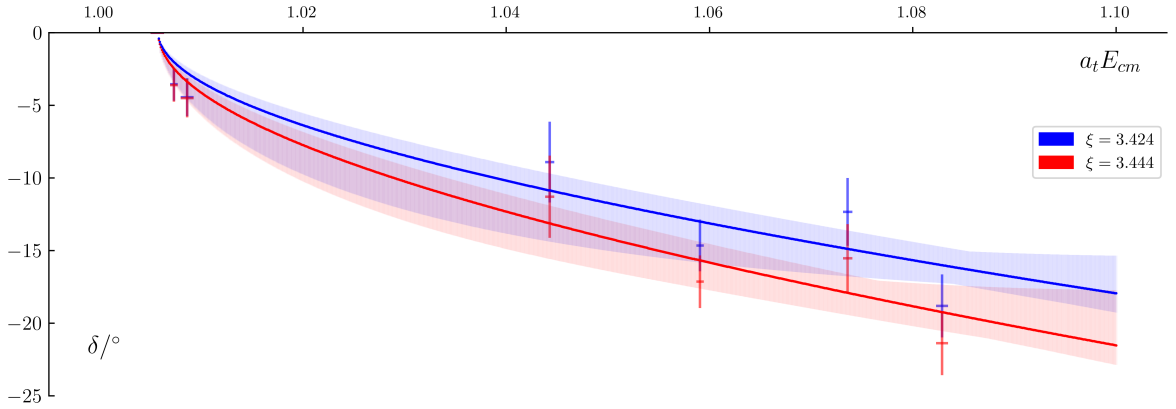
Figure 6.8: The *S*-wave phase shift δ_0 for isospin-3/2 $B\pi$ scattering. The parameterisation shown is the reference parameterisation, as detailed in Eq 6.1, with red corresponding to $\xi = 3.444$ and blue corresponding to $\xi = 3.424$. The band covers all parameterisations determined with acceptable χ^2/N_{dof}. The points from Figure 6.4 are shown in red. The blue points are the phase shift determined using the black points in Figure 6.2 with $\xi = 3.424$.

6.3 Outlook

As mentioned at the start of this chapter, isospin-3/2 $D\pi$ scattering was investigated previously in Ref [2]. A similar shape was found for the phase shift, resembling a weakly repulsive interaction. In that study, two-parameter parameterisations of the *t*-matrix were determined to be the best description of the energy levels calculated, in contrast to this study. However, this study contained no irreps with non-zero momentum, a key difference between the two studies.

A final plot of the isospin-3/2 $B\pi$ *S*-wave phase shift is shown in Figure 6.9. This corresponds to the phase shift determined from the reference parameterisation at $\xi = 3.444$, with the first errorband representing the effect of varying the *t*-matrix parameterisation, as in Figure 6.6. The outerband now contains systematic errors arising from the variation of input hadron masses within their statistical error and anisotropy values over the range $\xi \in [3.424, 3.444]$.

A conservative estimate of the scattering length, taking the average over the four fits which were the form of the effective range expansion yields

$$a_0 = (-3.2 \pm 1.0) \cdot a_t = -0.11 \pm 0.03 \text{ fm}. \qquad (6.6)$$
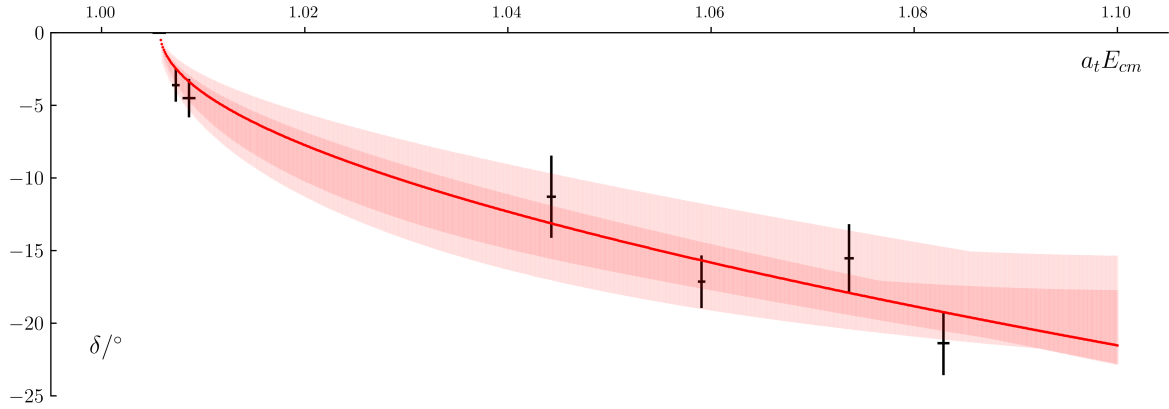
Figure 6.9: The *S*-wave phase shift δ_0 for isospin-3/2 $B\pi$ scattering. The reference parameterisation is shown, of the form shown in Eq 6.1. The inner band covers all parameterisations determined with acceptable χ^2/N_{dof}, while the outer band accounts for uncertainties arising from the variation of input masses and anisotropy. The points from Figure 6.4 are also shown.

It is clear that the scattering methods that were successfully used in the light and charm sectors are working in the heavy-light sector. The next steps in the study of isospin-3/2 $B\pi$ scatteing would be to first include states above the $B^\star\rho$ threshold, and do a coupled channel analysis, treating the ρ as a stable particle. Investigating the effect on the amplitude of including moving frame irreps would also be important. Confirming that contributions of partial waves with $\ell \geq 1$ are negligible would be desirable. Finally, moving on from this, studying the isospin-1/2 $B\pi$ scattering process would be very interesting. The study of $Q\bar{q}$ states such as the B_0^* should be fascinating, especially considering the results of the study of $D\pi$, detailed in Chapter 4. The scattering of $B\pi$ still has much left to explore.

7   Conclusion

In this thesis, heavy hadron spectroscopy was studied using the formalism of lattice quantum chromodynamics. This involved the determination of finite-volume spectra through the evaluation of correlators in the distillation framework from a basis of appropriate operators. These spectra were related to infinite-volume scattering amplitudes using Lüscher's method. In Chapter 4, isospin-1/2 $D\pi$ scattering amplitudes were computed. The elastic S-wave amplitude was analytically continued to complex energies in search of poles. A resonance pole was found, which was identified to be the D_0^* meson. The amplitude is of a similar shape to experimental observations but the mass calculated in this study is below the value currently reported. This is in agreement with a similar study performed at a higher pion mass. Extrapolating to physical pion mass suggests that the current reported mass of the D_0^* is too high.

In Chapter 5, a calculation of the excited and exotic spectra of the B, B_s and B_c mesons is described. An extensive spectra was calculated in each of the three meson sectors using a relativistic b quark, with robust spin identification. The pattern of states observed is similar to those previously observed in the charmed meson sector. The presence of exotic hybrid mesons was investigated, with hybrid mesons identified in each of the three meson sectors. These states were proposed to be candidate states of a hybrid supermultiplet in each sector. An investigation into the mixing of spin-singlet and spin-triplet states was performed, a phenomenon occurring due to heavy-light meson states not being eigenstates of charge conjugation on the lattice. The dependence of the mixing angle between pairs of spin-singlet and spin-triplet states, on the mass difference of the constituent quarks of the meson was examined. As previously predicted, there is more mixing in B and B_s than there is in D and D_s. Mixing in B_c on the other hand, was found to be much weaker than in the heavy-light mesons, and is much closer to zero mixing, as is observed in quarkonium.

Finally, Chapter 6 detailed an exploratory study of isospin-3/2 $B\pi$ scattering. The S-wave scattering amplitude was computed, and was found to be a similar shape to previously calculated isospin-3/2 $D\pi$ S-wave scattering amplitude, both being the form

of a weakly repulsive interaction. The systematic errors were investigated through the variation of input hadron masses and anisotropy, as well as of t-matrix parameterisations. A noteworthy dependence was found on the anisotropy, although that may be solved through the inclusion of more energy levels in a coupled channel analysis or through the addition of energy levels from moving-frame irreps.

It should be noted that all of the results presented in this thesis were calculated using a single lattice spacing, and at unphysical pion masses. Finite volume effects were explored through the variation of the spatial volume of the lattice. All of these contribute to systematic errors that were beyond the remit of this thesis. Nevertheless, the results obtained from the methods outlined in this work are promising, and there are clearly many prospects in the investigation of hadrons containing a bottom quark, with hopefully many more developments to come.

Bibliography

[1] L. Gayer, N. Lang, S. M. Ryan, D. Tims, C. E. Thomas, and D. J. Wilson, "Isospin-1/2 $D\pi$ scattering and the lightest D_0^* resonance from lattice QCD," *JHEP*, vol. 07, p. 123, 2021.

[2] G. Moir, M. Peardon, S. M. Ryan, C. E. Thomas, and D. J. Wilson, "Coupled-Channel $D\pi$, $D\eta$ and $D_s\bar{K}$ Scattering from Lattice QCD," *JHEP*, vol. 10, p. 011, 2016.

[3] G. K. Cheung, C. E. Thomas, D. J. Wilson, G. Moir, M. Peardon, and S. M. Ryan, "$DK\ I = 0$, $D\bar{K}\ I = 0, 1$ scattering and the $D_{s0}^*(2317)$ from lattice QCD," 8 2020.

[4] G. Moir, M. Peardon, S. M. Ryan, C. E. Thomas, and L. Liu, "Excited spectroscopy of charmed mesons from lattice QCD," *JHEP*, vol. 05, p. 021, 2013.

[5] M. Gell-Mann, "The Eightfold Way: A Theory of strong interaction symmetry," 3 1961.

[6] G. Zweig, *An SU(3) model for strong interaction symmetry and its breaking. Version 2*, 2 1964, pp. 22–101.

[7] R. L. Workman *et al.*, "Review of Particle Physics Chapter 15: Quark Model," *PTEP*, vol. 2022, p. 083C01, 2022.

[8] A. Pich, "Introduction to chiral perturbation theory," *AIP Conf. Proc.*, vol. 317, pp. 95–140, 1994.

[9] E. Eichten and B. R. Hill, "An Effective Field Theory for the Calculation of Matrix Elements Involving Heavy Quarks," *Phys. Lett. B*, vol. 234, pp. 511–516, 1990.

[10] M. Luscher and U. Wolff, "How to Calculate the Elastic Scattering Matrix in Two-dimensional Quantum Field Theories by Numerical Simulation," *Nucl. Phys. B*, vol. 339, pp. 222–252, 1990.

[11] L. E. LHCb Collaboration, "Future physics potential of LHCb," CERN, Geneva, Tech. Rep., 2022. [Online]. Available: http://cds.cern.ch/record/2806113

[12] L. Aggarwal *et al.*, "Snowmass White Paper: Belle II physics reach and plans for the next decade and beyond," 7 2022.

[13] C. Gattringer and C. B. Lang, *Quantum chromodynamics on the lattice*. Berlin: Springer, 2010, vol. 788.

[14] S. Elitzur, "Impossibility of Spontaneously Breaking Local Symmetries," *Phys. Rev. D*, vol. 12, pp. 3978–3982, 1975.

[15] K. G. Wilson, "Quarks and Strings on a Lattice," in *13th International School of Subnuclear Physics: New Phenomena in Subnuclear Physics*, 11 1975.

[16] J. B. Kogut and L. Susskind, "Hamiltonian Formulation of Wilson's Lattice Gauge Theories," *Phys. Rev. D*, vol. 11, pp. 395–408, 1975.

[17] D. B. Kaplan, "A Method for simulating chiral fermions on the lattice," *Phys. Lett. B*, vol. 288, pp. 342–347, 1992.

[18] R. Frezzotti, P. A. Grassi, S. Sint, and P. Weisz, "Lattice QCD with a chirally twisted mass term," *JHEP*, vol. 08, p. 058, 2001.

[19] K. Symanzik, "Continuum Limit and Improved Action in Lattice Theories. 1. Principles and φ^4 Theory," *Nucl. Phys. B*, vol. 226, pp. 187–204, 1983.

[20] B. Sheikholeslami and R. Wohlert, "Improved Continuum Limit Lattice Action for QCD with Wilson Fermions," *Nucl. Phys. B*, vol. 259, p. 572, 1985.

[21] M. Luscher and P. Weisz, "On-Shell Improved Lattice Gauge Theories," *Commun. Math. Phys.*, vol. 97, p. 59, 1985, [Erratum: Commun.Math.Phys. 98, 433 (1985)].

[22] C. Morningstar and M. J. Peardon, "Analytic smearing of SU(3) link variables in lattice QCD," *Phys. Rev. D*, vol. 69, p. 054501, 2004.

[23] G. P. Lepage and P. B. Mackenzie, "On the viability of lattice perturbation theory," *Phys. Rev. D*, vol. 48, pp. 2250–2264, 1993.

[24] H.-W. Lin *et al.*, "First results from 2+1 dynamical quark flavors on an anisotropic lattice: Light-hadron spectroscopy and setting the strange-quark mass," *Phys. Rev. D*, vol. 79, p. 034502, 2009.

[25] S. Duane, A. D. Kennedy, B. J. Pendleton, and D. Roweth, "Hybrid Monte Carlo," *Phys. Lett. B*, vol. 195, pp. 216–222, 1987.

[26] B. A. Galloway, P. Knecht, J. Koponen, C. T. H. Davies, and G. P. Lepage, "Radial and orbital excitation energies of charmonium," *PoS*, vol. LATTICE2014, p. 092, 2014.

[27] D. Hatton, C. T. H. Davies, B. Galloway, J. Koponen, G. P. Lepage, and A. T. Lytle, "Charmonium properties from lattice QCD+QED : Hyperfine splitting, J/ψ leptonic width, charm quark mass, and a_μ^c," *Phys. Rev. D*, vol. 102, no. 5, p. 054511, 2020.

[28] R. G. Edwards, B. Joo, and H.-W. Lin, "Tuning for Three-flavors of Anisotropic Clover Fermions with Stout-link Smearing," *Phys. Rev. D*, vol. 78, p. 054501, 2008.

[29] J. J. Dudek, R. G. Edwards, M. J. Peardon, D. G. Richards, and C. E. Thomas, "Toward the excited meson spectrum of dynamical QCD," *Phys. Rev. D*, vol. 82, p. 034508, 2010.

[30] J. J. Dudek, R. G. Edwards, and C. E. Thomas, "S and D-wave phase shifts in isospin-2 pi pi scattering from lattice QCD," *Phys. Rev. D*, vol. 86, p. 034031, 2012.

[31] J. J. Dudek, "The lightest hybrid meson supermultiplet in QCD," *Phys. Rev. D*, vol. 84, p. 074023, 2011.

[32] L. Liu, G. Moir, M. Peardon, S. M. Ryan, C. E. Thomas, P. Vilaseca, J. J. Dudek, R. G. Edwards, B. Joo, and D. G. Richards, "Excited and exotic charmonium spectroscopy from lattice QCD," *JHEP*, vol. 07, p. 126, 2012.

[33] F. Knechtli, M. Günther, and M. Peardon, *Lattice Quantum Chromodynamics: Practical Essentials*, ser. SpringerBriefs in Physics.   Springer, 2017.

[34] M. Peardon *et al.*, "A novel quark-field creation operator construction for hadronic physics in lattice QCD," *Phys. Rev.*, vol. D80, p. 054506, 2009.

[35] G. P. Lepage, B. Clark, C. T. H. Davies, K. Hornbostel, P. B. Mackenzie, C. Morningstar, and H. Trottier, "Constrained curve fitting," *Nucl. Phys. B Proc. Suppl.*, vol. 106, pp. 12–20, 2002.

[36] C. Michael, "Adjoint Sources in Lattice Gauge Theory," *Nucl. Phys. B*, vol. 259, pp. 58–76, 1985.

[37] B. Blossier, M. Della Morte, G. von Hippel, T. Mendes, and R. Sommer, "On the generalized eigenvalue method for energies and matrix elements in lattice field theory," *JHEP*, vol. 04, p. 094, 2009.

[38] S. Mandelstam, "Determination of the pion - nucleon scattering amplitude from dispersion relations and unitarity. General theory," *Phys. Rev.*, vol. 112, pp. 1344–1360, 1958.

[39] R. A. Briceno, J. J. Dudek, and R. D. Young, "Scattering processes and resonances from lattice QCD," *Rev. Mod. Phys.*, vol. 90, no. 2, p. 025001, 2018.

[40] J. R. Taylor, *Scattering Theory: The Quantum Theory of Nonrelativistic Collisions*. New York: John Wiley & Sons, Inc., 1972.

[41] G. F. Chew and S. Mandelstam, "Theory of low-energy pion pion interactions," *Phys. Rev.*, vol. 119, pp. 467–477, 1960.

[42] M. Luscher, "Volume Dependence of the Energy Spectrum in Massive Quantum Field Theories. 1. Stable Particle States," *Commun. Math. Phys.*, vol. 104, p. 177, 1986.

[43] ——, "Two particle states on a torus and their relation to the scattering matrix," *Nucl. Phys. B*, vol. 354, pp. 531–578, 1991.

[44] ——, "Signatures of unstable particles in finite volume," *Nucl. Phys. B*, vol. 364, pp. 237–251, 1991.

[45] K. Rummukainen and S. A. Gottlieb, "Resonance scattering phase shifts on a nonrest frame lattice," *Nucl. Phys. B*, vol. 450, pp. 397–436, 1995.

[46] C. h. Kim, C. T. Sachrajda, and S. R. Sharpe, "Finite-volume effects for two-hadron states in moving frames," *Nucl. Phys. B*, vol. 727, pp. 218–243, 2005.

[47] N. H. Christ, C. Kim, and T. Yamazaki, "Finite volume corrections to the two-particle decay of states with non-zero momentum," *Phys. Rev. D*, vol. 72, p. 114506, 2005.

[48] Z. Fu, "Rummukainen-Gottlieb's formula on two-particle system with different mass," *Phys. Rev. D*, vol. 85, p. 014506, 2012.

[49] L. Leskovec and S. Prelovsek, "Scattering phase shifts for two particles of different mass and non-zero total momentum in lattice QCD," *Phys. Rev. D*, vol. 85, p. 114507, 2012.

[50] M. T. Hansen and S. R. Sharpe, "Multiple-channel generalization of Lellouch-Luscher formula," *Phys. Rev. D*, vol. 86, p. 016007, 2012.

[51] R. A. Briceno and Z. Davoudi, "Moving multichannel systems in a finite volume with application to proton-proton fusion," *Phys. Rev. D*, vol. 88, no. 9, p. 094507, 2013.

[52] P. Guo, J. Dudek, R. Edwards, and A. P. Szczepaniak, "Coupled-channel scattering on a torus," *Phys. Rev. D*, vol. 88, no. 1, p. 014501, 2013.

[53] R. A. Briceno, "Two-particle multichannel systems in a finite volume with arbitrary spin," *Phys. Rev. D*, vol. 89, no. 7, p. 074507, 2014.

[54] K. Abe *et al.*, "Study of B- —> D**0 pi- (D**0 —> D(*)+ pi-) decays," *Phys. Rev. D*, vol. 69, p. 112002, 2004.

[55] B. Aubert *et al.*, "Dalitz Plot Analysis of B- —> D+ pi- pi-," *Phys. Rev. D*, vol. 79, p. 112004, 2009.

[56] R. Aaij *et al.*, "Dalitz plot analysis of $B^0 \to \overline{D}^0 \pi^+ \pi^-$ decays," *Phys. Rev. D*, vol. 92, no. 3, p. 032002, 2015.

[57] D. J. Wilson, R. A. Briceno, J. J. Dudek, R. G. Edwards, and C. E. Thomas, "The quark-mass dependence of elastic πK scattering from QCD," *Phys. Rev. Lett.*, vol. 123, no. 4, p. 042002, 2019.

[58] G. K. C. Cheung, C. O'Hara, G. Moir, M. Peardon, S. M. Ryan, C. E. Thomas, and D. Tims, "Excited and exotic charmonium, D_s and D meson spectra for two light quark masses from lattice QCD," *JHEP*, vol. 12, p. 089, 2016.

[59] D. J. Wilson, R. A. Briceno, J. J. Dudek, R. G. Edwards, and C. E. Thomas, "Coupled $\pi\pi, K\bar{K}$ scattering in P-wave and the ρ resonance from lattice QCD," *Phys. Rev.*, vol. D92, no. 9, p. 094502, 2015.

[60] C. E. Thomas, R. G. Edwards, and J. J. Dudek, "Helicity operators for mesons in flight on the lattice," *Phys. Rev. D*, vol. 85, p. 014507, 2012.

[61] R. A. Briceno, J. J. Dudek, R. G. Edwards, and D. J. Wilson, "Isoscalar $\pi\pi$ scattering and the σ meson resonance from QCD," *Phys. Rev. Lett.*, vol. 118, no. 2, p. 022002, 2017.

[62] S. Godfrey and N. Isgur, "Mesons in a Relativized Quark Model with Chromodynamics," *Phys. Rev. D*, vol. 32, pp. 189–231, 1985.

[63] S. Godfrey, "Spectroscopy of B_c mesons in the relativized quark model," *Phys. Rev. D*, vol. 70, p. 054017, 2004.

[64] T. A. Lahde, C. J. Nyfalt, and D. O. Riska, "Spectra and M1 decay widths of heavy light mesons," *Nucl. Phys. A*, vol. 674, pp. 141–167, 2000.

[65] M. Di Pierro and E. Eichten, "Excited Heavy - Light Systems and Hadronic Transitions," *Phys. Rev. D*, vol. 64, p. 114004, 2001.

[66] D. Ebert, R. N. Faustov, and V. O. Galkin, "Heavy-light meson spectroscopy and Regge trajectories in the relativistic quark model," *Eur. Phys. J. C*, vol. 66, pp. 197–206, 2010.

[67] Y. Sun, Q.-T. Song, D.-Y. Chen, X. Liu, and S.-L. Zhu, "Higher bottom and bottom-strange mesons," *Phys. Rev. D*, vol. 89, no. 5, p. 054026, 2014.

[68] Q.-F. Lü, T.-T. Pan, Y.-Y. Wang, E. Wang, and D.-M. Li, "Excited bottom and bottom-strange mesons in the quark model," *Phys. Rev. D*, vol. 94, no. 7, p. 074012, 2016.

[69] P. G. Ortega, J. Segovia, D. R. Entem, and F. Fernández, "Threshold effects in P-wave bottom-strange mesons," *Phys. Rev. D*, vol. 95, no. 3, p. 034010, 2017.

[70] P. G. Ortega, J. Segovia, D. R. Entem, and F. Fernandez, "Spectroscopy of $\mathbf{B_c}$ mesons and the possibility of finding exotic $\mathbf{B_c}$-like structures," *Eur. Phys. J. C*, vol. 80, no. 3, p. 223, 2020.

[71] B. Martín-González, P. G. Ortega, D. R. Entem, F. Fernández, and J. Segovia, "Toward the discovery of novel Bc states: Radiative and hadronic transitions," *Phys. Rev. D*, vol. 106, no. 5, p. 054009, 2022.

[72] A. M. Green, J. Koponen, C. McNeile, C. Michael, and G. Thompson, "Excited B mesons from the lattice," *Phys. Rev. D*, vol. 69, p. 094505, 2004.

[73] J. Koponen, "Energies of B_s meson excited states: A Lattice study," *Phys. Rev. D*, vol. 78, p. 074509, 2008.

[74] ——, "Energies and radial distributions of B(s) mesons on the lattice," *Acta Phys. Polon. B*, vol. 38, pp. 2893–2900, 2007.

[75] J. Foley, A. O'Cais, M. Peardon, and S. M. Ryan, "Radial and orbital excitations of static-light mesons," *Phys. Rev. D*, vol. 75, p. 094503, 2007.

[76] K. Jansen, C. Michael, A. Shindler, and M. Wagner, "The Static-light meson spectrum from twisted mass lattice QCD," *JHEP*, vol. 12, p. 058, 2008.

[77] T. Burch, C. Hagen, C. B. Lang, M. Limmer, and A. Schafer, "Excitations of single-beauty hadrons," *Phys. Rev. D*, vol. 79, p. 014504, 2009.

[78] C. Michael, A. Shindler, and M. Wagner, "The continuum limit of the static-light meson spectrum," *JHEP*, vol. 08, p. 009, 2010.

[79] F. Bernardoni, B. Blossier, J. Bulava, M. Della Morte, P. Fritzsch, N. Garron, A. Gérardin, J. Heitger, G. von Hippel, and H. Simma, "B-meson spectroscopy in HQET at order 1/m," *Phys. Rev. D*, vol. 92, no. 5, p. 054509, 2015.

[80] I. F. Allison, C. T. H. Davies, A. Gray, A. S. Kronfeld, P. B. Mackenzie, and J. N. Simone, "Mass of the B_c meson in three-flavor lattice QCD," *Phys. Rev. Lett.*, vol. 94, p. 172001, 2005.

[81] E. B. Gregory, C. T. H. Davies, E. Follana, E. Gamiz, I. D. Kendall, G. P. Lepage, H. Na, J. Shigemitsu, and K. Y. Wong, "A Prediction of the B*(c) mass in full lattice QCD," *Phys. Rev. Lett.*, vol. 104, p. 022001, 2010.

[82] E. B. Gregory *et al.*, "Precise B, B_s and B_c meson spectroscopy from full lattice QCD," *Phys. Rev. D*, vol. 83, p. 014506, 2011.

[83] M. Wurtz, R. Lewis, and R. M. Woloshyn, "Free-form smearing for bottomonium and B meson spectroscopy," *Phys. Rev. D*, vol. 92, no. 5, p. 054504, 2015.

[84] N. Mathur, M. Padmanath, and S. Mondal, "Precise predictions of charmed-bottom hadrons from lattice QCD," *Phys. Rev. Lett.*, vol. 121, no. 20, p. 202002, 2018.

[85] C. Peset, A. Pineda, and J. Segovia, "P-wave heavy quarkonium spectrum with next-to-next-to-next-to-leading logarithmic accuracy," *Phys. Rev. D*, vol. 98, no. 9, p. 094003, 2018.

[86] C. McNeile, C. T. H. Davies, E. Follana, K. Hornbostel, and G. P. Lepage, "Heavy meson masses and decay constants from relativistic heavy quarks in full lattice QCD," *Phys. Rev. D*, vol. 86, p. 074503, 2012.

[87] A. Lytle, B. Colquhoun, C. Davies, and J. Koponen, "B_c spectroscopy using highly improved staggered quarks," *PoS*, vol. LATTICE2018, p. 083, 2018.

[88] C. B. Lang, D. Mohler, S. Prelovsek, and R. M. Woloshyn, "Predicting positive parity B$_s$ mesons from lattice QCD," *Phys. Lett. B*, vol. 750, pp. 17–21, 2015.

[89] C. B. Lang, D. Mohler, and S. Prelovsek, "$B_s\pi^+$ scattering and search for X(5568) with lattice QCD," *Phys. Rev. D*, vol. 94, p. 074509, 2016.

[90] M. Albaladejo, P. Fernandez-Soler, J. Nieves, and P. G. Ortega, "Lowest-lying even-parity $\bar{B}_s$ mesons: heavy-quark spin-flavor symmetry, chiral dynamics, and

constituent quark-model bare masses," *Eur. Phys. J. C*, vol. 77, no. 3, p. 170, 2017.

[91] R. J. Hudspith and D. Mohler, "Exotic tetraquark states with two b‾ quarks and JP=0+ and 1+ Bs states in a nonperturbatively tuned lattice NRQCD setup," *Phys. Rev. D*, vol. 107, no. 11, p. 114510, 2023.

[92] W. Chen, T. G. Steele, and S.-L. Zhu, "Masses of the bottom-charm hybrid $\bar{b}Gc$ states," *J. Phys. G*, vol. 41, p. 025003, 2014.

[93] M. Berwein, N. Brambilla, J. Tarrús Castellà, and A. Vairo, "Quarkonium Hybrids with Nonrelativistic Effective Field Theories," *Phys. Rev. D*, vol. 92, no. 11, p. 114019, 2015.

[94] B. Barsbay, K. Azizi, and H. Sundu, "Heavy-light hybrid mesons with different spin-parities," *Eur. Phys. J. C*, vol. 82, no. 12, p. 1086, 2022, [Erratum: Eur.Phys.J.C 82, 1138 (2022)].

[95] S. M. Ryan and D. J. Wilson, "Excited and exotic bottomonium spectroscopy from lattice QCD," *JHEP*, vol. 02, p. 214, 2021.

[96] F. E. Close and E. S. Swanson, "Dynamics and decay of heavy-light hadrons," *Phys. Rev. D*, vol. 72, p. 094004, 2005.

A1   Isospin-1/2 $D\pi$ Scattering

A1.1   Operator Lists

$A_1^+[000]$	$A_1[100]$	$A_1[110]$	$A_1[111]$	$A_1[200]$
$D_{[000]}\,\pi_{[000]}$	$D_{[000]}\,\pi_{[100]}$	$D_{[000]}\,\pi_{[110]}$	$D_{[000]}\,\pi_{[111]}$	$D_{[100]}\,\pi_{[100]}$
$D_{[100]}\,\pi_{[100]}$	$D_{[100]}\,\pi_{[000]}$	$D_{[100]}\,\pi_{[100]}$	$D_{[100]}\,\pi_{[110]}$	$D_{[110]}\,\pi_{[110]}$
$D_{[110]}\,\pi_{[110]}$	$D_{[100]}\,\pi_{[110]}$	$D_{[110]}\,\pi_{[000]}$	$D_{[110]}\,\pi_{[100]}$	$D_{[200]}\,\pi_{[000]}$
$D_{[111]}\,\pi_{[111]}$	$D_{[100]}\,\pi_{[200]}$	$D_{[110]}\,\pi_{[110]}$	$D_{[111]}\,\pi_{[000]}$	$D_{[210]}\,\pi_{[100]}$
$D_{[000]}\,\eta_{[000]}$	$D_{[110]}\,\pi_{[100]}$	$D_{[111]}\,\pi_{[100]}$	$D_{[211]}\,\pi_{[100]}$	$D_{[200]}\,\eta_{[000]}$
$D_{[100]}\,\eta_{[100]}$	$D_{[110]}\,\pi_{[111]}$	$D_{[210]}\,\pi_{[100]}$	$D^*_{[110]}\,\pi_{[100]}$	
$D_{s[000]}\,\bar{K}_{[000]}$	$D_{[111]}\,\pi_{[110]}$	$D^*_{[100]}\,\pi_{[100]}$	$D_{[111]}\,\eta_{[000]}$	
	$D_{[200]}\,\pi_{[100]}$	$D^*_{[111]}\,\pi_{[100]}$	$D_{s[111]}\,\bar{K}_{[000]}$	
	$D_{[210]}\,\pi_{[110]}$	$D_{[110]}\,\eta_{[000]}$		
	$D_{[000]}\,\eta_{[100]}$	$D_{s[110]}\,\bar{K}_{[000]}$		
	$D_{[100]}\,\eta_{[000]}$			
	$D_{s[000]}\,\bar{K}_{[100]}$			
	$D_{s[100]}\,\bar{K}_{[000]}$			
$8 \times \bar{\psi}\boldsymbol{\Gamma}\psi$	$18 \times \bar{\psi}\boldsymbol{\Gamma}\psi$	$18 \times \bar{\psi}\boldsymbol{\Gamma}\psi$	$9 \times \bar{\psi}\boldsymbol{\Gamma}\psi$	$16 \times \bar{\psi}\boldsymbol{\Gamma}\psi$

Table A1.1: Operators used in the S-wave $D\pi$ fits. Subscripts indicate momentum types. $\boldsymbol{\Gamma}$ represents a monomial of γ matrices and derivatives. For more details, see Chapter 4.

$T_1^-[000]$	$E_2[100]$	$B_1[110]$	$B_2[110]$
$D_{[100]}\,\pi_{[100]}$	$D_{[100]}\,\pi_{[110]}$	$D_{[100]}\,\pi_{[100]}$	$D_{[100]}\,\pi_{[111]}$
$D_{[110]}\,\pi_{[110]}$	$D_{[110]}\,\pi_{[100]}$	$D_{[110]}\,\pi_{[110]}$	$D_{[110]}\,\pi_{[110]}$
$D^*_{[100]}\,\pi_{[100]}$	$D^*_{[000]}\,\pi_{[100]}$	$D_{[210]}\,\pi_{[100]}$	$D_{[111]}\,\pi_{[100]}$
	$D^*_{[100]}\,\pi_{[000]}$	$D^*_{[100]}\,\pi_{[100]}$	$D^*_{[000]}\,\pi_{[110]}$
		$D^*_{[110]}\,\pi_{[000]}$	$D^*_{[100]}\,\pi_{[100]}\,\{2\}$
			$D^*_{[110]}\,\pi_{[000]}$
			$D^*_{[111]}\,\pi_{[100]}$
$6 \times \bar{\psi}\boldsymbol{\Gamma}\psi$	$18 \times \bar{\psi}\boldsymbol{\Gamma}\psi$	$18 \times \bar{\psi}\boldsymbol{\Gamma}\psi$	$20 \times \bar{\psi}\boldsymbol{\Gamma}\psi$

Table A1.2: As for table A1.1, but for operators used in the P-wave $D\pi$ fits. The number in curly brackets indicates the number of operators of this kind that were used. For more details, see Chapter 4.

A1.2 Parameterisation Variations

	$\ell = 0$ Parametrisation	$\ell = 1$ Parametrisation	N_{pars}	χ^2/N_{dof}
K-matrix with a Chew-Mandelstam $I(s)$ in both partial waves				
(ax)	$K = \frac{g^2}{m^2-s}$	$K = \gamma_1$	3	1.07
(bx)	$K = \frac{g^2}{m^2-s} + \gamma^{(0)}$	$K = \gamma_1$	4	1.13
(cx)	$K = \frac{g^2}{m^2-s} + \gamma^{(1)}s$	$K = \gamma_1$	4	1.13
(dx)	$K = \frac{(g+g^{(1)}s)^2}{m^2-s}$	$K = \gamma_1$	4	1.13
(ex)	$K^{-1} = c^{(0)} + c^{(1)}s$	$K = \gamma_1$	3	1.07
(fx)	$K^{-1} = \frac{c^{(0)}+c^{(1)}s}{c^{(2)}s}$	$K = \gamma_1$	4	1.13
K-matrix with $I(s) = -i\rho(s)$ in both partial waves				
(gx)	$K = \frac{g^2}{m^2-s}$	$K = \gamma_1$	3	1.08
(hx)	$K = \frac{g^2}{m^2-s} + \gamma^{(0)}$	$K = \gamma_1$	4	1.13
(ix)	$K = \frac{g^2}{m^2-s} + \gamma^{(1)}s$	$K = \gamma_1$	4	1.16
(jx)	$K = \frac{(g+g^{(0)}s)^2}{m^2-s}$	$K = \gamma_1$	4	$1.37^{\dagger}$
(kx)	$K^{-1} = c^0 + c^1 s$	$K = \gamma_1$	3	1.08
(lx)	$K^{-1} = \frac{c^{(0)}+c^{(1)}s}{c^{(2)}s}$	$K = \gamma_1$	4	1.13
Effective range				
(mx)	$k \cot \delta_0 = 1/a_0 + \frac{1}{2}r_0^2 k^2$	$K = \gamma_1$	3	1.10
(nx)	$k \cot \delta_0 = 1/a_0 + \frac{1}{2}r_0^2 k^2 + P_{2,0}k^4$	$K = \gamma_1$	4	$1.11^{\dagger}$
Breit-Wigner				
(ox)	$t = \frac{1}{\rho_0}\frac{m_0\Gamma_0}{m_0^2-s-im_0\Gamma_0}$	$K = \gamma_1$	3	1.08
Unitarised χ_{PT}				
(px)	$t^{-1} = \left(-\frac{1}{16\pi}\mathcal{V}_{J=0}\right)^{-1} + 16\pi\, G_{\text{DR}}$	$K = \gamma_1$	3	1.09

$\dagger$ - physical sheet poles

Table A1.3: The parametrisations used that excluded any levels below threshold. N_{pars} indicates the number of free parameters in each parameterisation. An italicised χ^2/N_{dof} value indicates this fit was not included in the amplitude figure and pole values. For analysis of the results of these parameterisations, see Chapter 4.

$\ell = 0$ Parametrisation	$\ell = 1$ Parametrisation	N_{pars}	χ^2/N_{dof}
K-matrix with Chew-Mandelstam $I(s)$ in both partial waves			
(a) $K = \frac{g^2}{m^2-s}$	$K = \frac{g_1^2}{m_1^2-s}$	4	0.85
(b) $K = \frac{g^2}{m^2-s} + \gamma^{(1)}s$	$K = \frac{g_1^2}{m_1^2-s}$	5	0.84
(c) $K = \frac{(g+g^{(1)}s)^2}{m^2-s}$	$K = \frac{g_1^2}{m_1^2-s}$	5	0.84
(d) $K^{-1} = c^{(0)} + c^{(1)}s$	$K = \frac{g_1^2}{m_1^2-s}$	4	0.85
(e) $K^{-1} = \frac{c^{(0)}+c^{(1)}s}{c^{(2)}s}$	$K = \frac{g_1^2}{m_1^2-s}$	5	0.84
(f) $K = \frac{g^2}{m^2-s} + \gamma^{(0)} + \gamma^{(1)}s$	$K = \frac{g_1^2}{m_1^2-s}$	6	*0.88**
K-matrix with $I(s) = -i\rho(s)$ in both partial waves			
(g) $K = \frac{g^2}{m^2-s} + \gamma^{(0)}$	$K = \frac{g_1^2}{m_1^2-s}$	5	1.12
(h) $K = \frac{g^2}{m^2-s}$	$K = \frac{g_1^2}{m_1^2-s}$	4	0.86
(i) $K = \frac{(g+g^{(1)}s)^2}{m^2-s}$	$K = \frac{g_1^2}{m_1^2-s}$	5	0.84
(j) $K^{-1} = c^{(0)} + c^{(1)}s$	$K = \frac{g_1^2}{m_1^2-s}$	4	0.86
(k) $K^{-1} = \frac{c^{(0)}+c^{(1)}s}{c^{(2)}s}$	$K = \frac{g_1^2}{m_1^2-s}$	5	0.85
K-matrix with Chew-Mandelstam $I(s)$ in S-wave, Effective range in P-wave			
(l) $K = \frac{g^2}{m^2-s} + \gamma^{(0)}$	$k\cot\delta_1 = 1/a_1 + \frac{1}{2}r_1^2 k^2$	5	0.87
Effective range in S wave, K-matrix with Chew-Mandelstam $I(s)$ in P-wave			
(m) $k\cot\delta_0 = 1/a_0 + \frac{1}{2}r_0^2 k^2$	$K = \frac{g_1^2}{m_1^2-s}$	4	0.88
(n) $k\cot\delta_0 = 1/a_0 + \frac{1}{2}r_0^2 k^2 + P_{2,0}k^4$	$K = \frac{g_1^2}{m_1^2-s}$	5	*0.82*†
Effective range in both partial waves			
(o) $k\cot\delta_0 = 1/a_0 + \frac{1}{2}r_0^2 k^2$	$k\cot\delta_1 = 1/a_1 + \frac{1}{2}r_1^2 k^2$	4	0.87
(p) $k\cot\delta_0 = 1/a_0 + \frac{1}{2}r_0^2 k^2 + P_{2,0}k^4$	$k\cot\delta_1 = 1/a_1 + \frac{1}{2}r_1^2 k^2$	5	*0.85*†
Breit-Wigner in S-wave, K-matrix with $I(s) = L(s)$ in P-wave			
(q) $t = \frac{1}{\rho_0}\frac{m_0\Gamma_0}{m_0^2-s-im_0\Gamma_0}$	$K = \frac{g_1^2}{m_1^2-s}$	4	0.86
First-order unitarised χPT			
(s) $t^{-1} = \left(-\frac{1}{16\pi}\mathcal{V}_{J=0}\right)^{-1} + 16\pi G_{\text{DR}}$	$K = \frac{g_1^2}{m_1^2-s}$	4	0.81

† - physical sheet poles

∗ - additional resonance poles

Table A1.4: The parameterisations used that included the P-wave bound state in the data. N_{pars} indicates the number of free parameters in each parameterisation. Here $L(s)$ refers to the Chew-Mandelstam prescription. An italicised χ^2/N_{dof} value indicates this fit was not included in the amplitude figure and pole values. For analysis of the results of these parameterisations, see Chapter 4.

A2 Isospin-3/2 $B\pi$ Scattering

A2.1 Operator Lists

A_1^+ ($L/a_s = 16$)	A_1^+ ($L/a_s = 20$)	A_1^+ ($L/a_s = 24$)
$B_{[000]}\ \pi_{[000]}$	$B_{[000]}\ \pi_{[000]}$	$B_{[000]}\ \pi_{[000]}$
$B_{[100]}\ \pi_{[-100]}$	$B_{[100]}\ \pi_{[-100]}$	$B_{[100]}\ \pi_{[-100]}$
$B^*_{[000]}\ \rho_{[000]}$	$B^*_{[000]}\ \rho_{[000]}$	$B^*_{[000]}\ \rho_{[000]}$
	$B_{[110]}\ \pi_{[-1-10]}$	$B_{[110]}\ \pi_{[-1-10]}$
		$B_{[111]}\ \pi_{[-1-1-1]}$
		$B^*_{[100]}\ \rho_{[-100]}$

Table A2.1: Operators used in the isospin-3/2 S-wave $B\pi$ fits. Subscripts indicate momentum types. The respective lattice spatial length is noted in brackets. For details of the calculation these operators were used in, see Chapter 6.

T_1^- ($L/a_s = 16$)	E^+ ($L/a_s = 16$)	T_1^- ($L/a_s = 20$)	E^+ ($L/a_s = 20$)
$B_{[100]}\ \pi_{[-100]}\ \{2\}$	$B_{[100]}\ \pi_{[-100]}$	$B_{[100]}\ \pi_{[-100]}\ \{2\}$	$B_{[100]}\ \pi_{[-100]}$
		$B_{[110]}\ \pi_{[-1-10]}\ \{3\}$	$B_{[110]}\ \pi_{[-1-10]}\ \{2\}$

Table A2.2: As for table A2.1, but for the T_1^- and E^+ irreps. The number in curly brackets indicates the number of operators of this kind that were used. For details of the calculation these operators were used in, see Chapter 6.